Growth and Low Temperature Transport Measurements of Pure and Doped Bismuth Selenide

by

Jerome T. Mlack

A dissertation submitted to The Johns Hopkins University in conformity with the requirements for the degree of Doctor of Philosophy.

Baltimore, Maryland

July, 2015

Abstract

ABSTRACT

Primary Reader: Nina Marković

Secondary Reader: Mark Robbins

Strong spin orbit materials have become especially interesting due to their potential for applications in spintronics, novel transistors, and the search for Majorana fermions. In order to fully take advantage of these materials they must be thoroughly studied. This work focuses on the material Bi_2Se_3, which is a strong spin orbit material and a topological insulator. I describe a synthesis technique and low-temperature transport measurements of nanostructures of Bi_2Se_3, that when annealed with palladium show evidence of superconductivity. The growth method is a catalyst-free atmospheric pressure vapor-solid growth. The growth method yields a variety of nanostructures, and materials analysis shows ordered structures of bismuth selenide in all cases. Low-temperature measurements of as-grown nanostructures indicate tunable carrier density in all samples. By doping the nanostructures with palladium via annealing, the transport properties of the samples can be altered to

ABSTRACT

exhibit superconductivity. Thin films of palladium are deposited on prefabricated Bi_2Se_3 nanodevices and annealed at temperatures in excess of 100 °Celsius. We find that Bi_2Se_3 absorbs Pd under these conditions and that the absorption of Pd results in evidence of superconductivity, as shown by transport measurements measurements below 1K.

Acknowledgements

There are many people who have helped me on the road that has brought me here. Chief among them have been my advisor Nina Marković and Atikur Rahman. I also have my labmates to thank, especially Nik Hartman whose experience, guidance, and ideas have taken the edge off of the difficulties in what we do. There are also many friends and classmates at Hopkins who have helped give me a distraction from the day to day problems and also to help work through physics. Some names from this group in no particular order are Miguel, Wes, Nick, Mike P., Mike V., Keith, Matt M., Chris M., Matt W., Grace, Tristan, Ben, and so many more.

From my tenure in Copenhagen, I have many people to thank for welcoming me to the lab and helping to better understand aspects of Danish culture those being Christian, Thorvald, Shiv and many others at QDev. I also have to thank Charles Marcus, my advisor at QDev, for allowing me to work in his group, as well as Jess and Katrin who made sure that everything was arranged for me to live there.

My family has also been important in supporting me through it all, especially my parents Jerry and Kelly and sister Karalee.

ACKNOWLEDGEMENTS

Lastly I want to thank my girlfriend Tiff who has kept me sane and supported me even when we have lived far apart.

Contents

List of Figures

LIST OF FIGURES

Chapter 1

Introduction

In 2005 and subsequent years a new sub field of physics came to fruition in both theory and experiment, this is the field of topological insulators. The two early theory papers by Charles Kane and Eugene Mele predicted the existence of the quantum spin hall effect in graphene, an effect that is observable as topologically protected edges states. [3, 4] These edges states are ”topologically protected” because they stem from the time reversal symmetry that is present in the system, and they can only be disturbed by breaking that symmetry. Since these predictions, the topologically protected edge states have been observed in experiments. This has subsequently lead to a discovery of topologically protected surfaces [5–7] in a whole class of otherwise insulating materials [8–15]. Aside from considerable fundamental interest, topologically protected states have an exciting potential application in quantum computing, one particularly promising approach involves nanoscale topological insulators in proximity with superconductors [16–26]. One of these topological

materials is the topic of this thesis and that is bismuth selenide, Bi_2Se_3. This thesis presents a novel catalyst-free growth of topological insulator Bi_2Se_3 nanostructures, new method of creating superconductivity in Bi_2Se_3, and fabrication of nanoscale devices towards the goal of topological quantum computing.

Chapter 2 describes the origin of the spin-orbit coupling, a key component of the topologically protected state in Bi_2Se_3. it also describes the phenomenon of weak antilocalization, which is observed in materials with strong spin orbit coupling at low temperatures, and finishes by introducing some basic properties of Bi_2Se_3.

The basic physics of topological insulators and superconductivity is described in Chapter 3. The chapter concludes with a section on combining these two effects to create emergent collective excitations known as Majorana fermions.

Chapter 4 details the novel catalyst-free growth method developed that yields Bi_2Se_3 nanostructures.

Chapter 5 describes the process of fabricating devices using Bi_2Se_3 nanostructures and turning the nanostructures into measurable electron transport devices.

The cryogenic equipment and transport measurements used to study the devices are described in Chapter 6.

Chapter 7 provides basic transport measurement results from nanodevices made with Bi_2Se_3 nanostructures. These measurements show evidence of the protected surface state conduction and show the challenges of working with this material.

Chapter 8 details the several approaches to inducing superconductivity in Bi_2Se_3. The

first approach involves re-annealing copper doped Bi_2Se_3, a known superconductor. The next approach is doping Bi_2Se_3 with palladium, either by voltage pulse annealing or by thermal annealing.

Chapter 9 concludes this thesis and provides opinions on potential future work.

Chapter 2

Introduction to spin-orbit physics

Spin-orbit coupling is the coupling between an electron's spin and its angular momentum. The simplest method which derives this effect classically, which is also described in David Griffith's *Introduction to Quantum Mechanics* [27], is to look at a hydrogen atom like system, i.e. an electron that is in orbit around a proton. Looking at this interaction from the electron's viewpoint, the proton is seen orbiting around the electron. The orbiting proton acts as a current that flows around the electron and creates a magnetic field. The magnetic field created by the proton applies a torque onto the spin of the electron, causing the magnetic moment of the electron to align with the field. This interaction can be described by the following Hamiltonian:

$$H = -\boldsymbol{\mu} \cdot \mathbf{B} \tag{2.1}$$

The magnetic field **B** can be described using the Biot-Savart law and is:

$$B = \frac{\mu_0 I}{2r} \tag{2.2}$$

The current in this case can be considered to be the charge of the proton over the period of its orbit, which is the same as the period of the electron's orbit in the original picture of this problem. The period of the electron's orbit can then be related to its angular momentum via:

$$T = \frac{2\pi r}{v} = \frac{2\pi m r^2}{L} \tag{2.3}$$

This leads to the magnetic field in terms of angular momentum:

$$\mathbf{B} = \frac{e\mu_0}{4\pi m r^3}\mathbf{L} \tag{2.4}$$

This magnetic field couples to the magnetic dipole moment of the electron spin. Deriving the dipole moment from electrodynamics, the moment of a spinning charge is related to to its spin angular momentum by only a proportionality factor. If the spinning electron is considered to be an equally distributed ring of charge spinning around a central axis with some period, then its magnetic dipole moment can be written as:

$$\mu = \frac{-e\pi r^2}{T} \tag{2.5}$$

Giving the ring mass allows the spin angular momentum to be connected to its moment of inertia and angular velocity:

$$S = \frac{2\pi m r^2}{T} = \frac{-2m\mu}{e} \tag{2.6}$$

This last equation allows the Hamiltonian to now be represented in terms of orbital and spin angular momenta as:

$$H = \frac{e^2\mu_0}{8\pi m^2 r^3}\mathbf{S}\cdot\mathbf{L} \tag{2.7}$$

The derivation presented is a classical picture for a quantum system, but it illustrates the basic premise of the coupling of spin and orbital angular momentum. One important note is that this derivation only considers one proton orbiting an electron. If this increases to *N* protons, the magnitude of the effect in terms of the Hamiltonian scales as such. This means that the spin-orbit coupling strength increases.

A more sophisticated description of the spin-orbit interaction is provided by the Rashba effect and the Dresselhaus effect. In a two dimensional plane, the Rashba picture focuses on the addition of an asymmetric potential being applied perpendicular to the surface of the plane. The Dresselhaus picture focuses on the spin-orbit coupling that arises from crystal asymmetry.

2.1 Weak antilocalization

One of the important experimental manifestations of strong spin-orbit coupling is known as weak antilocalization(WAL). WAL arises due to the destructive interference of

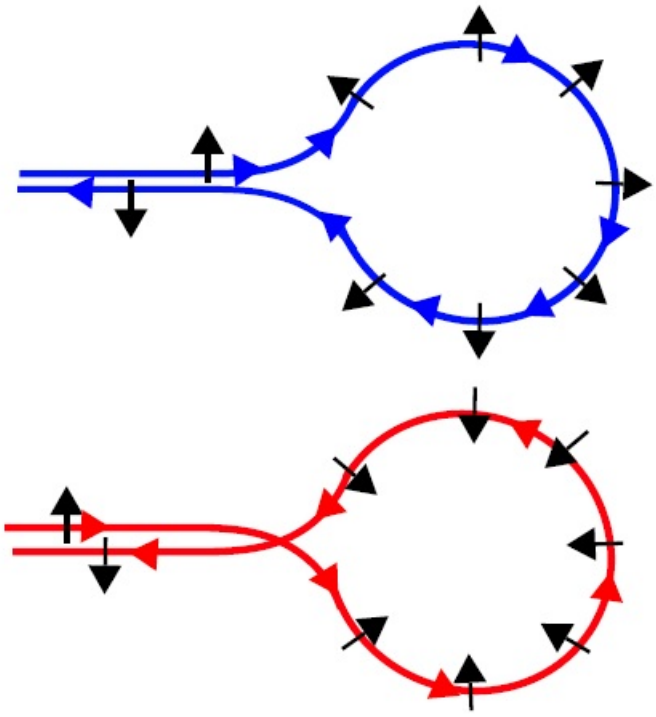

Figure 2.1: Diagram of destructively interfering scattering paths of weak antilocalization. Electron takes the blue path and the spin gains a phase of π after scattering back to its original position. The red path is another possible path, however the spin orbit coupling rotates the spin in the opposite direction adding a phase of -π. The two potential scattering paths add together to give a total phase change of 2π and thus interfering destructively leading to zero backscattering.

electron scattering paths in a strong spin-orbit material. Consider two paths that start at the same point, but where one is the time-reversed version of the other, as depicted in Fig.2.1. On the first path(blue), the spin has rotated due to the coupling with momenta and gained a phase of π. For the time reversed path(red), the rotation of the spin happens in the opposite direction, giving a phase of -π. These two paths interfere destructively, suppressing back scattering and manifesting as a lower average resistivity in the material. Since this effect

relies on time-reversal symmetry it is destroyed by applying a magnetic field to the material. Thus WAL is experimentally observed as a dip in the resistance around zero magnetic field.

2.1.1 Fitting weak antilocalization

In 1980 S. Hikama, A. I. Larkin, and Y. Nagaoka [2] derived an expression for the conductance change due to WAL as a function of magnetic field. The expression yields the coherence length and spin-orbit strength as its fitting parameters. This equation, as presented in Matsuo et. al. [28], is defined as:

$$\Delta G(B) = G(B) - G(0) = \frac{e^2\alpha}{h\pi}[\psi(0.5 + \frac{B_\phi}{B}) - ln\frac{B_\phi}{B}] \tag{2.8}$$

Where the coherence length l_ϕ is expressed in B_ϕ :

$$B_\phi = \frac{h}{8e\pi l_\phi^2} \tag{2.9}$$

α is the parameter which differentiates between strong, weak, and no spin orbit coupling. For α = 0 there is strong magnetic scattering, α = -0.5 gives strong spin-orbit coupling, and α = 1 is the weak spin-orbit case.

2.2 Strong spin-orbit material Bi_2Se_3

As established in the beginning of this chapter, heavier elements have stronger spin-orbit coupling effects. Thus, with the heavy element bismuth, Bi_2Se_3 is a semiconducting material with strong spin-orbit coupling. The semiconducting gap in Bi_2Se_3 is 0.3 eV, which is roughly equivalent to 3,480K. The structure of the material is depicted in Fig.2.2. It is a largely hexagonal structure that forms into five-atom thick quintuple layers of Se-Bi-Se-Bi-Se, squared in purple, where after the third Se the pattern repeats, starting again with Se. The quintuple layering and Se to Se termination means that similar to graphite, Bi_2Se_3 can be peeled apart layer by layer using mechanical exfoliation. However, instead of getting a single-atom layer like graphene, the minimal thickness is a single quintuple layer that is approximately 1 nm thick. The important property that makes Bi_2Se_3 the subject of this thesis is that it was proven to be a topological insulator in 2009 [29]. In the next chapter this property will be defined and described and it will also be shown how this property can be applied, along with superconductivity, to help build a new type of a quantum bit.

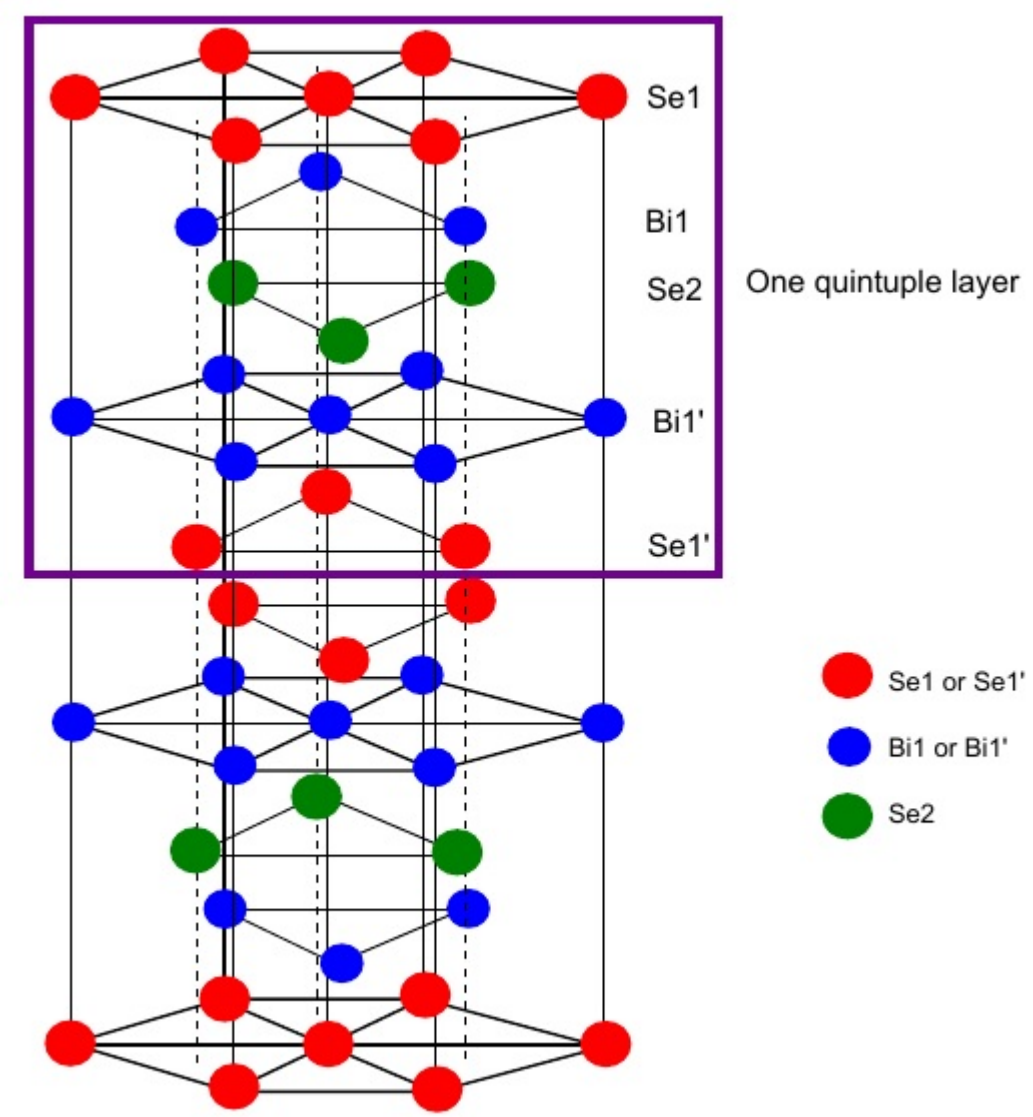

Figure 2.2: Hexagonal quintuple layer crystal structure diagram of Bi_2Se_3. A single quintuple layer, boxed in purple, is five atoms thick and ordered Se-Bi-Se-Bi-Se.

Chapter 3

Topological insulators and superconductivity

3.1 What are topological insulators?

Topological insulators are materials which are insulating in bulk, but when placed next to an ordinary insulator or vacuum, a metallic surface forms at the boundary. This surface forms because the bulk is topologically different from a normal insulator. In order to explain the notion of being ”topologically different”, one can compare a sphere and a donut, as shown in Fig.3.1. The sphere and donut are topologically different, it is impossible to adiabatically change one to the other. In order to transform the sphere into the donut, it must be broken by adding a hole.

What this means in the context of the electronic band structure is described in the review

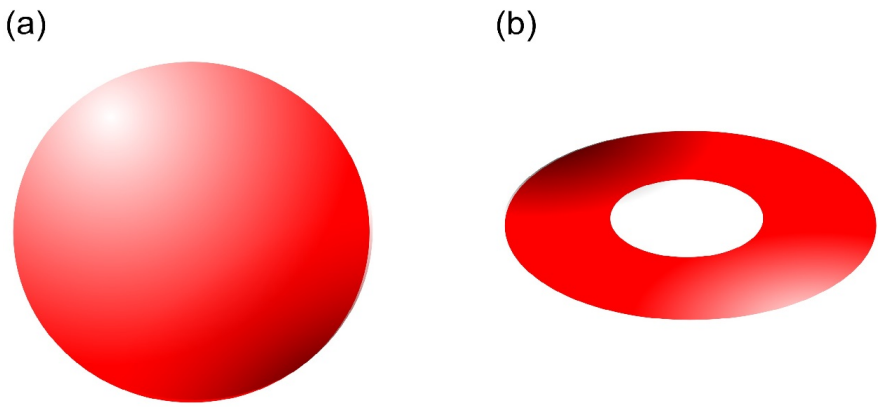

Figure 3.1: Diagram of sphere and donut which have a different topology, representing the difference between a normal insulator and a topological insulator. In order to transform one into the other a drastic change, in this case a hole, must take place during the transformation.

article by Hasan and Kane from 2010 [23]. When looking at the band structure for a material, gapped structures can be defined into topologically different sets based on whether they can be adiabatically deformed into each other without closing the energy gap. If a band structure from one material cannot be deformed into that of another, then they are characterized by a different topological invariant. In transitioning one system into a topologically different one, there must then be some point where the gap crosses back,this crossing is what gives the metallic surface state.

The metallic surface state appears in the surface band structure of a topological insulator in the form of a Dirac cone that crosses the semiconducting gap. The electrons of the surface state act as massless relativistic Dirac fermions that follow a linear dispersion relation that is depicted for a surface state in Fig.3.2(a), with a line cut of the Dirac cone shown in Fig.3.2(b).

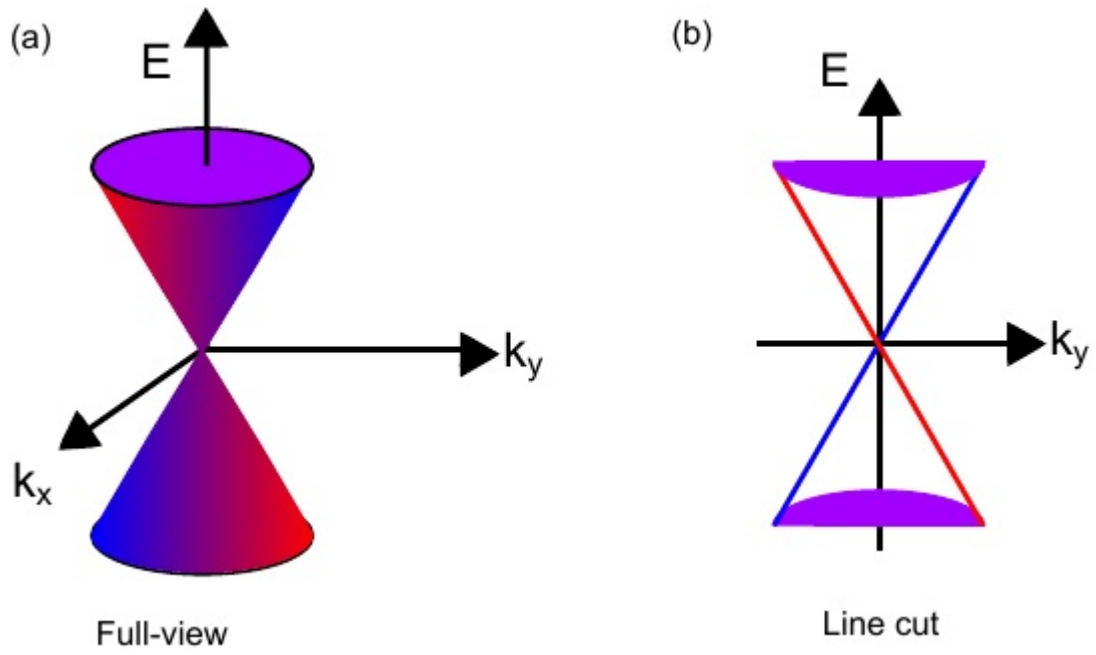

Figure 3.2: Diagram of linear dispersion relation of massless Dirac fermions, also known as a Dirac cone. (a) shows the Dirac cone which forms for a surface state. (b) shows a single line cut of (a), which is also the form of the dispersion for a topological edge state.

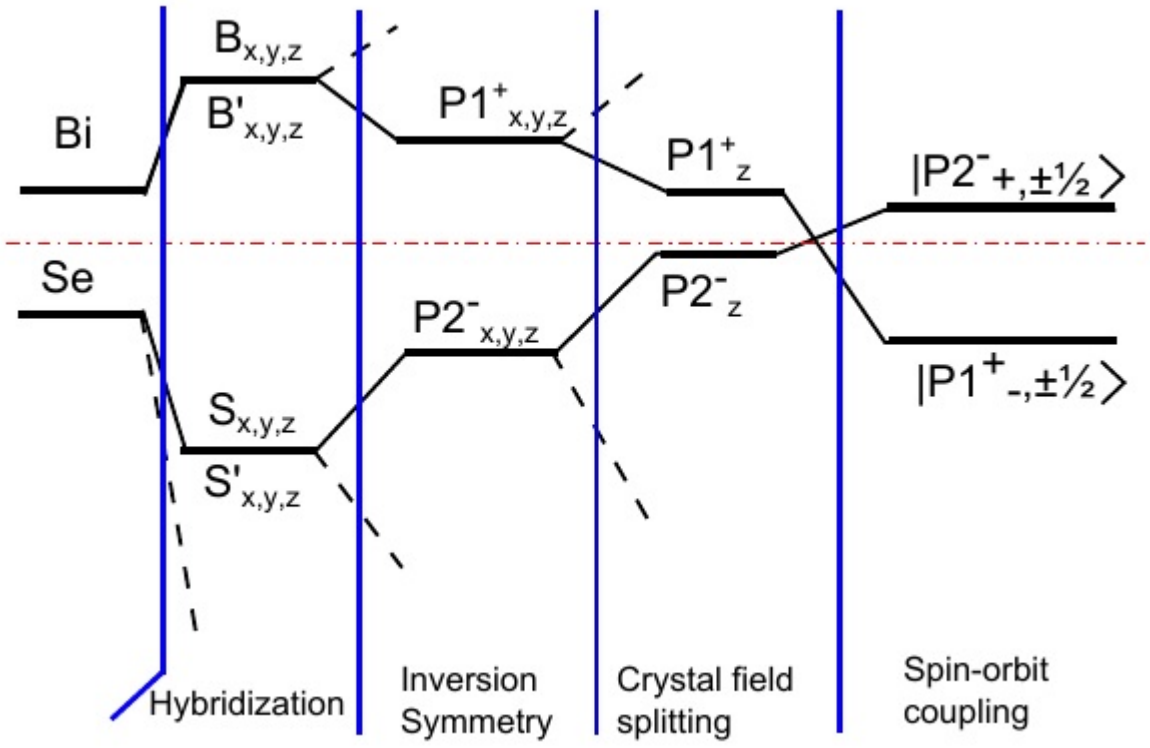

Figure 3.3: Diagram of selected parts of the energy levels of Bi_2Se_3 as various native effects are added in. Adapted from C. X. Liu et. al. [1]

3.1.1 Bismuth selenide as a TI

Bi_2Se_3 is an insulator that does is in fact have a topologically different band structure than a normal insulator. C. X. Liu et. al. [1] calculated the band structure and observed an inversion between two of the bands, giving rise to the topological surface states in the material. Fig.3.3 shows the band inversion in Bi_2Se_3 as a function of adding in various symmetries of this material. The first section of 3.3 starts with considering just the Bi and Se orbitals. The second section takes into account that since the Se layers are separated by

layers of Bi the strongest coupling between orbitals happen between Bi and Se layers. This causes level repulsion and the formation of new hybridized states. The system also has inversion symmetry, leading to the formation of bonding and anti-bonding sites (section three):

$$|P1^{\pm},\alpha\rangle = \frac{1}{\sqrt{2}}\left(|B_\alpha\rangle \mp |B'_\alpha\rangle\right)\ and|P2^{\pm},\alpha\rangle = \frac{1}{\sqrt{2}}\left(|S_\alpha\rangle \mp |S'_\alpha\rangle\right) \tag{3.1}$$

where $\alpha = p_x, p_y, p_z$. Since the crystal structure is layered, the z direction in the atomic plane is different from x and y, giving a splitting of the p_z orbital from the p_x and p_y orbitals(section four). Finally, when accounting for spin, the addition of spin-orbit coupling splits the orbitals once more into spin up and spin down states. It is this final splitting that causes the energy levels to cross, giving the inversion of two bands and leading to the topologically protected metallic surface.

3.2 What is superconductivity?

A superconductor is a material which when cooled below a certain temperature has zero resistance and expels magnetic field. This has been experimentally observed in many different materials since 1911, and theoretically understood since 1957 in a theory by Bardeen, Cooper, and Schrieffer [30, 31], by what is known as BCS theory. There are many different superconductors and some do coexist with magnetic fields, but the type that has been best described are the conventional metal superconductors which are described by BCS theory.

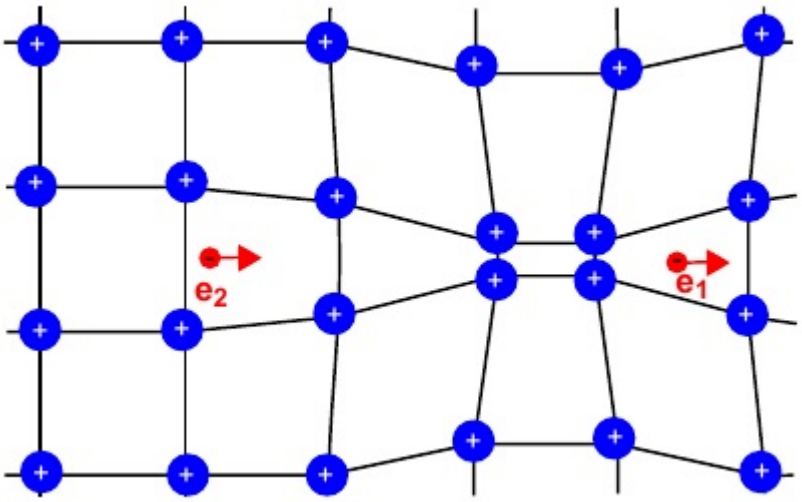

Figure 3.4: Diagram of basic Bardeen-Cooper-Schreiffer pairing process.

The basic picture of BCS theory is depicted in 3.4. When the material is cooled below its transition temperature, T_c, electrons begin to pair. The mechanism for the electrons pairing is that as an electron travels though the material it attracts positive charges in the crystal lattice. The attraction causes the trail behind the electron to have a higher density of positive charge than the normal crystal lattice background. The higher density region then attracts a second electron, thus pairing the two electrons together mediated by the lattice deformation. This pairing means the electrons are now correlated, and there are of course many pairs of electrons, which means their wave functions overlap with each other. The overlapping of the pairs means that all pairs are treated as a collective condensate.

When a superconducting material is placed next to a normal material, the Cooper pairs are able to diffuse into the material, creating some amount of superconductivity in the

normal material where it makes contact with the superconductor. This induced superconductivity is called the proximity effect, and penetration depth into the normal material is dependent on the coherence length, which in BCS theory is the size of the Cooper pairs. This allows one to combine the superconducting pairing with other material effects to create emergent phenomena. One of these phenomena is the Majorana fermion, which is discussed in the next section.

3.3 Topological insulators combined with superconductivity

As mentioned before, it is the combining of topological insulators with superconductivity that is a primary driving force in the field. The reason is that this combination has been predicted to allow for the emergence Majorana fermions which, under the right conditions, are considered to allow for a new and more robust form of quantum computing. Majorana fermions were first predicted, by Ettore Majorana, to exist as physical particle which was its own anti-particle [32].

In condensed matter systems, one of the most straight forward models for creating these quasi-particles is that proposed by Alexei Kitaev in 2001 [33]. The setup is that a 1-D quantum wire is placed on a 3-D superconductor. The wire has a number of sites L much greater than one, and each site can only be occupied by a spinless electron or completely unoccupied. The Majorana is a quasiparticle excitation which is a superposition of an

electron and hole, thus two Majoranas make up an electron. The electron creation and annihilation operators are then formed into Majorana creation and annihilation operators and are:

$$c_{2j-1} = a_j + a_j^\dagger, \quad c_{2j} = \frac{a_j - a_j^\dagger}{i} \quad (j = 1, ..., N) \tag{3.2}$$

which satisfy:

$$c_m = c_m^\dagger, \quad c_m c_l + c_l c_m = 2\delta_{lm} \quad (l, m = 1, ..., N) \tag{3.3}$$

with a_j and $a_j^\dagger$ being the electron creation operator and the electron(hole) annihilation(creation) operator. In the model, Majoranas are shown to appear at the ends of the wire when the superconducting gap is greater than zero. This possibility can be partially explained by converting the spinless electron site picture to a string of Majorana fermions, depicted in going from Fig. 3.5(a) to Fig. 3.5(b). One can keep each Majorana paired with its original partner on its site, as in Fig. 3.5(b) or one can pair them to neighboring sites, as depicted in Fig. 3.5(c). If the chemical potential, gap of the superconductor, and amplitude of hopping from one site to another are correctly tuned, the Hamiltonian Kitaev created for this system reduces to a form that leaves an unpaired Majorana at each end of the wire, Fig. 3.5(c).

This basic formulation is potentially a powerful tool for quantum computing according to the theory. A single qubit would be comprised of the two Majoranas, which are correlated together, with the two qubit states being the presence or absence of the quasiparticle. If the Majoranas are sufficiently separated then this information has been made non-local and can only be accessed when both are measured. This non-locality would mean that

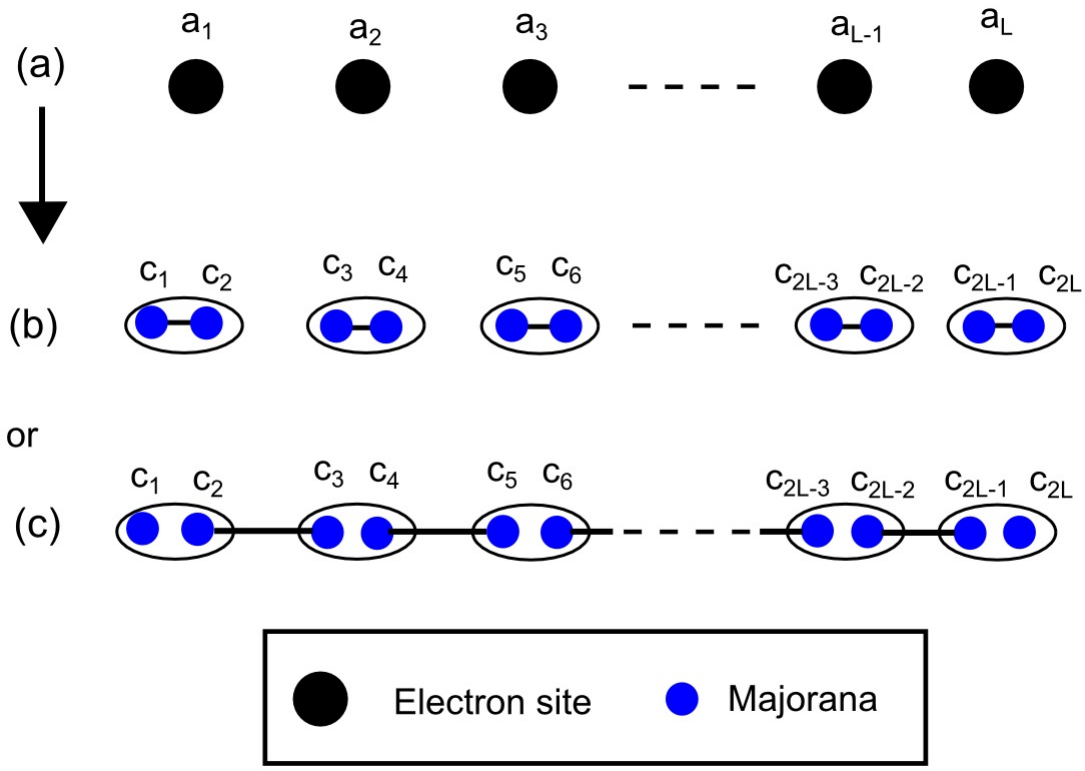

Figure 3.5: Diagram of one-dimensional wire Kitaev model. (a) All sites have possibility for electron or hole. (b) All sites are divided up into two Majoranas at each site where the Majoranas are paired together at each site. (c) Alternate pairing scheme where Majoranas pair with neighbor site Majorana, leaving an unpaired Majorana at each end of the wire.

fluctuations local to one Majorana would not disturb the state of the overall qubit, leading to longer coherence times. Further operations of a Majorana based quantum computer are more complex and a good resource is the review article by C. W. J. Beenaker [22].

The toy model has been advanced by Cook and Franz in 2011. Their proposal involved putting a topological insulator nanowire on top of a superconductor, this method also produced Majorana fermions at the ends of the nanowire. There are also device based proposals by Fu and Kane [16] and Ilan et. al. [25] Both of these proposals involve creating a Josephson junction out of two superconductors and a topological insulator that is either a sheet, as in the Fu and Kane paper [16], or a nanowire, as in the Ilan et. al. paper [25]. In the case of the second article, the existence of the Majorana fermions is observed as a peak in the critical current when a magnetic field equivalent to half a flux quantum is applied parallel to the nanowire.

Experimentally several groups have combined topological insulators and superconductors in order observe the Majoranas. Some of the groups have claimed to have created them, but there is still debate [22].

Chapter 4

Nanostructure Growth

There are many ways to grow Bi_2Se_3 such as molecular beam [34, 35] and hot wall [36] epitaxy, single crystal growth [9, 14, 37], sonoelectrochemical methods [38, 39], mechanical exfoliation [40, 41], and chemical vapor deposition(CVD) methods [42–44]. The CVD methods though, are one of the easiest for growing nanomaterials. The ratio of surface to bulk is maximized in a nanomaterial, helping to increase the relative contributions of the surface to transport measurements. An as-grown nanostructure also has the advantage of being a single crystal, reducing the potential for defects. Chemical vapor deposition, specifically the gold catalyst vapor-liquid-solid(VLS) technique [42], was one of the first, at the time most straightforward, and most widely used method for growing Bi_2Se_3 nanostructures.

The method developed in this thesis is a derivative of the original VLS method with three main differences in the overall process: the use of hydrogen carrier gas, no gold

catalyst is used, and the quartz tube is allowed to remain at atmospheric pressure [45]. The other main difference between the method presented here and previous methods, is that this method has been shown to work on multiple substrates. By growing on flexible mica, cheap and transparent glass slides, and semiconductor industry device standard silicon-oxide covered silicon, the catalyst-free method allows for making as grown nanostructure devices for a variety of applications. The following sections of this chapter will layout the catalyst-free method, show the resultant nanostructures, and prove that the nanostructures are indeed Bi_2Se_3 by utilizing a variety of materials analysis methods.

4.1 Catalyst-free growth method

The catalyst-free method begins with preparing the substrates. Three different substrates were used in developing this method: glass slides, mica, and 300nm silicon-oxide capped silicon(hereafter referred to as simply silicon). The substrates, with the exception of the mica, are cleaned before use. The cleaning process is performed in a cleanroom and starts with 5 minutes of sonication in acetone, continues with 5 minutes of sonication in isopropanol, and five minutes on a hotplate set to 185 °C. The substrate cleaning step removes contaminants from the substrates which could alter the growth. The mica does not go through this process because of its fragility and instead the substrates are freshly cleaved using mechanical exfoliation immediately before growth, thus exposing a clean surface.

The furnace setup for the catalyst free method is depicted in Fig.4.1. Bulk Bi_2Se_3

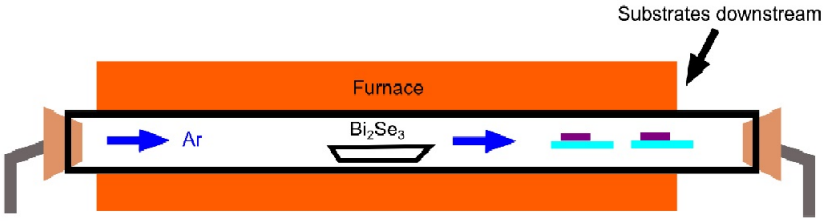

Figure 4.1: Diagram of the growth setup and results. (a) Quartz tube furnace setup. A ceramic boat containing Bi_2Se_3 is located in the center of the tube. On the right end of the tube are glass slides of size 2.3x2.54 cm. The slides are located in a range from 13.5-19 cm from the center of the furnace. Prior to growth, argon is flowed at a rate of 1500 sccm for 15 minutes to purge the system of any oxygen. After purging the flow rate is decreased to 200 sccm, H2 gas flow of 5 sccm is started, and the furnace is set to 700C. When the furnace reaches the set temperature, the H2 gas is turned off and the furnace is allowed to cool down.

source crystals, obtained from Alfa Aesar, are placed in a ceramic boat in the center of a quartz tube in a tube furnace. Growth substrates are placed near the end of the tube furnace in such a way that they will be downstream from the ceramic boat in regards to the flow direction of the carrier gases. With the substrates and source materials in place the tube quartz tube is flushed with high purity argon gas at a flow rate of 1600 sccm for fifteen minutes. The argon gas flush is to insure that potential contaminants in air are removed from the tube. After the flush is complete, it is time to start the growth process.

The growth process starts with lowering the argon flow rate to 200 sccm and adding H_2 at a flow rate of 5 sccm. With the Ar and H_2 rates stable, the furnace is set to 700 °C. When the furnace reaches the set temperature, it is kept at this temperature for only five minutes. During this time period, Bi and Se vapors from the melting bulk source crystals are being carried downstream by the Ar and H_2 gases. As these vapors travel downstream,

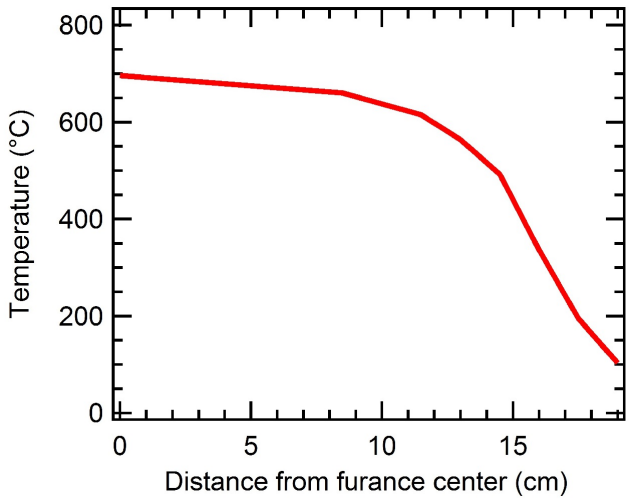

Figure 4.2: Temperature profile of quartz tube furnace used for growth, temperature represented as a function of the distance from the center of the furnace.

they reach increasingly colder regions of the furnace and begin to condense. The measured temperature at increasing distances from the center of the furnace when the set point is 700 °C is shown in Fig.4.2. In the graph, 0 cm is the exact center of the tube furnace and 19 cm and beyond is outside the furnace, but still in the quartz tube. Different temperature regions yield different types of nanostructures. After reducing the set temperature and turning off the furnace, the Ar gas is left on while the H_2 gas is turned off. The furnace is allowed to cool naturally down to room temperature at which point the Ar gas flow is stopped and the samples may be removed from the furnace. It should be noted that it is possible to achieve nanostructure growth with slightly lower temperature and flow rates. The most important conditions for successful growth were a temperature above 600 °C and the inclusion of H_2 as a carrier gas.

4.2 Catalyst-free results

After the growth has been completed, the first step in analyzing the results is to look at the substrates under an optical microscope to determine whether nanostructures have grown, where they have grown, and whether they have the hexagonal crystal structure that should be exhibited by Bi_2Se_3. Obtaining the desired results is the product of many trials, hours, and tweaks to the growth recipe. The following sub-sections will show the growth results for all three types of substrates.

4.2.1 Glass Slide Growth

As one moves from the center of the furnace to its edge, the temperature gradually decreases, as shown in Fig.4.2. In order to properly locate the optimal temperature region for successful growth of nanostructures, glass slides were lined up in the quartz tube at positions from 11.5 cm to 19.6 cm from the furnace center. Distances below 11 cm were not tested as the glass slides would begin to melt and warp in these hotter regions. Fig.4.3 depicts the results of one of these growths where the set temperature was 600 °C with Ar gas flow of 120 sccm and H_2 gas flow of 3 sccm. In Fig.4.3(a) at a distance of 11.5 cm there are no large structures, showing the first region was not conducive to growth. In the colder 14 cm region, depicted in Fig.4.3(b), some nanostructures can be seen, including wires, ribbons and flakes. Going further from the center of the furnace to 16.5 cm, Fig.4.3(c), nanowires and ribbons are observed growing up from the surface of the substrate in large

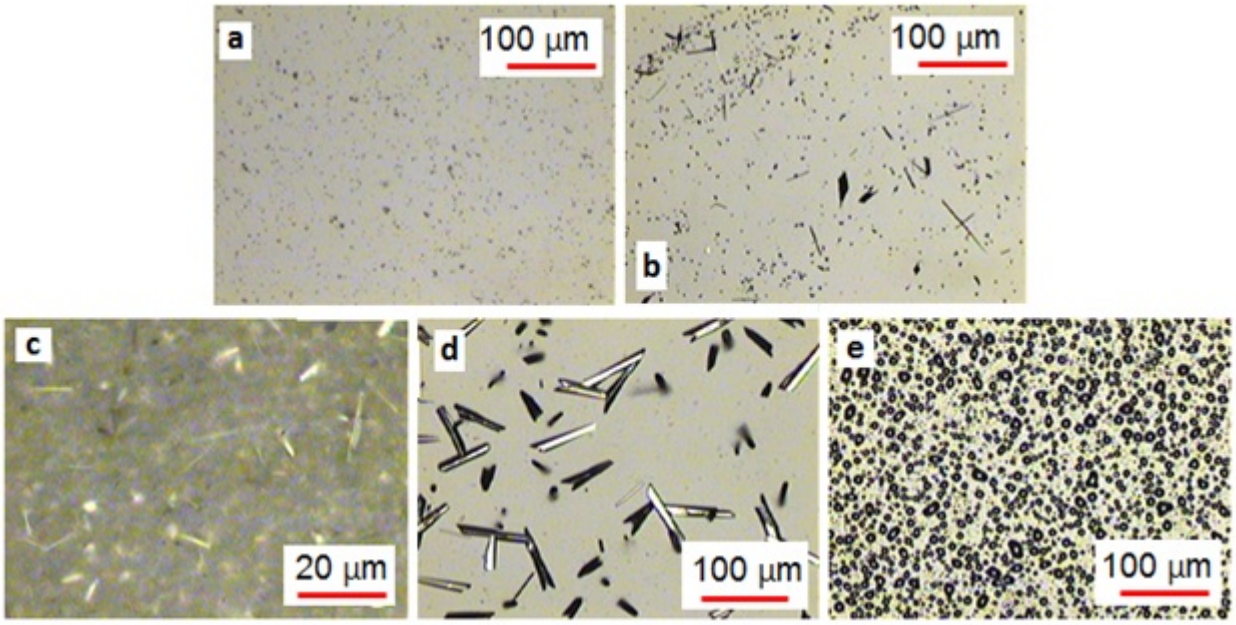

Figure 4.3: Optical microscope images of Bi_2Se_3 growth results on glass slides using standard recipe as a function distance from the center. (a) Growth in the region around 11.5 cm from the center, no nanostructures are found on small particulate. (b) Growth in the region around 14 cm from the center, nanowires and ribbons are grown in this region. (c) Growth in the region around 16.5 cm from the center, nanowires and ribbons are grown in this region. (d-e) Growth in the region around 19.5 cm from the center, this region at the edge of the end of the furnace with (d) closer to the center than (e). This region is the coldest growth region and any structures in this region are not Bi_2Se_3 but pure selenium.

quantities. Finally in the coldest region at the edge of the furance at 19.6 cm, Fig.4.3(d) and (e), only small flakes were observed. The nanostructures in this cold region, although the correct size for device making, are not in fact Bi_2Se_3. This was determined by fact that these nanostructures melt at 200 °C, which is lower than the melting temperature of Bi_2Se_3, 710 °C, and thus suspected to be solid selenium(melting point 221 °C).

In order to emphasize the importance of including H_2 as a carrier gas in order to achieve nanostructures, growth results from the 14-16 cm region without H_2 is shown in Fig.4.4.

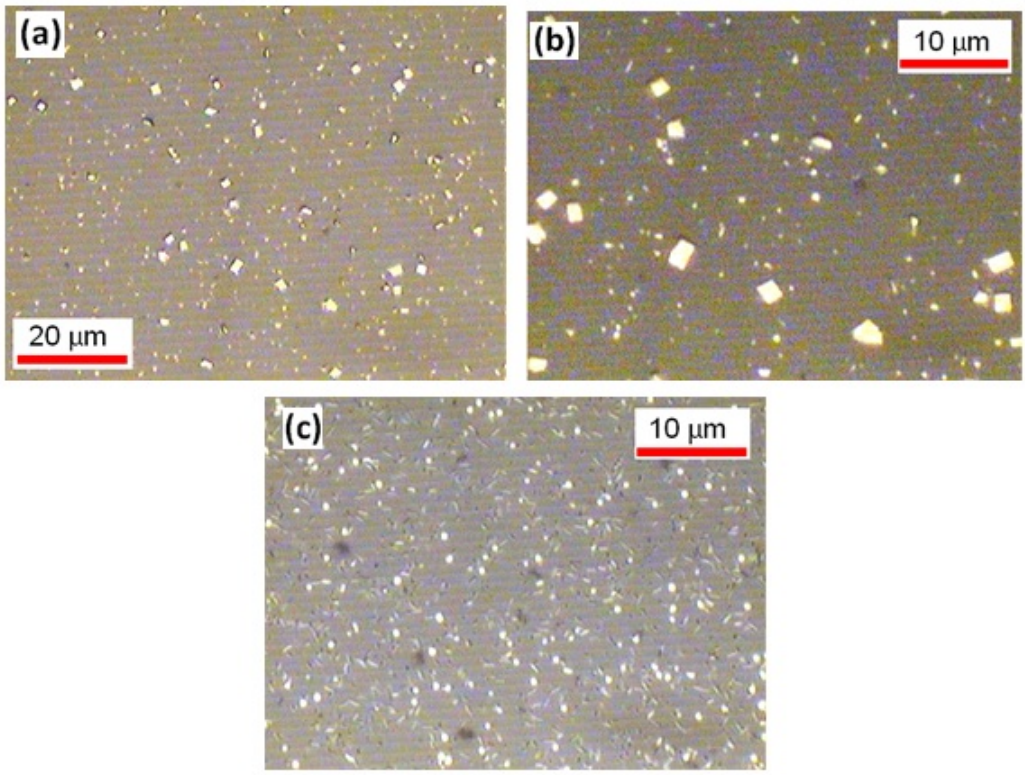

Figure 4.4: Examples of growth on glass slides in 14-16 cm region when hydrogen carrier gas is not present. (a-c) All three images show some amount of particulate and small nanostructures, but the structures are too small for fabrication and are of unknown composition.

The growth was performed using a set temperature of 700 °C and Ar flow of 200 sccm. Although in all three images, Fig.4.4(a-c), there are some micron-sized structures, they are rectangular as opposed to hexagonal and in general too small to be used to fabricate nanodevices from.

4.2.2 Other substrates

With the growth recipe worked out and the optimal growth region located, it is easy to start growing on alternate substrates. All growth results in this subsection were performed in the 14-16 cm region and using the recipe of 700 °C, Ar flow of 200 sccm, and H_2 flow of 5 sccm.

A mica sample is shown in Fig.4.5, with (a-c) being optical images of nanostructures formed on the substrate and (d) being an atomic force microscope profile and image of an area of the sample. The mica growth shows a nanoplatelet layering, silver and light gray areas, across the substrate in contrast to the largely individual structures that grow on glass slides. The nanoplatelet layering is observed to continuously cover large areas of the substrate. As expected for Bi_2Se_3 the layered structure shows largely hexagonal shapes with some quadrilateral shapes that are partial hexagons. In Fig.4.5(c) however, two nanorods are observed laying on the surface of the substrate and a nanoribbon is observed growing of the substrate(black, partially out of focus in bottom center of the image). Using an atomic force microscope(AFM) the thickness of the nanoplatelet layers can be measured and compared to the known thickness of the Bi_2Se_3 crystal structure. 4.5(d) shows a height trace(left) from a sample(right) that was imaged using the AFM, the layer height that was found from this measurement for the lower layer(height comparison region denoted by red triangles). This lower layer was found to be approximately 3nm which is roughly three times the c-axis height for a single Bi_2Se_3 [46] quintuple layer.

Growing nanostructures on silicon is the most important for establishing the catalyst-

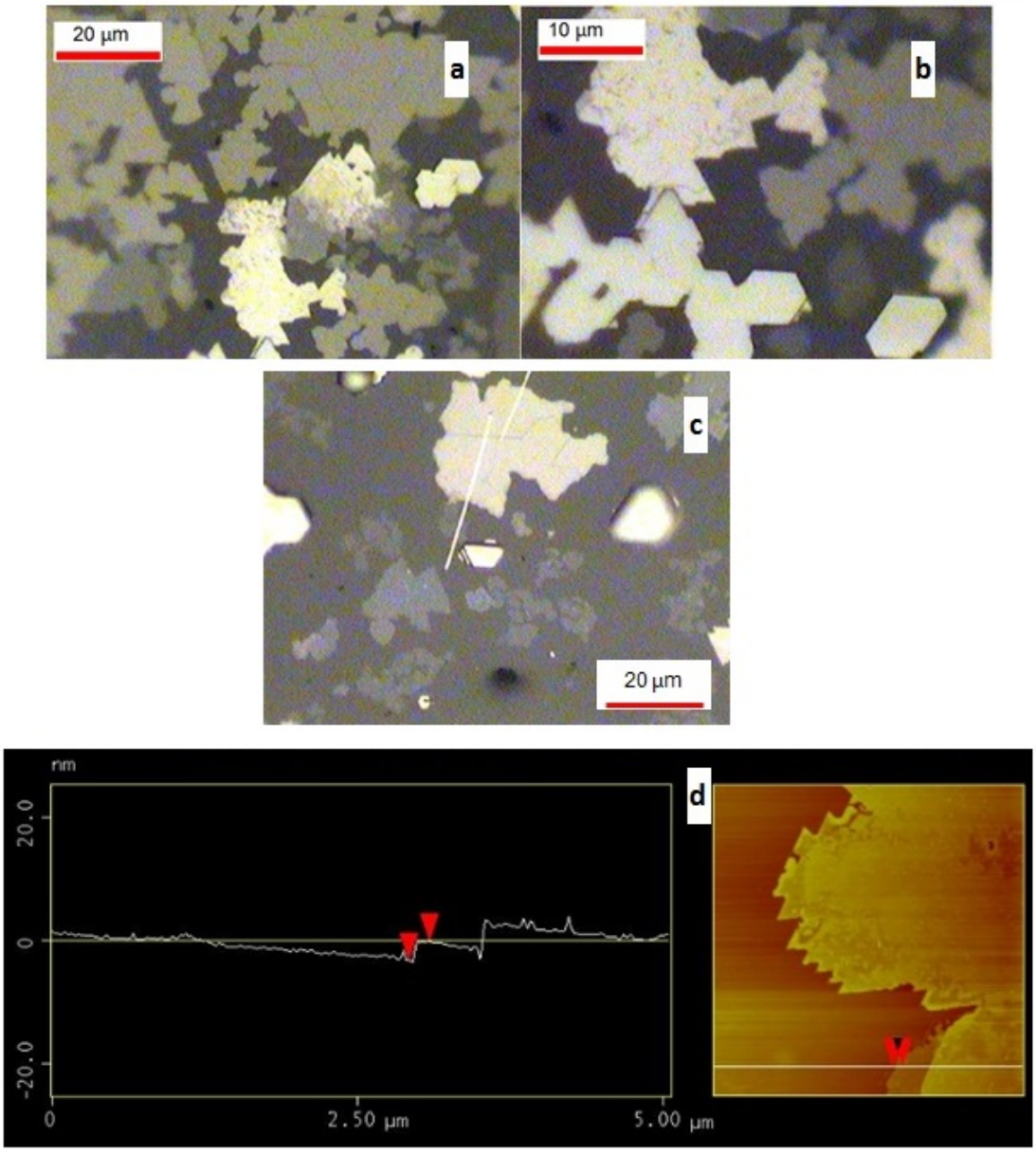

Figure 4.5: Optical images and AFM height analysis of nanostructures grown on mica using catalyst free method in the 14-16 cm temperature region. (a-b) Nanoplatelet layering of Bi_2Se_3 in hexagonal and triangular shapes. (c) Nanostructure layering and nanorods. (d) AFM height analysis and corresponding image, height analysis between points denoted by red markers gives a height difference of approximately 3 nm which is equivalent three times the c-axis height of Bi_2Se_3.

free method as a good standard for device fabrication. Shown in Fig.4.6 are images of silicon substrate growth results. Fig.4.6(a) is an optical image that shows not only some nanostructures grown on the surface(silver), but also thin structures, both ribbons and rods growing of the surface as was observed on glass and mica(black and partially out of focus). Also, as with the glass slides, no large amounts of nanoplatelet layering are observed. Fig.4.6(b-d) are scanning electron microscope(SEM) images that emphasize the diversity of structures found on silicon substrates. In 4.6(b) the image is focused on a nanorod over 15 μm in length is observed as well. Small groupings of well-formed hexagonal and partial hexagon quadrilateral nanoplatelets are also observed. A nanoribbon is the focus of 4.6(c). The ribbon is semi-transparent, which provides evidence that the nanostructures are thin. 4.6(d) also shows semi-transparent nanoribbons of various shapes and size, but all show the hallmarks of internal hexagonal structure with corners having angles of 60° of 120°.

4.3 Material Analysis

The nanostructures grown using the catalyst method can be shown from optical, SEM, and AFM imaging to have the characteristic shape of a hexagonal crystal structure like that of Bi_2Se_3. However, images are not enough to prove that they are Bi_2Se_3. In order to be sure that the nanostructures have the right chemical composition and crystal structure a transmission electron microscope(TEM) is used. A TEM is a microscope which transmits electrons through an ultra-thin sample. As the electrons pass through a sample, they

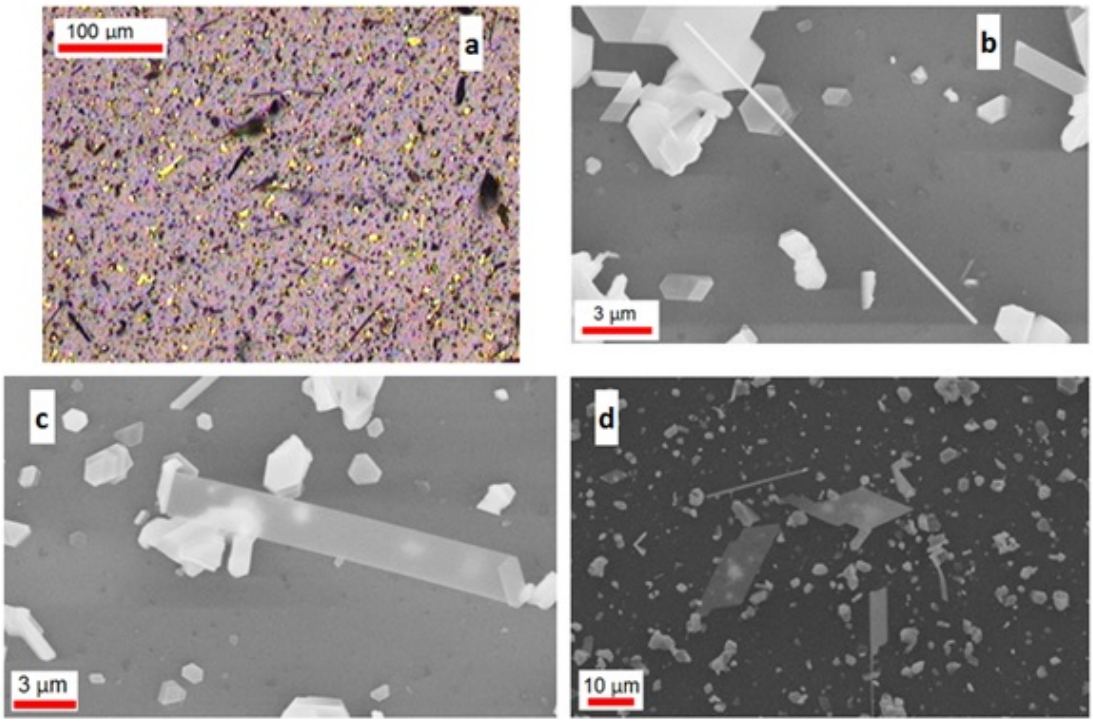

Figure 4.6: Optical microscope image of Bi_2Se_3 nanostructures in 14-15.5 cm region, approx. 20 m long nanowire in upper right hand corner.

interact with the material itself, allowing a user to determine the crystal structure, lattice spacings, and chemical composition, of the material. This section will describe three basic techniques for determining these properties and their results when applied to the catalyst-free nanostructures presented in the previous section. The nanostructures in this section were grown on glass slides and silicon.

4.3.1 High Resolution Transmission Electron Microscopy

High resolution transmission electron microscopy(HRTEM) is a useful tool that allows a user to directly image the crystal structure of a sample and is sometimes referred to as phase contrast TEM. As the electrons from the TEM beam travel through a sample, some are diffracted by the sample and others are transmitted without scattering. Each group or wave of diffracted electrons gains its own phase that depends on the scattering path through the material. When the transmitted and diffracted electrons exit the sample, they create interference patterns that reflect on the internal crystal structure of the material. If a sample is thin enough, the diffraction will only occur on a few lattice sites and the resulting interference image will better reflect the exact crystal structure.

For the catalyst-free Bi_2Se_3 nanostructures, HRTEM can provide information on the crystal lattice spacing in the structures. Fig.4.7 depicts TEM images(Fig.4.7 (a) and (b)) and an HRTEM image(Fig.4.7(c)) of nanowires that were grown on glass slides. In Fig.4.7(a) and (b), two different nanowires are found to have a diameter of around 100 nm and lengths beyond 1 micron. The HRTEM image of Fig.4.7(c) is from a portion of the

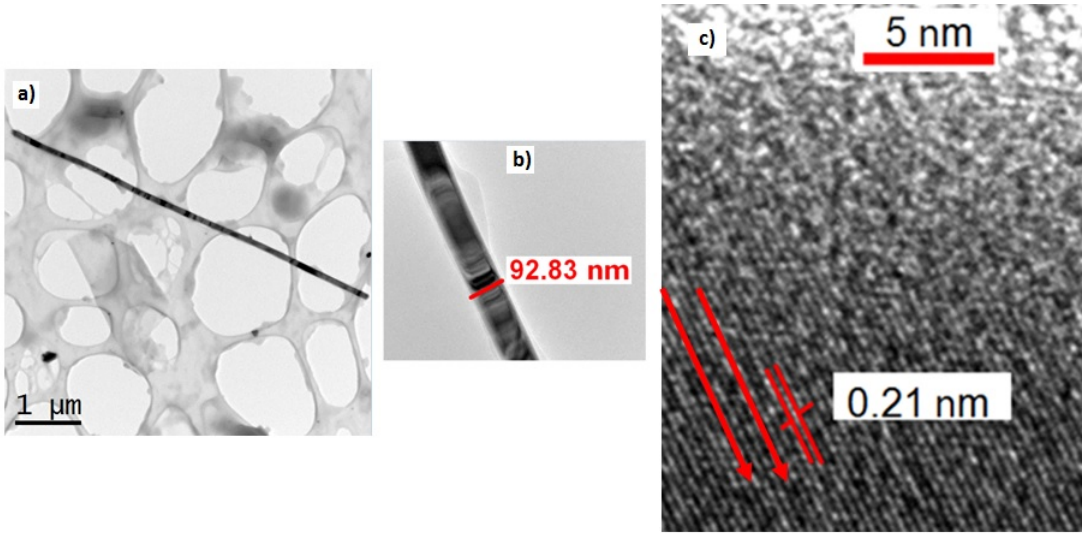

Figure 4.7: TEM and structural analysis of glass slide grown Bi_2Se_3 nanowire. (a) A TEM image of a nanowire that is 6 m long and 100 nm in diameter. (b) A TEM image of a Bi_2Se_3 nanowire, with a diameter of 93 nm.(c) High-Resolution TEM image of the nanowire shown in (a). Lattice spacing is found to be 0.21 nm in accordance with the Bi2Se3 lattice structure.

nanowire shown in Fig.4.7(a). Looking at the HRTEM image, there is clearly a layered structure that is at an angle from the primary axis of the wire, highlighted by the red arrows, showing that for this wire the growth was not a neat vertical stacking but most likely a preferentially offset stacking of layers. It is also possible to estimate the layer separation from the HRTEM image. The layer separation in this case is 0.21 nm, in agreement with known values for Bi_2Se_3 [42].

4.3.2 Selected Area Diffraction

Apart from looking at a larger interference pattern and larger range crystal structure, it is also possible look at diffraction and crystal properties in a smaller area which is known as

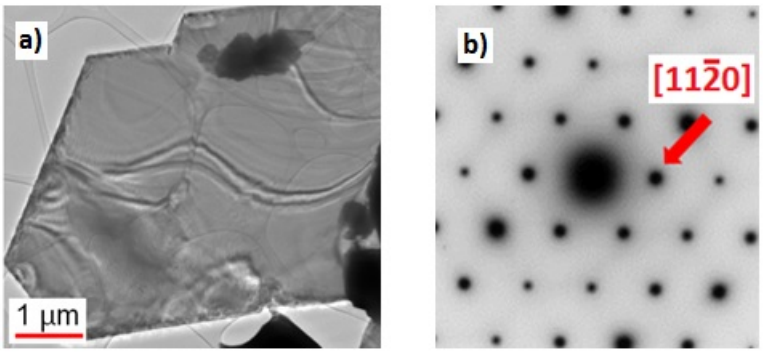

Figure 4.8: TEM image and diffraction pattern of Bi_2Se_3 nanoplatelet grown on silicon wafer substrate. (a) TEM image of a typical nanoplatelet. (b) Selected area diffraction of the nanoplatelet shown in (a). Analysis of SAED shows hexagonal structure with the radial pattern corresponding to the [110] direction.

selected area diffraction(SAED). In SAED, the sample acts as a diffraction grating and as with HRTEM, the electrons in the electron beam are scattered and diffracted by the atoms in the material. In order to make the area selected small, apertures are used to carefully control the size of the electron beam that is probing the sample. The resulting image of the diffracted electron beam is observed as a series of spots in a pattern that is directly related to the location of the atoms in the sample, i.e. the crystal structure. The shape and size of the pattern relative to the sample position can be used to calculate the crystal axis lengths as well as the crystal planes in the material.

The use of SAED to analyze a catalyst-free nanoplatelet is shown in Fig.4.8. Fig.4.8(a) shows a TEM image of a hexagonal nanoplatelet and Fig.4.8(b) shows the resultant SAED pattern from this nanostructure. The hexagonal SAED pattern agrees with the hexagonal super-structure of the sample, the pattern shows the hexagonal crystal axis of the [11-20] plane, and that the top and bottom of the structure are of the [001] plane. The SAED

provides further evidence that the nanostructures have the same crystal structure as Bi_2Se_3.

4.3.3 Energy Dispersive X-ray Spectroscopy

The third way that a TEM was used to help confirm the nanostructures as Bi_2Se_3 was through the the use of energy dispersive X-ray spectroscopy(EDS). EDS is used to analyze the chemical make-up of a sample. The basic principle of the EDS process is that as the electrons from the TEM beam pass through the atoms in the sample, there is some probability that they will kick a low atomic orbital electron out of an atom. After the low orbital electron has been removed from the atom, a higher orbital electron will fall down to the lower atomic orbital and release a photon in the X-ray energy range. Each element has a unique X-ray fingerprint associated with this process and making it possible to determine the elements in the sample by the energies of detected X-rays.

Fig.4.9 depicts the resultant X-ray energy spectrum when using EDS on the nanoplatelet shown in Fig.4.8(a). The EDS spectrum is represented as the number of X-rays of different energies that have been observed during the measurement. From this spectrum, the peak matching software of the TEM identified X-ray peaks from Bi, Se, Cu, and C. The Bi_2Se_3 was placed onto a copper grid for measurement in the TEM, which is why there is a copper peak. In order to put the Bi_2Se_3 on the copper grid, they had to be removed by scraping them off the substrates, which is reason for the the small amount of carbon contamination. The sample is otherwise clearly only a composition of Bi and Se with no obvious contaminants. By combining the EDS with the SAED and HRTEM it is shown that the

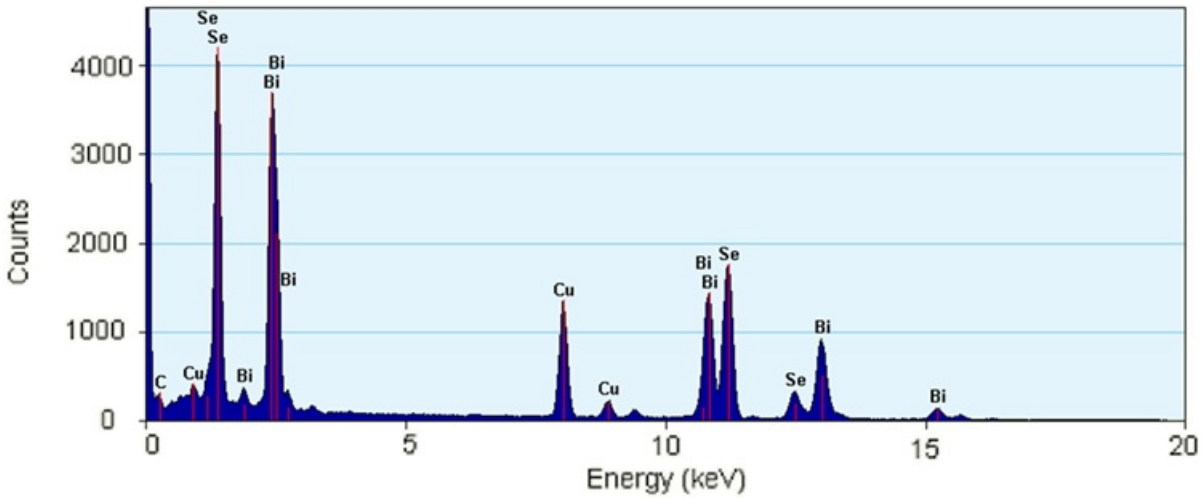

Figure 4.9: Energy dispersive X-ray spectroscopy of Bi_2Se_3 nanoplatelet shown in previous figure, shows clear Bi and Se peaks. The C peak is most likely due to contamination during the measurement process and the Cu is from the copper TEM grid on which the structure was measured.

nanostructures are made of Bi and Se and have the correct crystal structure of Bi_2Se_3.

Chapter 5

Nanoscale Fabrication

The next step after growing the Bi_2Se_3 nanostructures and confirming their material and crystal structure is to make devices out of them. In order to make devices, they must first be placed on a substrate, usually silicon wafers with a 300nm thick SiO capping layer. The wafers are the standard for nanodevice fabrication and can easily be cleaved to any size.

There are two primary ways to get the nanostructures on the substrates: either to grow the nanostructures on the substrate as detailed in the previous chapter, or to sonicate the nanostructures off the growth substrate and into isopropanol(IPA) to keep them in suspension. Typically for nanostructures grown on Si substrates a single growth substrate of 0.7 cm by 0.7 cm is sonicated in 10 mL of IPA in a sealable bottle. If the nanostructures to be used are suspended in IPA, the device substrate must first be cleaved and cleaned using a 5 minute Acetone sonication, 5 minute IPA sonication, and 5 minute bake on a hot plate at 185 °C. After cleaning the substrate, a pipette is used to draw suspended nanostructure

solution and carefully drop the solution onto the substrate. The IPA can dry and evaporate on its own, leaving only the nanostructures on the substrate. IPA does however leave a residue, so it is better to carefully blow on the substrate with a nitrogen gun to hasten the evaporation which reduces the residue left behind. After each drying step, the substrate should be checked under the optical microscope in order to determine if any nanostructures have been deposited. If no nanostructures or very few are on the substrate the drop casting process can be repeated as many times as necessary to achieve desired results. With the nanostructures on a substrate, the next step to be taken is to cover the substrate with resist and perform lithography to shape a future device. It should be noted that all steps where the Bi_2Se_3 is exposed to ambient air should be performed as quickly as possible because a native oxide forms on the surface of the nanostructures [37].

5.1 Lithography

Optical lithography and electron beam lithography were used to make all the nanodevices described in this thesis. Optical lithography is used for larger features (between roughly four micrometers to about several hundred micrometers), and electron beam is used for smaller features.

5.1.1 Optical Lithography

Optical lithography uses ultraviolet light and a mask to write designs in photosensitive resist. The process is depicted in Fig.5.1. It begins by preparing the sample with a 5 minute soak in Acetone, followed by a 5 minute soak in IPA and drying with application of a nitrogen gun. Fig.5.1(a) shows a substrate that has been cleaned, has a nanostructure on it(teal rectangle), and is ready for the resist. After cleaning, the sample is placed in a spin-coater and a three drops of the optical resist S1813 from a pipette are dropped onto the sample. The spin-coater is now set to ramp up to 4000 RPM and will spin at this setting for 45 seconds after which it will ramp down and stop. The fast spinning of the sample forces the drop of resist to spread out on the sample and form a neat layer as depicted in Fig.5.1(b). The faster and longer the spinning, the thinner the layer achieved. The best reference for this is the S1813 datasheet found at the MMT website [47]. The recipe used should achieve approximately a two micron layer of resist on top of the sample and is shown in Appendix A.1. After spinning, the sample is placed on a hotplate set to 115 °C in order to bake and harden the resist.

After baking the sample is ready for lithography. The process works by shining light through a mask projecting the mask pattern onto the substrate through the lense of an optical microscope, depicted in Fig.5.1(c). The resist used, S1813, is a positive resist and thus everywhere that light is not blocked by the mask, the resist polymers there will be degraded. The necessary time for the exposure of the resist to the microscope light is variable and depends on the individual microscope as well as resist baking time and thickness. In order

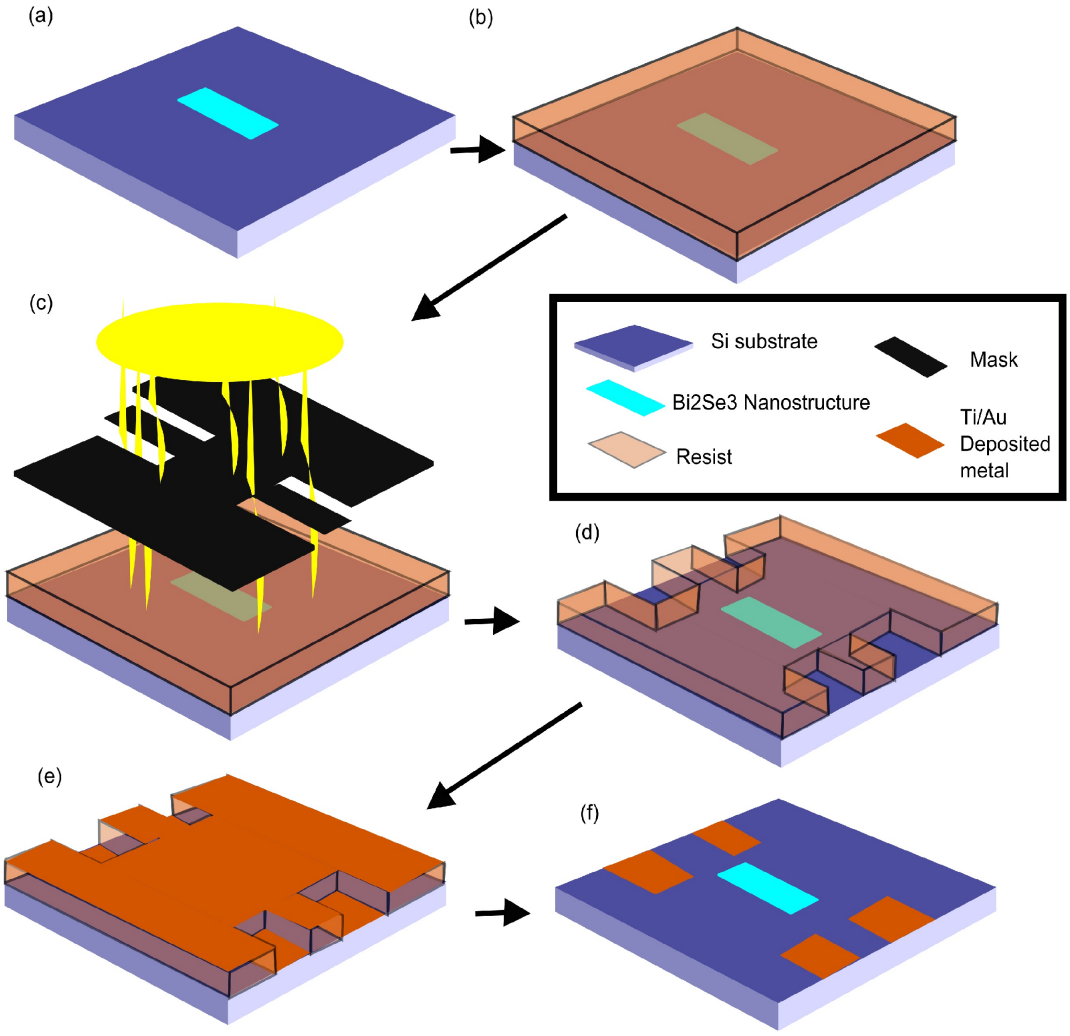

Figure 5.1: Steps involved in optical lithography. (a) Sample with Bi_2Se_3 nanostructure is cleaned with Acetone, IPA, and Nitrogen dried. (b) S1813 optical resist is spun onto the sample. (c) A mask is projected through an optical microscope onto the sample, ultraviolet light breaks down the polymer bonds of areas not masked off. (d) Sample is developed in Microposit 351 removing all exposed resist and leaving pattern etched in the resist. (e) Metal is deposited onto the sample with some making direct contact to the sample and the rest sitting on top of the resist. (f) After metal deposition and leaving the sample overnight in acetone the unexposed resist and metal on top of it have been removed leaving only the desired pattern.

to make devices for this thesis two steps of optical lithography were performed at 10X and 50X magnification, and these recipes are detailed in Appendix A.1.

With the exposure finished the sample is then washed in a developing solution. The developer, in this case Microsposit 351, breaks down and removes the resist from the exposed areas, leaving the projected pattern etched into the resist as shown in Fig.5.1(d). The next step in the process is to deposit metal onto the sample, shown in Fig.5.1(e) and detailed in Fig.5.2. After the metal is deposited, the sample is left overnight in acetone to remove all excess resist. After the overnight acetone bath, an acetone squirt bottle is used to spray the sample to remove any excess metal that is not attached to the substrate surface. The final product looks like that in Fig.5.1(f). Although optical lithography can be used to make contact to larger nanostructures, usually electron beam lithography is required as the next step to connect the nanostructure to the optical leads.

5.1.2 Electron Beam Lithography

Electron beam lithography has many similarities to optical lithography in the basic preparation. The sample has already had optical lead deposited as shown in (Fig.5.2(a)), and coated with resist(Fig.5.2(b)), but instead of using a mask, a beam of electrons writes the designs into the resist, depicted in Fig.5.2(c). The resist used is 950PMMA A4. As the electron beam is scanned over an area of the resist, it breaks the polymer bonds in only the scanned areas, allowing customized designs to be drawn in the resist. This method is able to produce features as small as 10nm. MIBK and IPA, in a ratio of 1:7, are used to

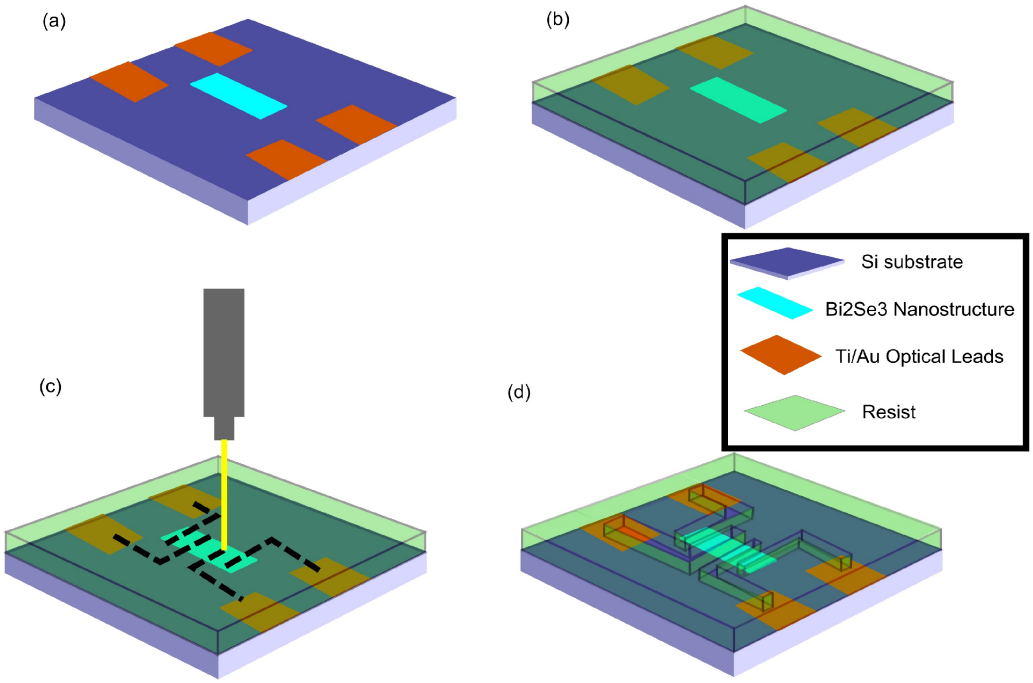

Figure 5.2: Steps involved in electron beam lithography to connect optical leads to the nanostructure to complete the device. (a) Sample with Bi_2Se_3 nanostructure and optical leads is cleaned with Acetone, IPA, and Nitrogen dried. (b) 940PMMA A4 electron beam resist is spun onto the sample. (c) An electron beam is used to draw designs in the resist by breaking down the polymer of any area of the resist that is exposed to the beam. (d) Sample is developed in MIBK and IPA, is a 1:7 ratio, removing all exposed resist and leaving pattern etched in the resist. After this step, metal is deposited and fabrication completed in the same manner as depicted in Fig.5.1(e) and (f).

develop out the scanned pattern, shown in Fig.5.2(d). After the exposed resist is removed, the sample is ready for metal to be deposited in the same manner as depicted in Fig.5.1(e) and (f). After the metal is deposited the sample is left overnight in acetone to remove excess resist and metal.

5.2 Metal deposition

The main purpose of the lithography is to be able to contact interesting nanostructures with metal leads which can then be easily connected to measurement equipment. There are a variety of metals that can be used for these connections. The choice of materials depends on the details of the sample and the deposition process. The two main deposition processes used in this thesis were thermal evaporation deposition and sputtering deposition. The details of these processes will be presented in the following two subsections.

5.2.1 Thermal deposition

Thermal evaporation deposition is a very straight forward process and is depicted in Fig.5.3. The sample, with resist developed, is held upside down in the evaporation chamber, which is pumped down under vacuum. Beneath the sample is a ceramic boat that has been wrapped in tungsten wire and is attached to a power supply outside the chamber. Inside the boat are chunks of the metal that is to be evaporated. The power supply runs current through the tungsten wire and heats the ceramic boat. The temperature of the boat is

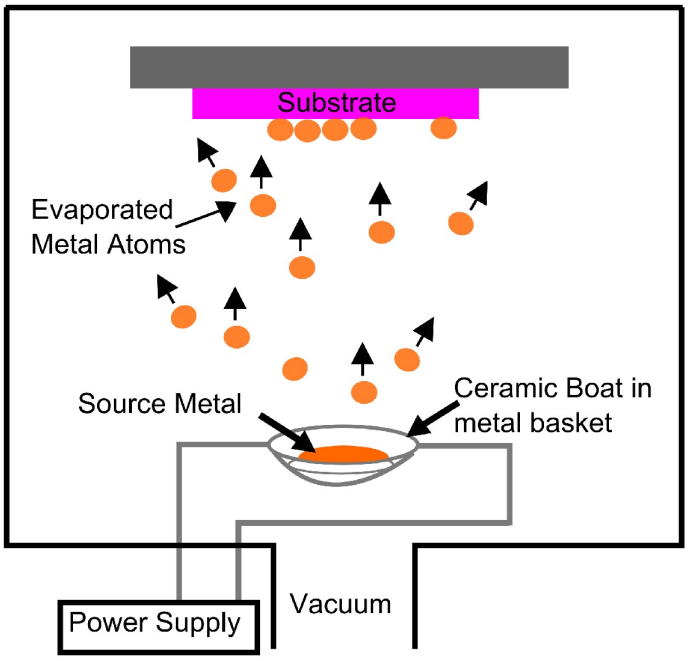

Figure 5.3: Diagram of thermal evaporation process. Sample hangs upside down in chamber under vacuum. Ceramic boat wrapping tungsten wire contains the desired metal. External power supply is used to run current through and raise the temperature of the tungsten wire heating the boat and source metal. When enough current is passed through the tungsten wire the source metal will melt and begin evaporating. The rate and amount deposited is measured by a quartz crystal balance and when the appropriate amount has been deposited the current is turned down and the evaporation stops.

controlled by the current and it needs to be high enough to melt the metal. A shutter serves to block the sample from the evaporation source until a steady evaporation rate has been achieved. This is necessary to protect the sample from outgassing of contaminant materials as the evaporation source is heating up. When the source has reached a steady sample rate as measured by a crystal quartz balance the shutter is opened and metal evaporates and deposits on the sample above. The crystal quartz balance helps to measure not only the rate but also the total amount of deposited material. When the desired amount has been

deposited, the shutter is closed and current from the power supply is turned to zero. The metals typically used in this process for this thesis are gold, titanium, and chromium.

5.2.2 Sputter Deposition

Sputter deposition, depicted in Fig.5.4, is more complicated than thermal deposition but has the advantage of being able to deal with metals with higher melting temperatures. Sputtering is done in a chamber that has been pumped to high vacuum but then the vacuum is lowered by adding argon gas that flows through the chamber. The source metal in sputtering is typically in the form of a disk that is around 5 mm thick and 6 cm in diameter. The source disk is place on a cathode while the sample is attached to an anode. With the argon flowing through the chamber, an external power supply is used to create a high voltage potential from the cathode to anode. The potential causes electrons to be released from the cathode and to bombard the argon gas, ionizing it. The ionized argon gas is then attracted to the cathode and will thus bombard the source material causing source metal atoms to be ejected and to deposit themselves on the sample and the chamber surface. This ejection process means that the material does not need to be taken to a high temperature melting point. The metal which was sputtered in this thesis was palladium.

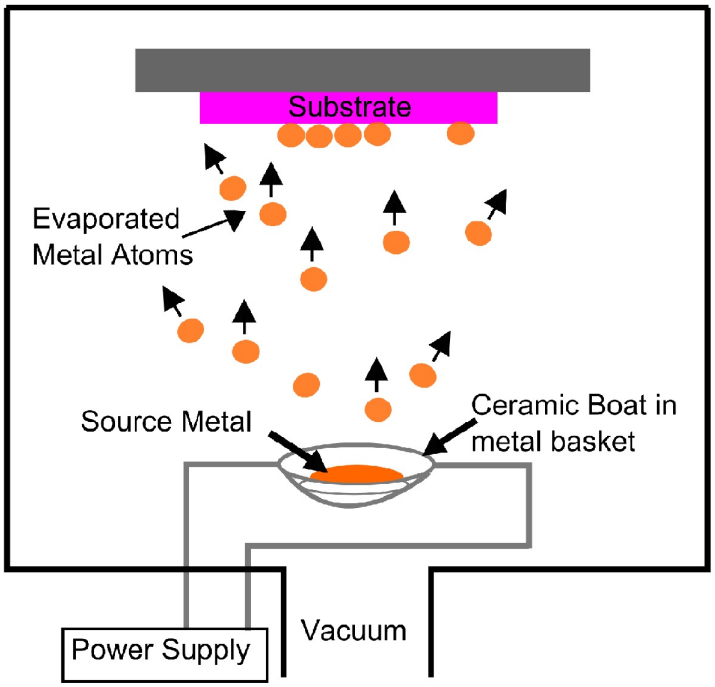

Figure 5.4: Diagram of sputtering deposition process. Argon gas is flowed through a pumped out chamber. A potential is applied from the cathode which has the source metal attached to it and an anode which has the sample attached to it. The potential causes electrons to be released from cathode and to ionize the argon gas. Ionized argon is drawn to the cathode and bombards the source metal. The bombardment causes source metal atoms to be ejected. The ejected atoms deposit on the surface of the sample.

Chapter 6

Low Temperature Transport Measurement

In order observe the topological states, and other quantum mechanical effects, in the catalyst-free nanostructures, they must cooled down to low temperatures where phonons and impurity states are frozen out, and the temperature fluctuations of the system are smaller than the band gap of the Bi_2Se_3. At low temperatures the measurements are designed to look at the movement of electrons in the material to understand individual and collective phenomena they may exhibit in order to better design future devices, experiments, and ultimately technologies. This chapter gives an overview of the concepts involved in cooling these samples to low temperature as well as the basic measurement of them.

6.1 Refrigerators and Operation

In some ways the refrigerators used to reach the necessary sub-kelvin temperatures are similar to ordinary refrigerators in a house. Both use a liquid coolant and system of pumps to help move heat from inside the fridge to outside the fridge and both require proper insulation to isolate them to maintain their base temperatures. The two primary types of fridges used in for the measurements in this thesis were Helium-3 refrigerators and Dilution refrigerators and will be covered in the next two sections. In both cases the refrigerators are in in the form of a self contained complete assembly that sits inside a liquid Helium dewar and can be swapped out as necessary without warming the dewar.

6.1.1 Helium-3

A Helium-3 fridge insert is depicted already inside a dewar in Fig.6.1. The insert sits in a main bath of liquid helium. The main bath is in turn surrounded by a nitrogen jacket, which lessens boil-off and then an outer vacuum chamber(OVC) pumped to very high vacuum, which serves to help further isolate the nitrogen and helium from outside heat sources. The sample and main elements of the fridge sit in the inner vacuum chamber(IVC) designed to be thermally isolated from both ambient room temperature and the liquid helium main bath. Initially, in order to cool everything in the IVC from room temperature to 4.2K a small amount of helium exchange gas is used to act as a temperature mediator between fridge elements and the IVC and liquid helium main bath. This system uses Helium-3 as its

coolant to get to the base temperature. The helium is stored permanently in the helium-3 line and helium dump in the insert, and never opened to atmosphere due to the fact that it is expensive and hard to obtain. The operation of the fridge begins when the whole insert has been placed in dewar and has been allowed to reach 4.2K, at which point the exchange gas is pumped out of the IVC. At this first base temperature a pickup tube equipped with a needle valve is used to draw liquid helium from the main bath into a chamber referred to as the 1K pot. When the pot is full, as measured by its internal pressure, the needle valve is carefully adjusted as the pump begins to draw on the 1K pot. Carefully balancing the in-flow of liquid helium with the the helium evaporating and being pumped out cools the 1K pot below 2K. The exact temperature of the 1K pot is different for different fridges, but is usually around or below 1.6K if the fridge is operating properly.

With the 1K pot below 2K, the He3 Sorb is activated and set to a temperature of 30K. The heating from the sorb causes helium-3 to de-sorb and be cooled by the 1K pot and to condense in the helium-3 Pot. When the helium-3 has completely condensed, the He3 sorb is turned off. After the sorb is off, the temperature off the Helium-3 pot should drop to base temperature, which for most systems is around 300mK, though sometimes lower. At this point the sample, which is thermally anchored to the Helium-3 pot is being evaporation cooled by the boil off of the helium-3. When the liquefied helium-3 has completely boiled off, the temperature of the Helium-3 pot and sample will rise above 1K and the cooling process will need to be repeated from the beginning, i.e. the heating of the sorb. The length of time the fridge stays cold is related to how much helium-3 was condensed and can last

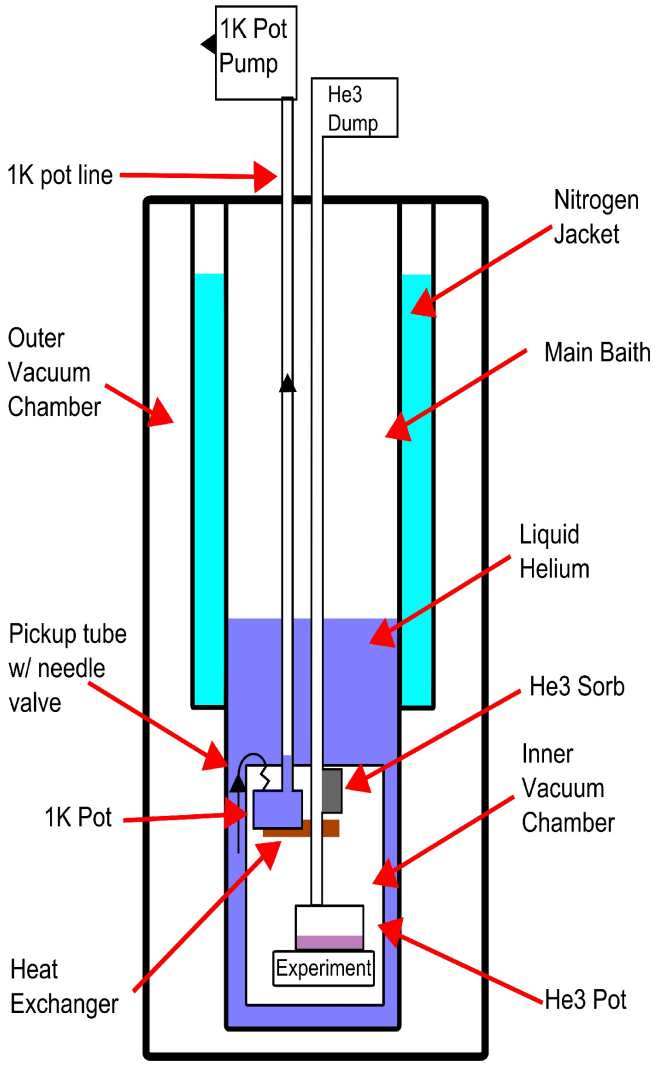

Figure 6.1: Diagram of Helium-3 refrigerator showing primary parts used for cooldown.

anywhere from a couple of minutes to a couple of days.

6.1.2 Dilution Refrigerators

Dilution refrigerators are useful for when 300mK is not cold enough, reaching temperatures typically on the order of 10 to 20 mK. A diagram of a dilution refrigerator is shown in Fig.6.2. Similar to the Helium-3 fridge, exchange gas and a 1K Pot system is used to get the fridge and the coolant to below 2K. In the case of a dilution refrigerator, the coolant is a mixture of helium-3 and helium-4 and is used in a closed-cycle system that never exposes the mixture to atmosphere. The mixture is stored in an external tank when the system is not being used. Operation of the dilution refrigerator begins with using the 1K pot to cool the mixture below 2K to condense the mixture. With the mixture condensed, the cooling process begins by pumping on the still line using a closed-cycle pump. The closed-cycle pump then forces the mixture through external liquid nitrogen traps which remove any impurities from the mixture. The mixture then re-enters the fridge through the condenser line. The condenser line is in thermal contact with the 1K pot, and contains a very narrow tube, called the impedance. The impedance helps to control the flow of helium-3 through the system. As the condensed helium travels through the impedances, it is cooled by the helium in the still. This lowers the temperature of the helium in the condenser impedances below the tri-critical point at 0.86K to the region where the mixture will separate into a He3-rich phase and a He4-rich phase.

This phase separation is necessary to cool the fridge down to sub-100mK temperatures.

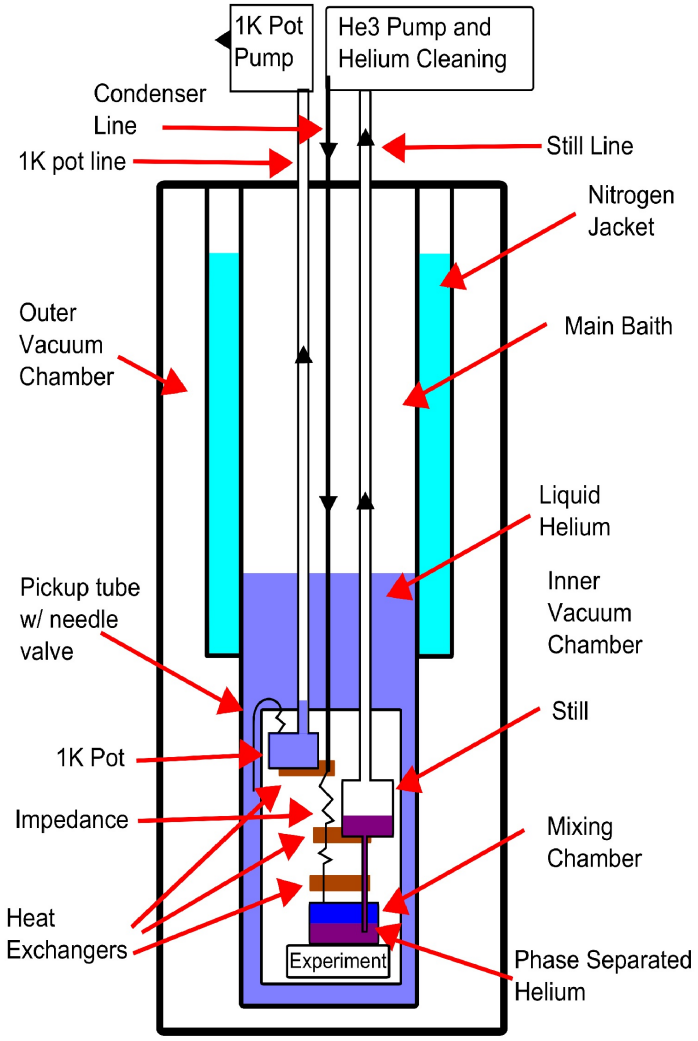

Figure 6.2: Diagram of dilution refrigerator showing primary parts used for cooldown.

The He3-rich phase is lighter and has a higher partial pressure than the He4-rich phase. As the closed-cycle pump pumps on the still, it extracts mainly the He-3 rich phase, while the He4-rich phase is mostly stationary. At the phase boundary between the two isotope liquids, the moving of a helium-3 atom through this boundary is endothermic and what provides the cooling power. After passing through the phase boundary and into the still, the He3 evaporates and is pumped out, cooling the helium in the impedance, and begins the process anew. Because this process constantly flows helium-3 through the mixture, a dilution refrigerator can effectively stay cold indefinitely, which is another advantage over the Helium-3 fridge, although a dilution refrigerator is more complicated in overall operation. A useful source for further information and specific operations on running a dilution refrigerator can be found in "The Hitchhikers Guide to the Dilution Refrigerator", written by N. Craig and T. Lester in 2004 [48].

6.2 Basics of transport measurements

In any refrigerator system there are also electrical lines that start from an external break-out box attached to the top of an insert and extent down, and are electrically connected, to the sample. It is through these electrical lines that electron transport in the sample is probed. Two ways of passing electrons through and measuring the sample properties are via current biasing and voltage biasing. For either measurement the properties are measured as the response of the resistance, or sometimes conductance, of the sample to changes in parameters

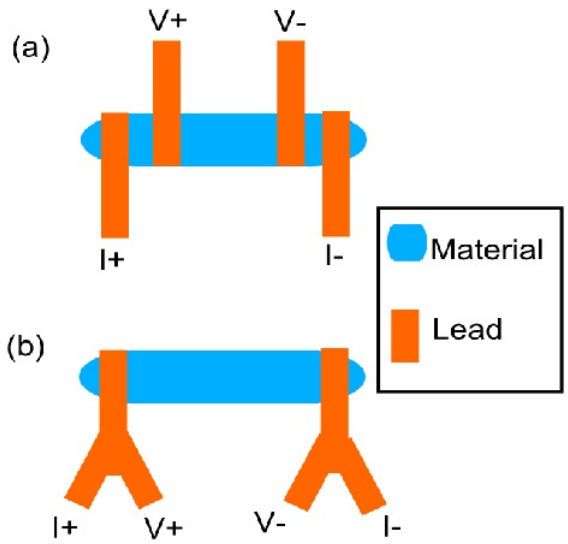

Figure 6.3: (a) Diagram of 4-probe measurment. (b) Diagram of 2-probe measurement.

in and around the sample such as temperature, magnetic field strength, an applied electric field, or even to the magnitude and/or sign of the biased voltage or current. The next two subsections give a brief overview of the two biasing techniques.

6.2.1 Current Bias

Current bias measurement means applying a constant current through a sample and measuring the voltage drop across it. When the magnetic field, temperature, or gate voltage on a sample is changed the changes in the resistance in the sample will be observed as a change in voltage. In the case of measuring the transport properties of an individual material, it is the best measurement to make when used in a four probe configuration.

A four-probe measurement is shown in Fig.6.3(a), it consists of four leads contacting

the material or device of interest with the current being sourced from one outer lead to the other and two inner leads are measuring the voltage drop across an individual region of the material. This configuration allows for the resistance caused by the contact between a lead and the material as well as the resistance of the leads themselves to be ignored. This means that the measured resistance is purely based on the current running through the material and the resistance of the material itself. For a superconducting material, it is the best way to understand how much of the material has transitioned into a superconducting state.

This setup can also be used in a three or even two probe configuration. A two probe configuration is shown in Fig.6.3, where the outer current lead and nearest inner voltage lead may be combined for both sides or one side of the device. However, this will add lead and contact resistances which, although they may not affect the qualitative observations, will affect the quantitative analysis of the material.

6.2.2 Voltage bias

The opposite, and sometimes necessary measurement, is a voltage biased measurement shown in Fig.6.4. This measurement involves applying a voltage bias across the device and putting an ammeter in before the device ground. This measurement is useful when gating a device and depleting the number of carriers. As the number of carriers is depleted, the resistance increases drastically. If the device is current-biased, then the voltage across it will sky-rocket, potentially damaging the device. A voltage bias measurement will keep the voltage constant and the change in resistance will be noticed as a decrease in current

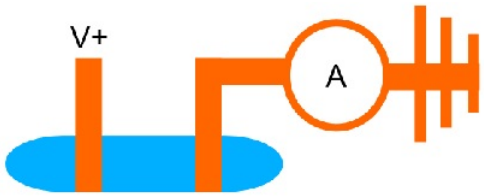

Figure 6.4: Diagram of voltage bias measurement which puts an ammeter before the ground.

which is perfectly fine for the device.

Chapter 7

Electron transport in Bi_2Se_3 nanostructures

Having grown and fabricated devices from the catalyst-free Bi_2Se_3 nanostructures, it is now time to check their transport properties at low temperature. This chapter will detail electron transport measurements from two different samples, a nanoribbon and a nanowire. The two devices will be referred to as Device 1 and Device 2, and are displayed in optical images in Fig.7.1 (a) and (b) respectively.

Device 1, Fig.7.1(a), is a nanoribbon that is approximately 15 microns long and 3 microns wide with palladium metal leads. Device 1 was designed to allow for Hall measurements using the leads designated 3, 4, 5, and 6. The measurements for Device 1 had current driven through leads 1 and 2 and voltage measured between 5 and 6 for longitudinal resistance, and voltage measured between 4 and 6 for the Hall resistance. Device 2, Fig.7.1(b),

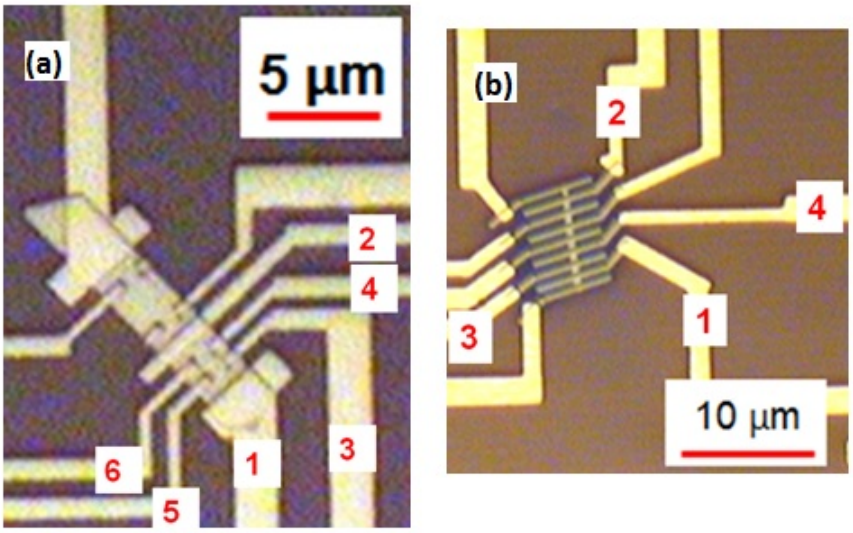

Figure 7.1: Optical images of Bi_2Se_3 nanodevices. (a) Image of nanoribbon device with palladium leads in a Hall measurement configuration and referred to as Device 1. Current is driven through leads 1 and 2 and voltage was measured between 5 and 6 for longitudinal resistance and between 4 and 6 for Hall resistance. The leads of this device are made of Pd for the e-beam leads and Cr/Au for the optical leads. (b) Nanowire device referred to as Device 2. Current was driven through leads 1 and 2 and voltage was measured between 3 and 4. A focused ion beam was used to remove the oxide layer on the nanoribbon and to deposit platinum leads. The Pt leads were connected to Cr/Au leads by Pd.

is a nanowire device that had platinum leads deposited using a focused ion beam after the beam was used to clean the surface. Palladium leads connect the Pt leads to the Cr/Au optical leads. The measurement configuration on Device 2 had current supplied between leads 1 and 2 and voltage measured between 3 and 4. For both devices, the resistance versus temperature, voltage gating, and magnetoresistance are measured and shown together to compare and contrast the two devices. Using the the Hall configuration on Device 1, this chapter also includes measurement of the Hall properties of Device 1.

7.1 Resistance versus temperature

Fig.7.1 (a) and (b) shows the resistance versus temperature(R-T) measurements of Device 1 and Device 2 respectively. Device 1 was cooled to 4.2K and Device 2 was measured from 1.5K to 0.3 K. In both figures, there has been an increase in resistance as the temperature is increased. For Device 1, the R-T starts with a decrease in resistance with decreasing temperature until 14K. Below 14K there is a change from metallic to insulating behavior as the resistance starts to increase with the decreasing temperature. Device 2 shows incomplete insulating behavior. Although the resistance increases with decreasing temperature, the resistance begins to plateau around 600 mK. The change from metallic to insulting behavior in Devices 1, and the plateau in Device 2, indicate that although some free carriers are freezing out at low temperatures, there are still conduction channels in the material. For Device 1 especially, the small increase in resistance after the upturn indicates that there is

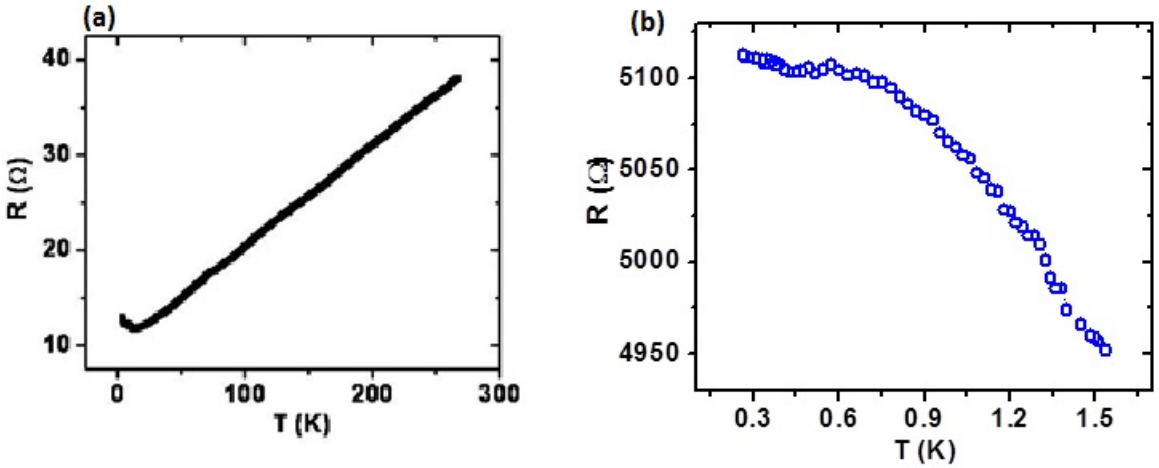

Figure 7.2: Resistance versus temperature(R-T) curves for Bi_2Se_3 Devices 1 and 2, (a) and (b) respectively, measured down to 4.2K and 250 mK respectively. (a) The resistance in Device 1 shows a decrease in resistance with decreasing temperature. The downward trend changes below 14K, showing a change from metallic to insulating behavior. (b) Device 2 shows increasing resistance with decreasing temperature in the low temperature regime. The resistance begins to plateau below 0.6K showing that the device is not fully insulating.

still a significant contribution from the bulk.

7.2 Voltage gating

With the samples at low temperature and in an insulating regime, it is important to look at the response of the resistance when the Fermi level is tuned with an applied electric field. The electric field is supplied by backgating the sample. The results of backgate sweeps for each sample are shown in Fig.7.1 (a) and (b) for Devices 1 and 2 respectively. For both devices the carrier concentration is tunable with an applied electric field, although for Device 2 the response is very weak. Each device also shows a resistance peak around

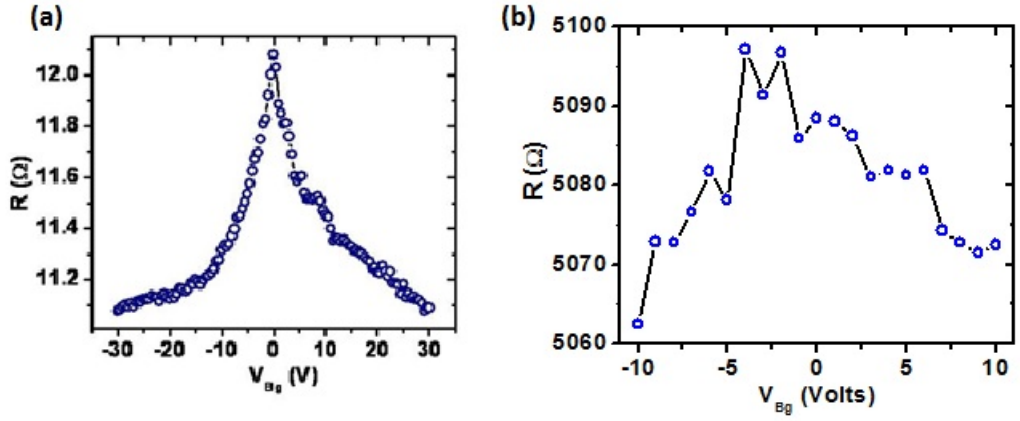

Figure 7.3: Resistance as function of backgate voltage for both Bi_2Se_3 Devices 1 and 2 in (a) and (b) respectively, measured at 4.2K and 250 mK respectively. Both plots show that the carrier concentration in each device can be tuned by an applied electric field. The peak in both plots also shows that the devices are near the Dirac point and thus in the topological regime.

0V for Device 1 and -2.5V for Device 2, this peak indicates the location of the Dirac point, a signature of the existence of a topological surface. One caveat from these plots is that a switchover from electron to hole carriers is not observed as would be expected. A reason the switchover is not observed may be that the back-gate is only affecting part of the device. The bottom surface states and bulk states are most likely being tuned, but the top surface and bulk states are unaffected, creating an overall electron carrier background signal [49–52]. It is also possible that there is local band bending of the Bi_2Se_3 due to nearby oxides [50, 53]. A solution to potentially remove this problem would be to simultaneously gate from the top and bottom of the nanostructure.

7.3 Magnetoresistance

The next knob that can be turned to better understand these devices is to apply a perpendicular magnetic field. For a strong spin-orbit material such as Bi_2Se_3, the effect of weak antilocalization should be observable as a resistance dip around zero field at low temperatures. Fig.7.4 (a) and (b), Device 1 and 2 respectively, show the resistance response to an applied magnetic field. Device 1 being measured at 4.2K does not show a WAL dip, it most likely has not been sufficiently cooled so that the quantum mechanical effects are observable. It instead shows a parabolic magnetoresistance curve, this is further indication that there is still bulk conduction [54]. Device 2 shows more refined curvature that is less parabolic, but still does not show the characteristic dip of WAL. The lack of sharp dip in Device 2 could be due to structural damage from the application of the FIB leads or bulk contributions as with Device 1 and as in Chen et. al. [54] which shows the change in WAL as the thickness of Bi_2Se_3 increases.

7.3.1 Hall properties

In order to understand the nature of the carriers in the nanostructure, the next aspect to look at is the Hall response of the nanoribbon. The basic theory behind the Hall effect starts with applying a magnetic field perpendicular to a thin conductor with current flowing in the plane of the conductor. The magnetic field applies a force on, and perpendicular to, the current, but in the plane of the thin conductor. In a conducting ribbon, with current flowing

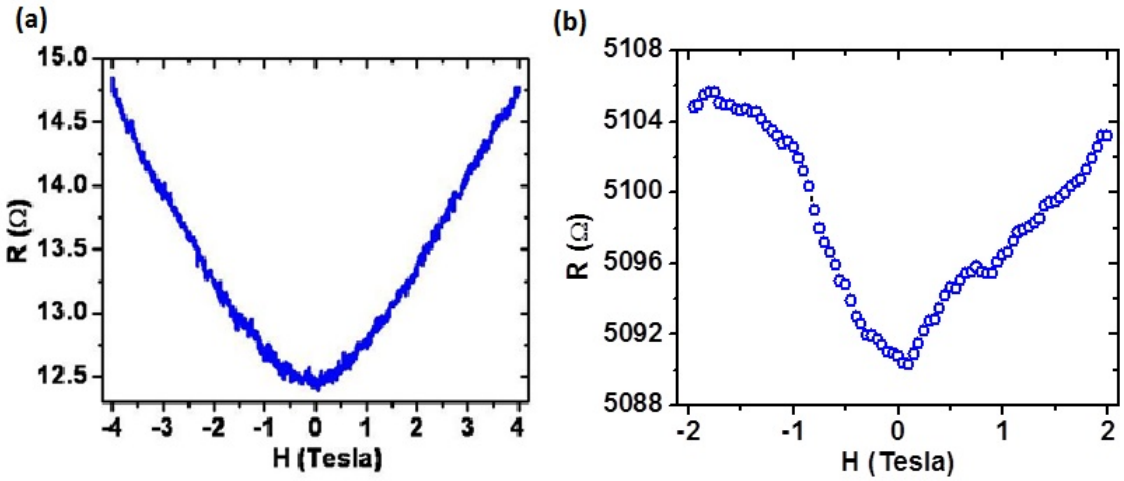

Figure 7.4: Perpendicular field magnetoresistance measurements for Devices 1 and 2 in (a) and (b) respectively, measured at 4.2K and 250 mK respectively. (a) Magnetoresistance measurement shows increase of the resistance in increasing magnetic field. (b) Resistance as a function of magnetic field shows positive magnetoresistance.

length wise, this force will cause a buildup of opposite charges on each long side of the ribbon. The buildup of charge leads to a net potential gradient that is oriented perpendicular and in plane to the current flow and can be measured. This overall effect is called the Hall effect. The strength of the potential depends on the concentration of carriers in the material, and can be defined by the Hall coefficient which is inversely proportional to the carrier concentration. The Hall coefficient of Device 1, R_H, as a function of applied back-gate voltage, is shown in Fig.7.5. A dip in R_H is observed around zero voltage, this is indicative of a minimum in carrier concentration in the material. This measurement compliments the results of Fig.7.3(a), which also showed tunability in the carrier concentration with a minimum around 0V. The plot of R_H also shows a lack of switchover from electron to hole

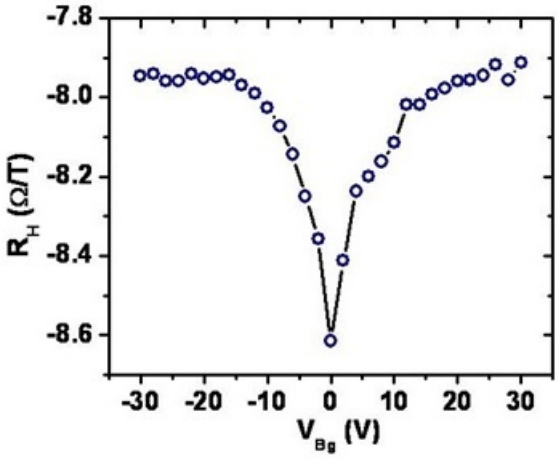

Figure 7.5: Hall coefficient as a function of back-gate voltage for Device 1 shows dependence on the back gate.

carriers, which again may be due to the fall off of the backgate's ability to tune the device, or band bending effects.

7.3.1.1 Two carrier conductance

In measuring the carrier concentration of Device 1 via Hall measurements it is also possible to take the analysis one step further. 7.6(a) shows the Hall resistance or R_xy, measured Hall voltage divided by source current, as a function of magnetic field. Although R_xy at first looks linear as a function of magnetic field, closer observation shows a small amount of curvature. By converting R_{xy} into conductance, G_{xy}, this nonlinearity becomes far more apparent and is shown as the blue data points in 7.6(b), where G_{xy} is calculated

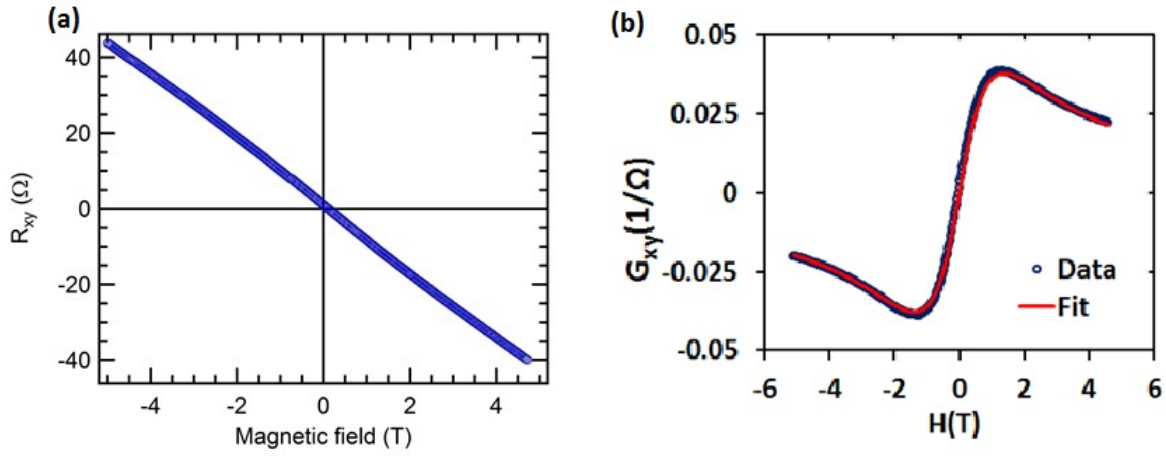

Figure 7.6: Latitudinal magnetoresistance and calculated magnetoconductance of Device 1. (a)Latitudinal resistance shows mostly linear response to application of a magnetic field, but there is a small amount of non-linearity meaning a conversion to magneto conductance is more appropriate, shown in (b). (b) Latitudinal magnetoconductance data from Bi_2Se_3 Device 1, blue circles, fitted with two carrier conductance model, red line. The fit produced carrier concentrations of n1 = 7.8e+12 and n2 = 6.0e+13 cm^2.

form the conductance tensor and is:

$$G_{xy}(B) = -\frac{R_{xy}(B)}{(R_{xy}(B)^2 + R_{xx}(B)^2)} \tag{7.1}$$

The nonlinearity in G_{xy} arises when there is more than one conductance channel in a material [55], and can be modeled as:

$$G_{xymodel}(B) = eB(\frac{c_1\mu_1 - c_2}{(\frac{\mu_1}{\mu_2} - 1)(1 + \mu_2^2B^2)} + \frac{c_1\mu_2 - c_2}{(\frac{\mu_2}{\mu_2} - 1)(1 + \mu_1^2B^2)}) \tag{7.2}$$

where c_1 and c_2 are parameters extracted from the data and are:

$$c_1(B = 0) = \frac{G_{xx}(B = 0)}{e} \tag{7.3}$$

and

$$c_2 = \lim_{B\to 0} \frac{G_{xy}(B)}{eB} \tag{7.4}$$

the free parameters are then the mobilities of the two conductance channels, μ_1 and μ_2. After fitting the data, the mobilities, c_1, and c_2 can be used to calculate the carrier concentrations of each channel n_1 and n_2:

$$n_1 = \frac{c_1\mu_2 - c_2}{\mu_1\mu_2 - \mu_1^2} \tag{7.5}$$

and

$$n_2 = \frac{c_1\mu_2 - c_2}{\mu_1\mu_2 - \mu_2^2} \tag{7.6}$$

This fit is performed on the G_{xy} curve(blue) in Fig.7.6(b), and results in the fit curve(red). The two carrier concentrations obtained from this fit are n_1 = 7.8e^{12} and n_2 = 6.0e^{13} in units of 1/cm^2. The values compare well to values obtained by N. Bansal et. al. [55] for MBE thin films, and can be similarly interpreted to represent the existence of not only the topological surface state, in this case n_2, but also an underlying two dimensional electron gas that exists in the bulk, n_1. The fitting of G_{xy} continues to reinforce the idea that when the device is being tuned there is more than one conductance channel that is being manipulated, meaning that a change in carrier sign in Fig.7.3(a) would, as observed, be obscured by other conductance contributions.

7.4 Mica transport

Looking at the nanoplatelet layers grown on mica substrates, basic electron transport was measured on a sample to show that the layers are in fact contiguously covering the substrate. In order to measure the resistance of a large portion of a sample, thin copper wires

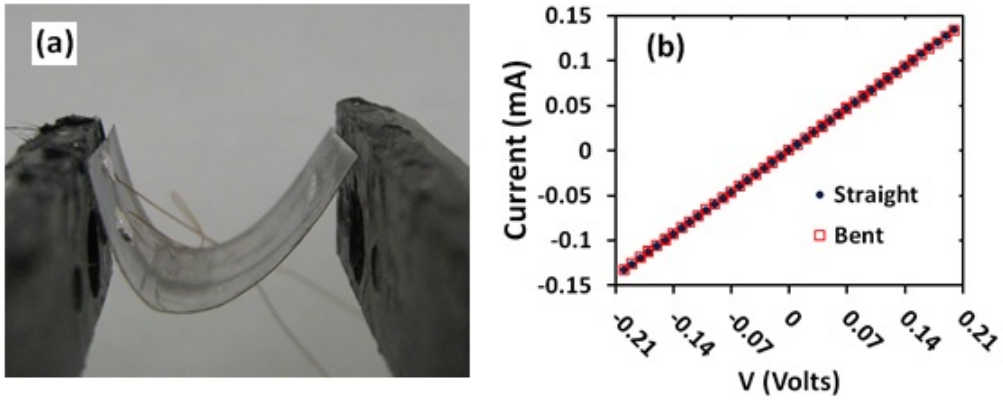

Figure 7.7: Image and data of Bi_2Se_3 mica sheet device where Bi_2Se_3 nanoplatelets cover large portions of the substrate contiguously. (a) A photograph of a flexible mica substrate with a Bi2Se3 film grown on top and bent using a vice. Electrodes are indium pads, attached by silver paint. (b) I-V characteristics of the Bi_2Se_3 film on the straight mica substrate (black circles) and on the bent mica substrate (red open squares). Change in the resistance was minimal: the average resistance on straight mica was 1.499 kΩ, and the average resistance on bent mica was 1.501kΩ.

were attached using indium at two points on a region that has an area completely covered with nanoplatelets. The platelet layer device being bent in a vice is shown in 7.7(a) with the two leads on the left hand side of the mica sheet. The current vs. voltage was measured both with the mica sheet laying flat and as depicted in 7.7(a) when slightly bending the sheet. This measurement was done to see what effect stress has on the conductivity of the nanoplatelet layer, similar to the work in Peng. et. al. [56]. The results of the I-V measurements are shown in 7.7(a). The bent results are shown as red squares and the flat as blue circles. In converting the I-V plots to resistance, there is very little change in between the bent and unbent states, R_{bent} = 1.501 kΩ and R_{flat} = 1.499 kΩ respectively. The small change in resistance in concurrent with Peng et. al., as the resistance did not significantly

change when the mica was placed under stress..

Chapter 8

Superconductivity in Bi_2Se_3 via doping

As mentioned in Chapter 3, Majorana fermions have been predicted to exist in devices which combine the topological insulator surface states with superconductivity. For Bi_2Se_3, there are two ways to accomplish this: by utilizing the proximity effect [57–62] or by doping the Bi_2Se_3 to make it intrinsically superconducting [63, 64]. The doping method is the subject of this chapter, and it is accomplished using two different dopants, copper and palladium. There are also three methods used to dope samples, thermal annealing pre-doped materials, voltage pulse annealing un-doped materials, and thermal annealing un-doped materials.

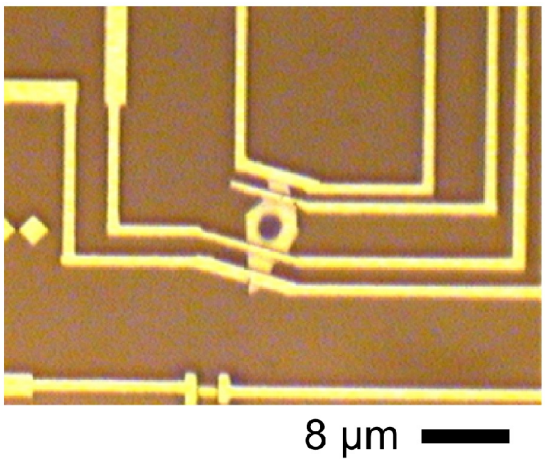

Figure 8.1: Optical image of copper-doped Bi_2Se_3 sample that was mechanically exfoliated from a bulk crystal with a circle etched into its center by focused ion beam.

8.1 Cu Doping

Copper doped Bi_2Se_3 was first shown to be superconducting in 2010 by Y. S. Hor et. al. [63]. The formulation that showed the best superconducting properties was $Cu_{0.12}Bi_2Se_3$ which had a T_c of 3.8K. However, the copper tends to leech out to the surface of $Cu_xBi_2Se_3$ at room temperature and ambient pressure, this destroys the superconductivity in the material. There is a possibility that thermal annealing could repair this, causing the bulk of $Cu_xBi_2Se_3$ to take up the copper from the surface. If the sample is then measured at low temperatures, the superconductivity should be recovered. Fig.8.1 shows a sample that underwent this exact process. The nanodevice in Fig.8.1 was fabricated from a bulk $Cu_{0.12}Bi_2Se_3$ crystal grown by John Sheckleton, of the McQueen group at Johns Hopkins. The nanoflake was obtained using the mechanical exfoliation method to apply it to a silicon substrate with a 300nm thick SiO capping layer. The circle etched in the center of the

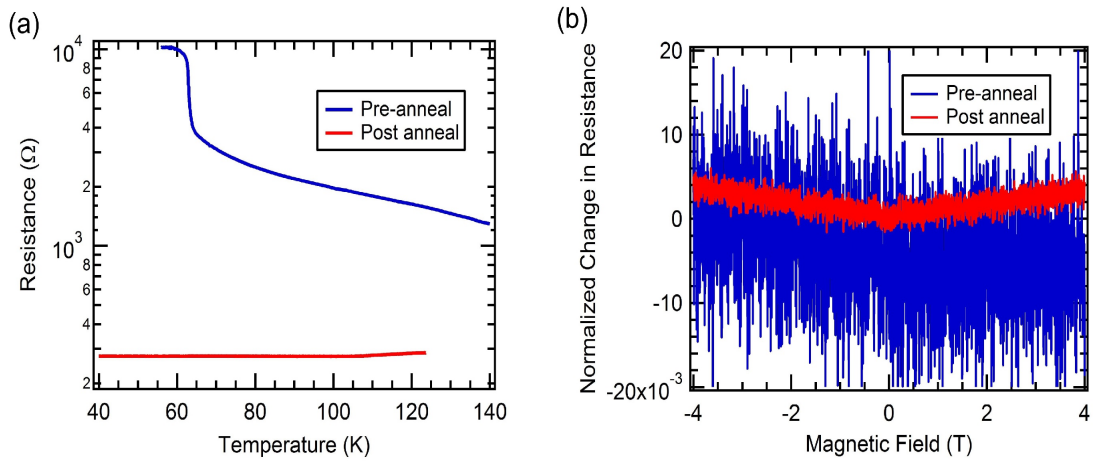

Figure 8.2: Results from a device shown in Fig.8.1, comparing measurements before and after thermal annealing. (a) Resistance versus temperature of the device, showing that the resistance significantly decreased from before annealing(blue) by over an order of magnitude after being annealed(red). (b) Normalized change in resistance as a function of magnitude of before annealing(blue), and after annealing(red). There is a clear change in the magnetoresistance, before annealing the response was negligible and largely noise, versus after annealing where a parabolic metallic shape can be resolved.

device was made using a focused ion beam. The sample was measured twice, once before annealing and once after. The thermal annealing process involved placing the sample in a quartz tube in a tube furnace under argon gas. Before annealing the tube was flushed with argon at a flow rate of 1600 sccm for 30 minutes, this cleared the tube of potentially contaminating gases. After the tube was flushed, the flow rate was reduced to 200 sccm for the annealing process. The furnace was set to 200 °C and held at the set temperature for 1 hour, then allowed the cool naturally with the argon still flowing. After the annealing step, the sample was immediately put into the He3 refrigerator, pumped down, and cooled to 4K.

The results of measuring the sample before annealing(blue), and after annealing(red),

are shown in Fig.8.2. The figure shows both the resistance as a function of temperature, Fig. 8.2(a), and the effect of an applied magnetic field 8.2(b). In the resistance versus temperature curve, we see insulating behavior before annealing, giving a resistance above 10kΩ below 60K. Post annealing, the resistance has dropped by over an order of magnitude, and follows a curve that more resembles a metal. Unfortunately, due to a leak in the 1K pot of the He3, the sample was not measured below 4.2K for either sample. The stark difference between pre- and post-anneal is also apparent in the change in the normalized magnetoresistance, Fig.8.1(b). The pre-anneal data show no real response to magnetic field, being essentially noise. Post-anneal data show a small parabolic trend in the resistance, pointing to a now metallic material, more in line with a device that could go superconducting. These data show that the annealing process has a positive impact on the conductivity in the device, and may have the potential to restore superconductivity.

8.2 Pd Doping I: Voltage Pulse Annealing

An alternative to working with copper-doped Bi_2Se_3 is to develop nanostructures of a different material. Heavily palladium-doped Bi_2Se_3, in the form of $Bi_2Pd_3Se_2$, was discovered to be superconducting in 2008 by T. Sakamoto et. al. [65] and several variations of Pd_xSe_y, discovered by T. Takabatake et. al. [66] have shown superconducting properties as well, making palladium an interesting doping element for Bi_2Se_3. In order to explore this space, lessons from copper thermal annealing were combined with palladium to develop a

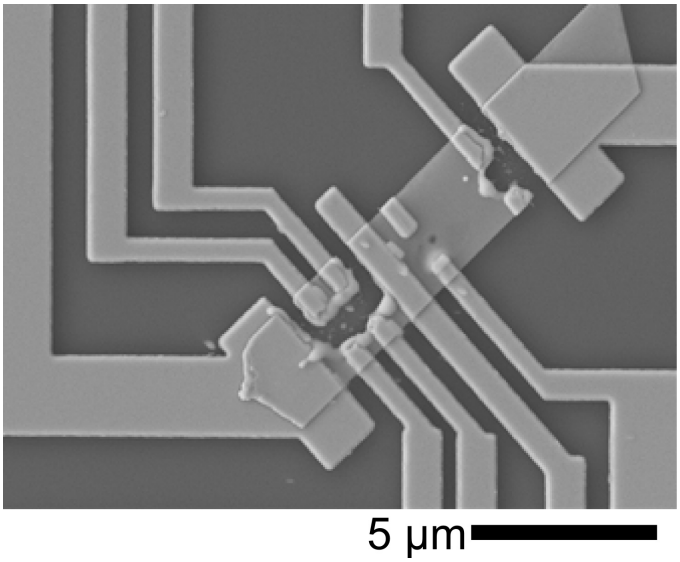

Figure 8.3: SEM image of voltage pulse annealed device. The region which was voltage pulse annealed is boxed in red. The resistance was measured in a four-probe configuration, with current supplied from 1 to 2 and voltage measured from 3 to 4.

new way to dope Bi_2Se_3 and induce superconductivity.

The first method used to achieve this goal was voltage pulse(VP) annealing. The goal of VP annealing is to apply a high voltage pulse to part of the device to increase the temperature and cause it to absorb the desired material. Fig. 8.3 shows a device that has undergone this process. It should be noted that this was originally the same device depicted in Fig.7.1(a). The primary affected region is boxed in red, showing partial destruction of the device, but also fusion of the materials. The device leads are palladium, with a post annealing patch of platinum on the upper sides of the leads on the nanostructure. Measurements on this device were four-probe, current was supplied from 1 to 2, and voltage measured from 3 to 4, as depicted in the figure. The basic transport data for the VP annealed device, measured in a He3 refrigerator, is shown in Fig.8.4. The resistance versus

temperature curve is shown in Fig.8.4(a), and covers the temperature range of 4.2K to 250 mK. A superconducting transition is observed to occur at 1.2K. The resistance does not go to zero, which means that part of the measured portion is still a normal conductor. The resistance does, however, continue to decrease with decreasing temperature and the decrease begins to accelerate again below 500 mK, depicted in Fig.8.4(b). The acceleration in decreasing of resistance could be an indication of the beginning of a second transition. As mentioned previously, there are several Pd, Se, and Bi compounds which go superconducting and could explain some of the data. The doping of the Bi_2Se_3 may not be uniform, giving the possibility for strictly normal regions as well as regions with the correct doping amount of one, or more, of the potential materials.

The magnetoresistance curve taken at 250 mK, shown in Fig. 8.4(c), indicates that the critical field is approximately B_C=1.6T. There is no indication of WAL in the sample around zero field and no obvious indication of a second transition at low fields.

8.2.1 Differential Resistance

To better understand the nature of the superconductivity in the VP annealed sample, we look at the superconducting gap by looking at the current dependence of the voltage(V-I) and its derivative(dV/dI). Fig. 8.5 shows the current versus voltage curves for the sample as a function of temperature. As expected, based on the R-T curve, the device never truly shows a flowing current without voltage, but the transition from the low resistance, of 1.5Ω, to the normal region, of 30Ω, does show that the device is at least partially superconducting.

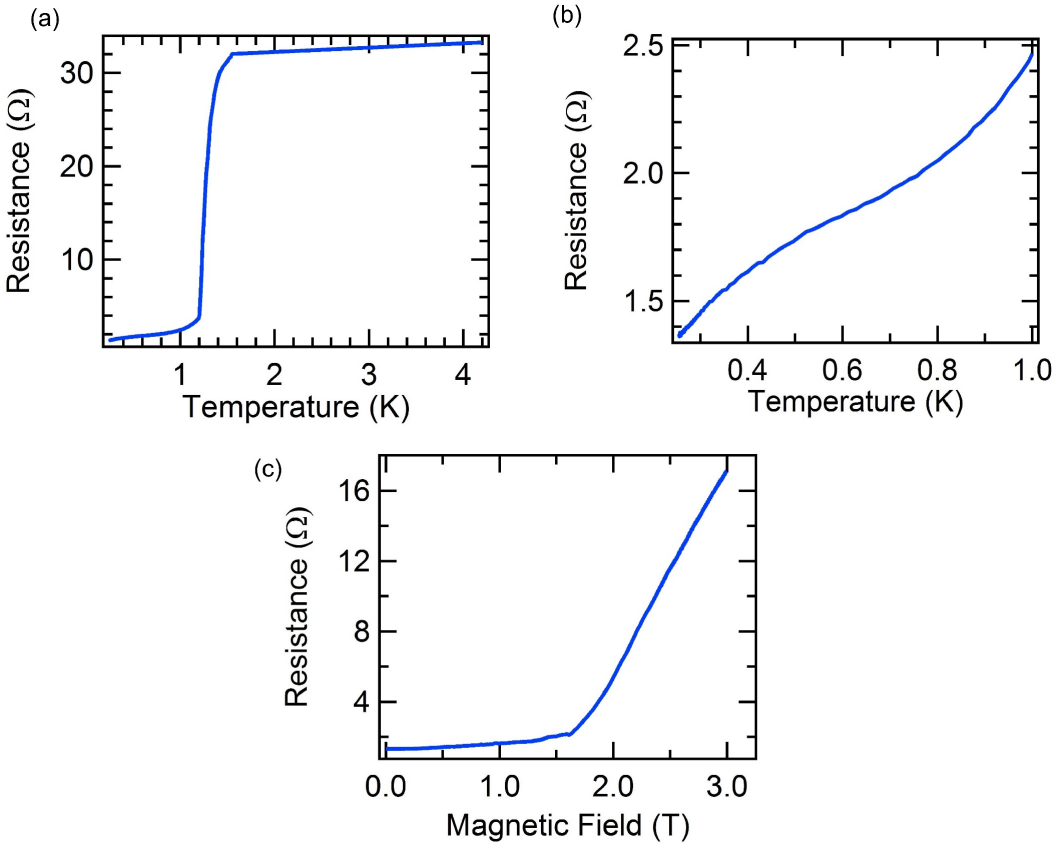

Figure 8.4: Four-probe resistance measurements of voltage pulse annealed device shown in Fig.8.3. (a) Resistance versus temperature(R-T) curve shows a superconducting transition around 1.2K. (b) Zoomed in view of (a), covering temperature region of 250 mK to 1K, a possible second transition is observed below 500 mK indicated by an acceleration of the decrease in resistance. (c) Resistance versus magnetic at 250 mK. Curve shows superconducting-like properties with critical field B_C=1.6T

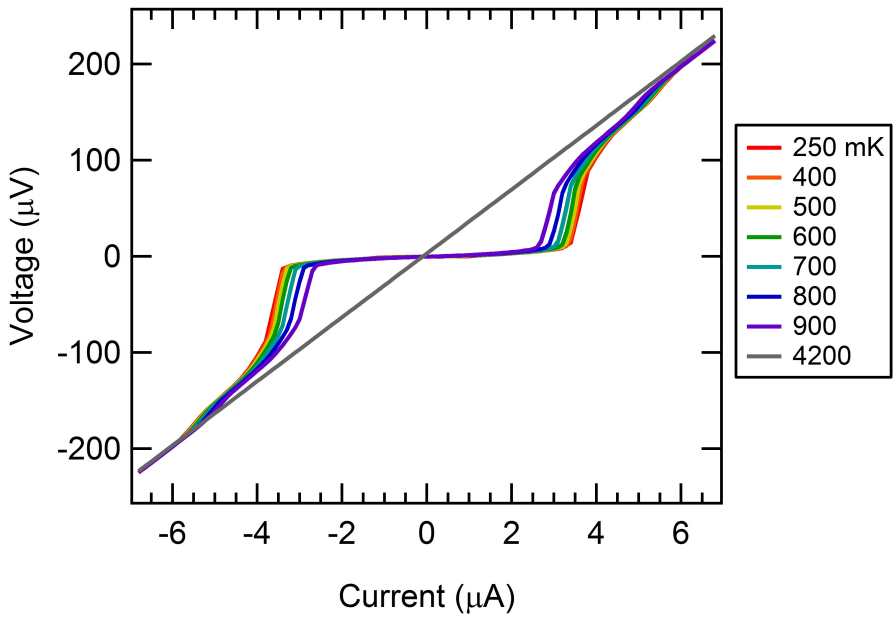

Figure 8.5: Voltage versus current curves measured on device shown in Fig. 8.3 at different temperatures. As the temperature increase the superconducting gap closes.

The curves also show that the size of the low resistance region gets smaller with increasing temperature. This means that the sample is transitioning from the superconducting regime to normal regime. There is some extra curvature to the V-I curves, located at approximately 5.5μA, indicating that the transition is more complex. In order to better understand the transitions that cause the curvature in the V-I curves, the curves are differentiated with respect to the current, and the results are presented in Fig. 8.6. The dV/dI curves, again similar to the R-T data, show that the sample exhibits more than one transition in the material. The peaks in graph represent transitions of part of the material from normal to superconducting, with the primary peaks being located at 5.5μA and 3.5μA. The peak at 3.5μA also has a shoulder with a slight plateau at 3.9μA that may be another peak that

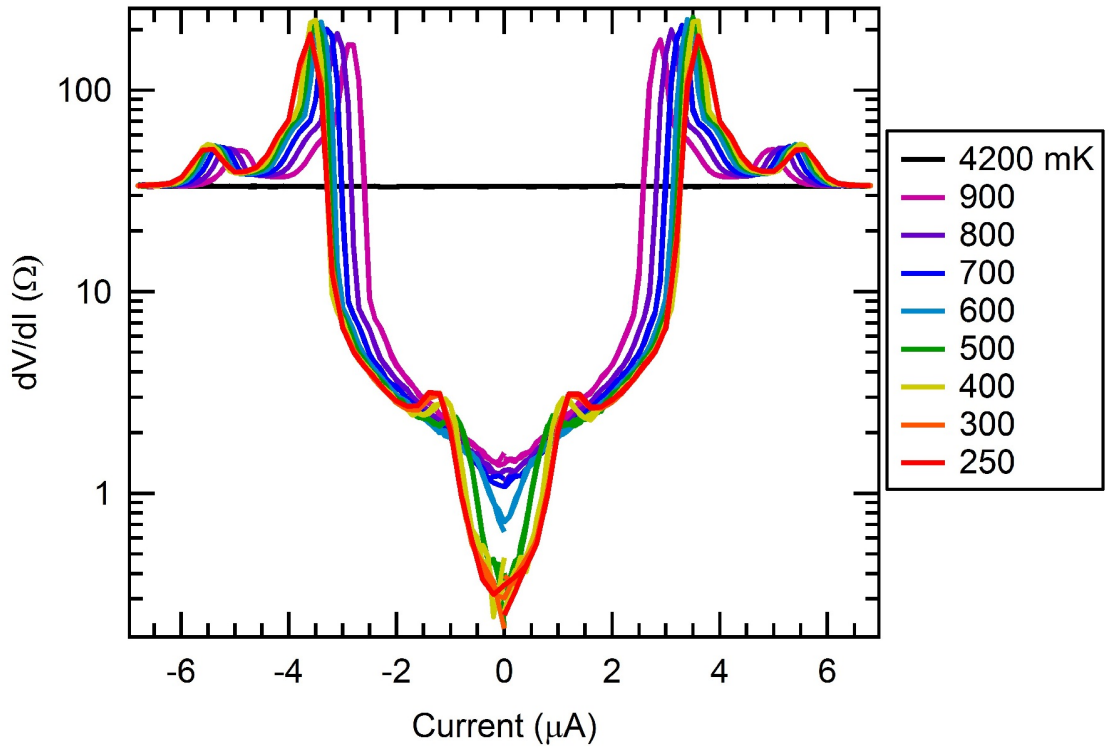

Figure 8.6: Differential resistance of the device shown in Fig. 8.3 at different temperatures, showing a trend of decreasing strength of superconductivity as temperature is increased. Three peaks are observed, two outside the superconducting gap at 5.5μA and 3.5μA and one inside the gap at 1.3μA. The peak at 3.5μA also has a shoulder at 3.9μA that may be hiding another peak next to it. It should be noted that the inner 1.3μA peak disappears more quickly with increasing temperature than the outer peaks.

is hidden by the primary peak. The primary superconducting gap spans from +3.5μA to -3.5μA. These multiple peaks again speak to the idea that the material is not evenly doped, though it is also possible that the resultant material is a multiband superconductor, similar to MgB_2 [67], which also shows a similar structure in the dV/dI curves.

There is also a notable secondary gap within the main gap, spanning from +1μA to -1μA, that disappears above 600mK. This gap is also surrounded by two peaks at temperatures below 600 mK. These peaks disappear quickly with temperature and move with the gap as the temperature increase.

To further understand the nature of the superconductivity, the changes in the dV/dI curves at different magnetic fields are displayed in Fig. 8.7. Many of the same features and changes from Fig. 8.6 are observed in this graph. The two primary peaks outside the gap are observed to be decreasing as a function of magnetic field, following the decreasing superconducting gap. At fields of 1.2T and 1.6T the shoulder of the 3.5μA peak primary peak has resolved into its own peak. In order to better visualize the changes in the peaks as a function of magnetic field, the dV/dI curves are plotted in an image map, Fig. 8.8. As seen in Fig. 8.7, the shoulder of the 3.5μA peak resolves into a separate peak beginning around 0.6T. This third peak is most pronounced at 1.4T. By 2.6T, all three outer peaks have melded into one. The inner peak has disappeared at lower fields around 1T.

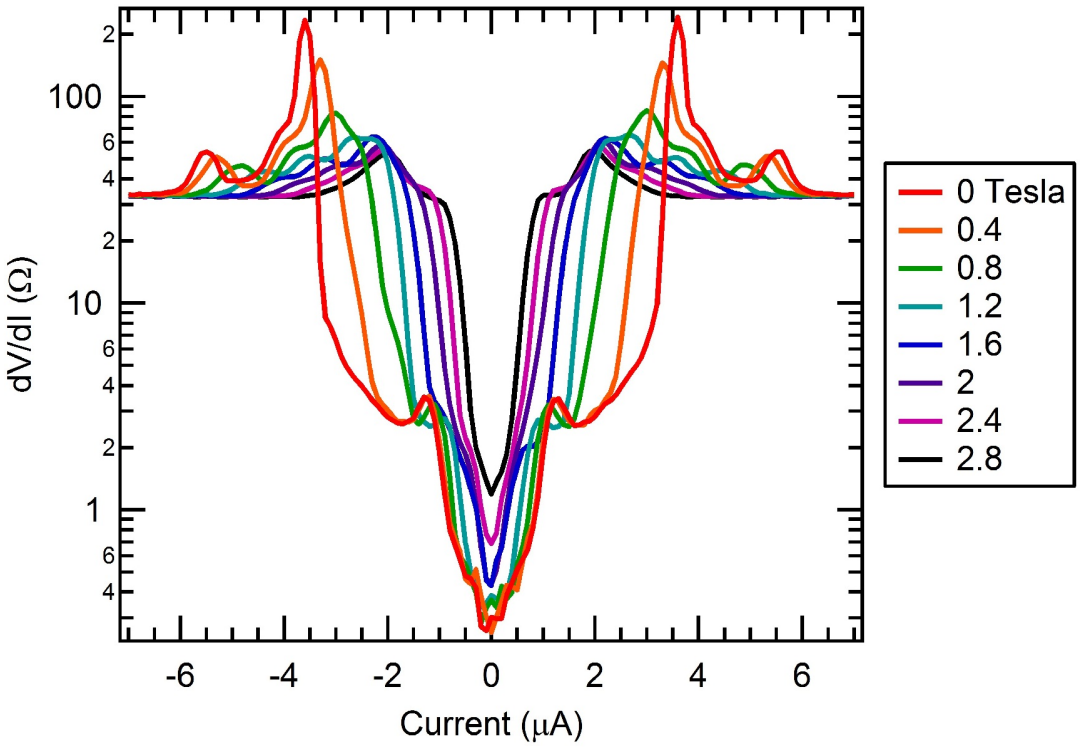

Figure 8.7: Differential resistance of the device shown in 8.3 at different applied magnetic fields, showing a trend of decreasing strength of superconductivity as applied magnetic field is increased. The same three peaks in 8.6 are observed, as well as an additional peak that is resolved from the shoulder of the 3.5μA peak at 1.2T and 1.6T.

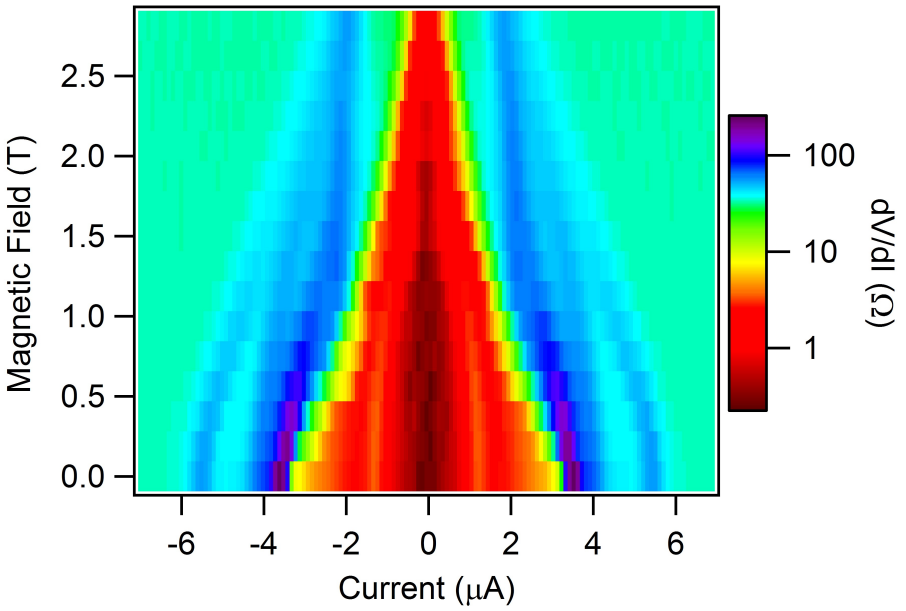

Figure 8.8: Image plot of the differential resistance of the device shown in Fig. 8.3 at different applied magnetic fields and data beyond that shown in Fig. 8.7 .

8.2.2 Materials Analysis

The transport measurements of the device shown in Fig.8.3 decisively show that the voltage pulse annealing produced a superconducting material, but it is important also to make sure that there is no inadvertent contamination. In order to check the device for contamination, EDS was performed on the device in an SEM. Both the VP-annealed region, as well as an un-annealed pristine region, were measured. The EDS results from the voltage pulse annealed region are shown in Fig.8.9, corresponding to the area between leads 4 and 3, as depicted in Fig.8.3. X-ray peaks are observed for the Bi and Se of the nanostructure, the Pd of the original leads, and the Pt from the leads added after annealing. The Si and O peaks are from the substrate. The only apparent contaminant was a small amount of carbon,

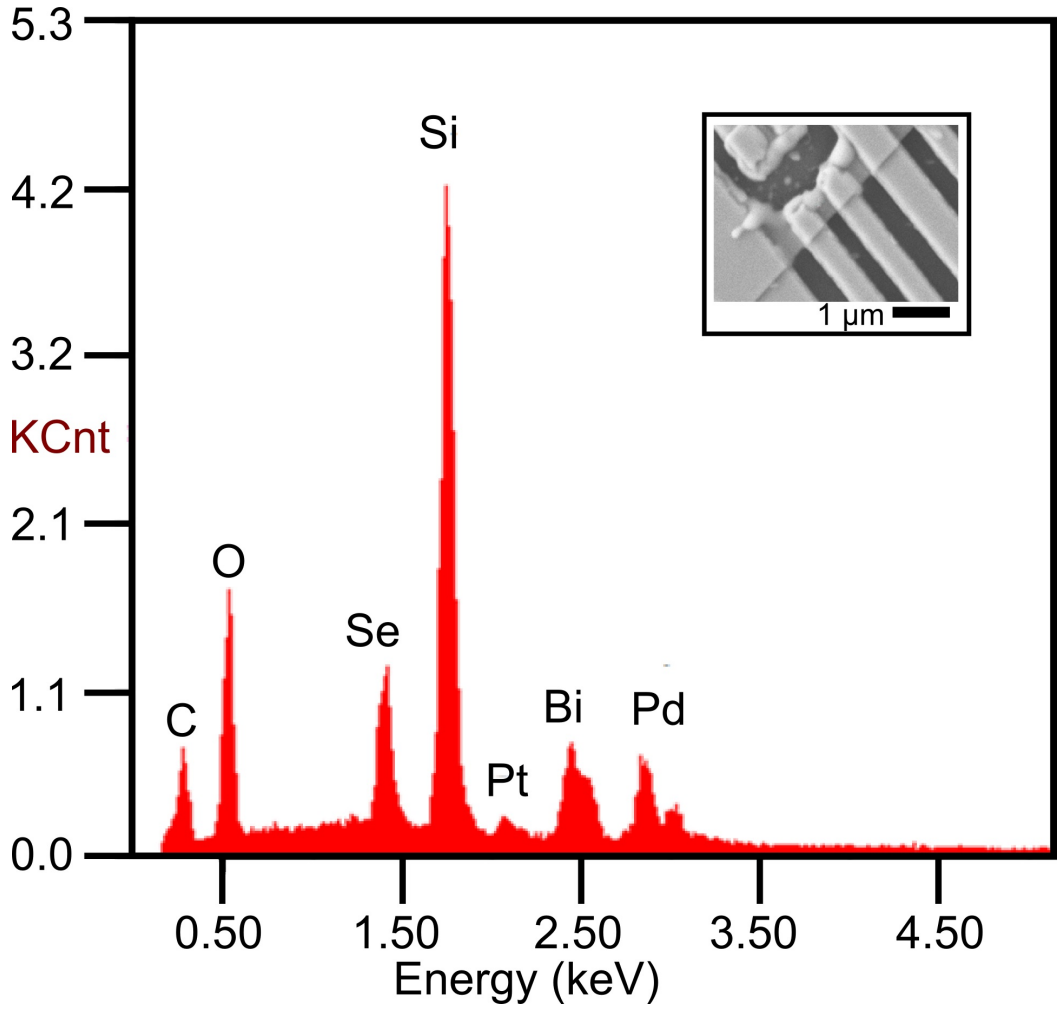

Figure 8.9: Energy dispersive x-ray spectroscopy data of transport measured portion of voltage pulse annealed sample shown in Fig. 8.3. Inset depicts the region(boxed in red) where the EDS measurement was obtained, and the transport measurements were performed.. EDS spectroscopy data from this region indicates only expected elements were present, i.e. Pd, Pt, Bi, Se, O, and Si. Carbon line is likely due to a small amount of contamination due to device handling and between measurements.

which most likely came from the sample being handled and cooled down and measured twice. This measurement shows that there was no significant contamination, and especially no known elemental superconductors could have a role in the transport measurements. The EDS results from the pristine region shown in Fig. 8.10, with the measured region shown boxed in red in the inset, also show no major contamination. There is, as with the VP annealed region, some small carbon contamination. These results, along with the materials analysis of the pristine region, and the transport measurements, show that the VP annealing has created superconductivity in a material made primarily of Bi, Se, and Pd. However, the VP annealing is a very uncontrolled and destructive process. In order to make a consistent and careful process, another annealing method must be used.

8.3 Pd Doping II: Thermal Annealing

With the information provided from both the thermal copper annealing, and the VP Pd doping, thermal annealing of Pd into Bi_2Se_3 shows promise as a method to induce superconductivity in Bi_2Se_3. In order to develop a thermal annealing method, a four step plan was used to prove the concept. First, a Bi_2Se_3 nanostructure device with palladium leads was covered completely in a thin palladium capping layer, and thermally annealed to see if there was a structural change to the sample when exposed to a large amount of palladium. Second, the capped device was measured at low temperatures to see if superconductivity could be observed. Third, if the palladium capping worked, devices with palladium leads,

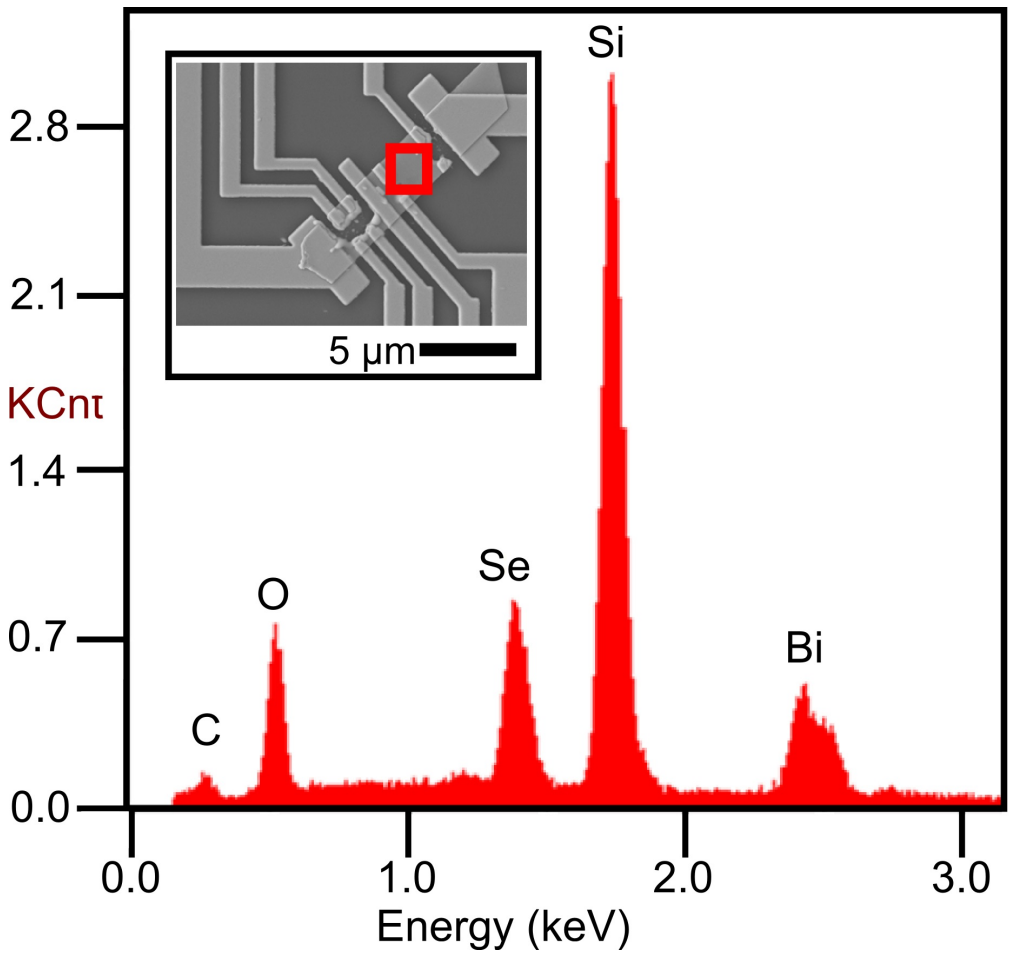

Figure 8.10: Energy dispersive x-ray spectroscopy data from part of sample shown in Fig.8.3 that was not voltage pulse annealed. Inset depicts the region (boxed in red) where the EDS measurement was obtained. EDS spectroscopy data reveal that the unannealed parts of the device remained pristine after annealing

and no capping layer, would be annealed to see if the same structural change occurred. Fourth, if the target doped devices did in fact change, they were measured at low temperatures. The section shows the results from these steps, separated first into the results from a palladium capped device and second from target annealed devices.

8.3.1 Palladium Capping

Images and R-T data from a palladium capped device are shown in Fig. 8.11. Fig. 8.11 (a) shows an optical image of the device before capping and annealing. Fig. 8.11 (b) shows the device after thermal annealing. The Pd capping layer was approximately 8nm thick and the Pd leads underneath the capping layer were approximately 90 nm thick. The tube furnace thermal annealing process was the same as that used in Sec.8.1, except an anneal temperature of 250°C was used. Before the annealing, the sample looks smooth and the leads are well defined. After annealing, the leads appear absorbed into the nanostructure, as the top of the leads is at the same height as the nanostructure. The surface of the nanostructure is now rough and bumpy, as opposed to a smooth nicely formed layer, indicating a structural change. There are also now gaps that exist between the leads and the nanostructure, indicating a separation by absorption.

The sample was cooled down in the Physical Property Measurement System(PPMS), and measured using a current biased two-probe measurement configuration. The data from the R-T measurement is shown in Fig. 8.11. The device exhibits a transition around 500mK that drops the resistance by one third of its initial value, but does not decrease it to zero.

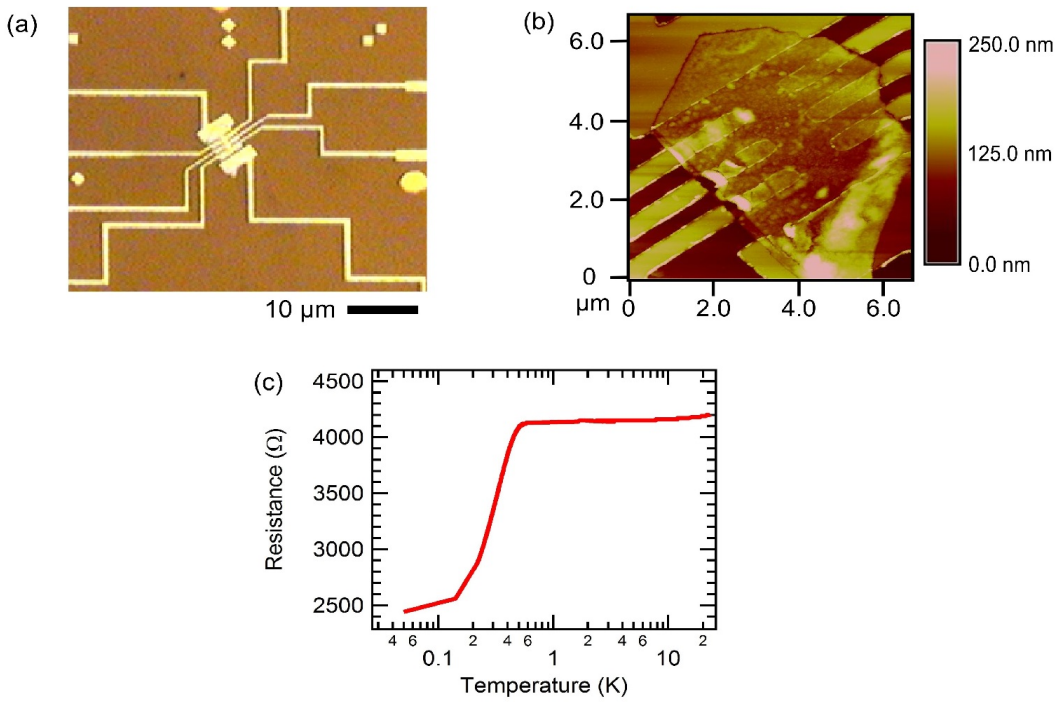

Figure 8.11: Images and two-probe resistance versus temperature of a thermally annealed palladium-capped Bi_2Se_3 device. (a) Optical image of capped device before annealing. (b) AFM image of device post annealing. In the AFM image the device no longer looks smooth and flat, but has a coarser top and there are now gaps between the leads and nanostructure itself. The Pd leads are shorter than as deposited, indicating some Pd absorption has occurred. (c) Resistance versus temperature curve showing sharp superconducting like drop in resistance beginning at 500 mK.

Some of the measured resistance is most likely resistance from the leads going down to the sample in the PPMS. The magnetoresistance of the sample at several temperatures is shown in Fig. 8.12. At 800mK, Fig. 8.12(a), the superconducting gap hasn't formed, but there is a dip that is indicative of WAL. There is a second dip above 1T that may be indicative of a second WAL region. The MR at 550mK is shown in Fig. 8.12(b), showing that the gap is beginning to form and the resistance around zero field is dropping. The drop in resistance around zero field increases with the decreasing temperature at 350 mK, as shown in Fig. 8.12(c). At 200 mK, the sample is in the stable region where the superconducting transition has saturated and the MR has reached its maximum, as shown in Fig. 8.12(d). The 200 mK measurement shows both the superconducting gap and the WAL dip, which is observed as the thin region at the bottom of the superconducting well. The WAL signal from the 800 mK and 200 mK data were fit with the Hikami-Larkin Nagaoka theory [2] laid out in Sec. 2.1.1 Eqn.2.8, and are displayed in Fig. 8.12(a) and (b) with red representing the data and blue representing the fit. For the 800mK data the HLN fit finds $\alpha = -0.045$ and coherence length $l_\phi = 90nm$. When the temperature has decreased to 200 mK the HLN fit finds $\alpha = -0.23$ and $l_\phi = 2.6\mu m$, putting the 200 mK data and the sample in the strong spin-orbit regime. In comparing the 800 and 200 mK data and fit parameters, there is an obvious increase in the coherence length and strength of the observed WAL. This is what would be expected when the sample gets colder, as the phonons and other effects will freeze out and quantum mechanical effects will become more pronounced. The fact that WAL is observable, along with the fact that the resistance does not go to zero, most likely means

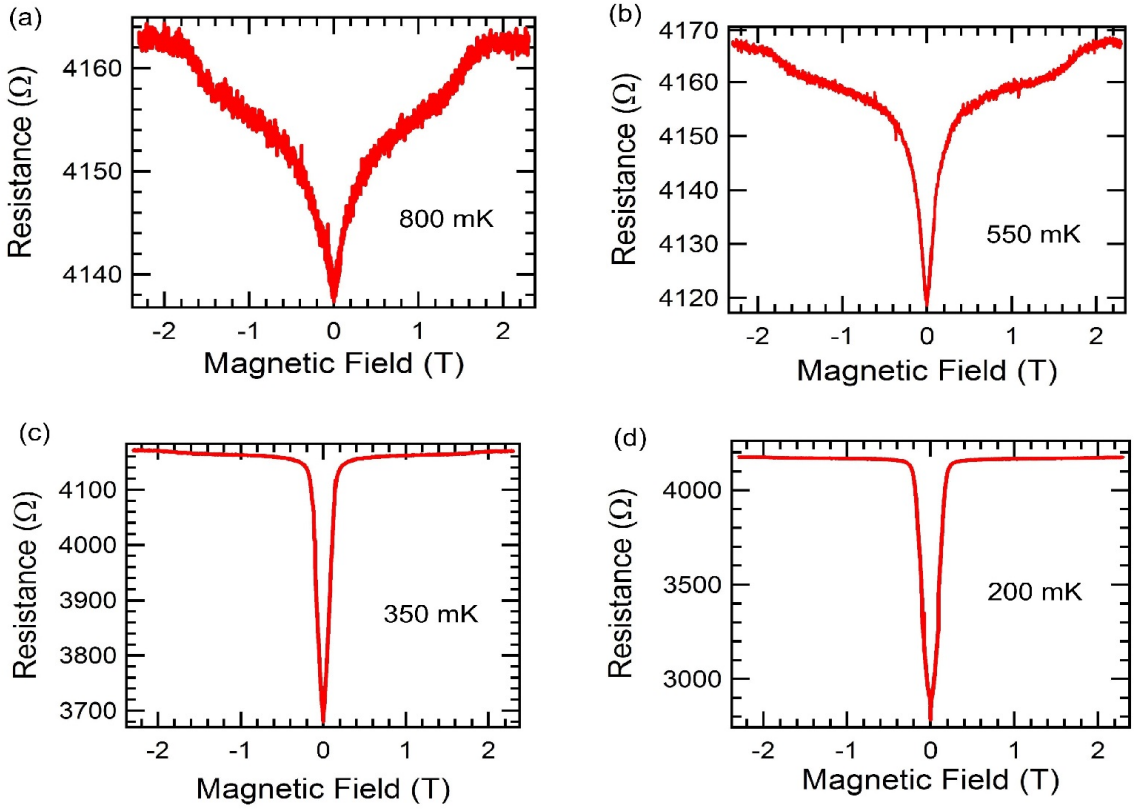

Figure 8.12: Two-probe magnetoresistance measurements of the nanodevice depicted in Fig.8.11(b) at different temperatures. (a) Magneto-resistance measurement of the device at 800mK. Dip in the resistance around zero field is indicative of weak antilocalization. (b) Magneto-resistance measurement of the device at 550mK, showing that the dip is increasing in depth. (c) Magneto-resistance measurement of the device at 350mK. Dip in the resistance has increased significantly and is showing not only WAL, but also the onset of superconductivity, which is accelerating the increase in depth. (d) Magneto-resistance measurement of device at 200 mK. Weak antilocalization is still observed around zero field, as well as a sharp increase in resistance with applied magnetic field.

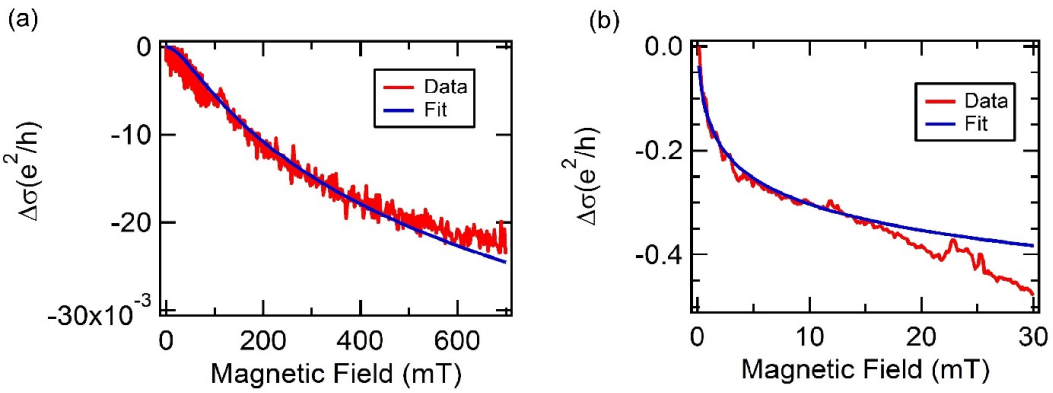

Figure 8.13: Magnetoconductance measurements of weak antilocalization at 800mK and 200mK and fits using the Hikami-Larking-Nagaoka model [2]. (a) Magnetoconductance and HLN fit for 800 mK data. The HLN theory finds the fit parameters to be $\alpha = -0.045$ and coherence length $l_\phi = 90nm$. (b) Magnetoconductance and HLN fit for 200 mK data. When the temperature has decreased to 200 mK there is still evidence of WAL at low field as shown in (a), but it now sits in a deep resistance valley. The HLN fit is again used to fit the WAL signal obtaining $\alpha = -0.23$ and $l_\phi = 2.6\mu m$. In comparing the 800 and 200 mK data and fit parameters, there is an obvious increase in the coherence length and strength of the observed WAL as the temperature has increased.

that there are non-superconducting regions in the sample.

8.3.2 Targeted Annealing

With the promising results from the Pd capped sample, target annealed samples were produced to reproduce both the physical transformation and superconductivity. In order to speed up sample production, samples in this subsection were produced from mechanically exfoliated samples as opposed to the catalyst-free grown samples in the previous sections. This section will first describe the physical changes that the devices undergo in the annealing, and then data from a target-doped sample. The samples used for target doping were made using Ti/Au optical leads and Pd leads on 300nm thick SiO on silicon substrates.

8.3.2.1 Materials Comparison

The materials analysis of the target doped samples focuses on imaging of the devices before and after annealing. Fig. 8.14(a) and (b) show a Bi_2Se_3 nanostructure with a Pd lead before and after annealing, respectively. The before image shows a smooth 60nm tall nanostructure with Pd leads that are 90 nm thick. In the bottom left corner, there is a 5nm thick Pd patch sitting isolated on the susbtrate surface, and there is a similar thin patch on top of the substrate sitting on the left side of the center lead. Some Bi_2Se_3, circled in red, is isolated from the leads, and like the patch, serve as a control. After initial AFM imaging, the sample was annealed using the same procedure described in Sec.8.1, except an anneal temperature of 280°C was used. The sample was immediately AFM imaged

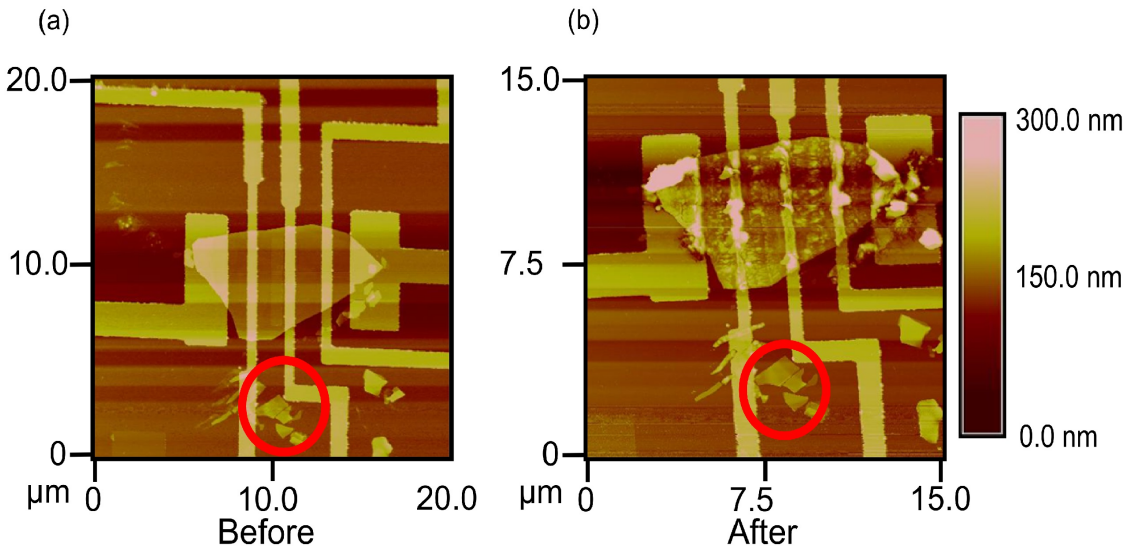

Figure 8.14: Images of anneal-doped Bi_2Se_3 nanodevice. (a) AFM image of mechanically exfoliated Bi_2Se_3 with palladium leads before annealing. (b) AFM of sample in previous (a) after annealing under flowing Ar gas at 280C for one hour. At any point where Pd is touching Bi_2Se_3 the surface morphology changes post annealing, free Bi_2Se_3 and Pd do not change during the annealing process.

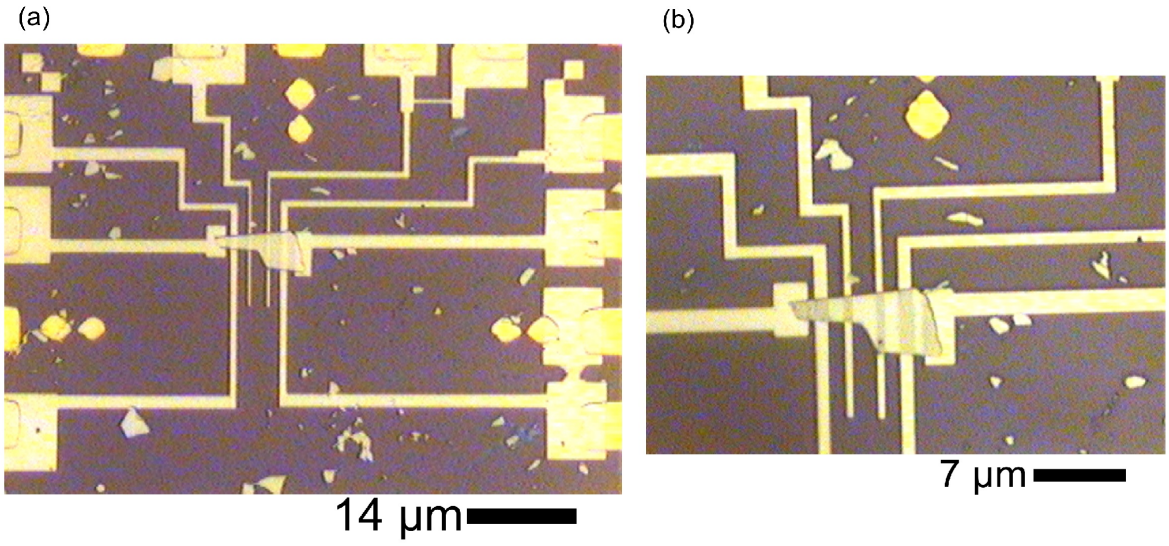

Figure 8.15: Images of anneal doped Bi_2Se_3 nanodevice. (a) Optical image of Mechanically exfoliated Bi_2Se_3 with palladium leads before annealing. (b) Optical image of sample in (a) after annealing under flowing Ar gas at 220 °C for one hour. There is an optical change between the two images as the leads, from before to after, have changed from well defined rectangles sitting on the nanostructure into absorbed gray regions. As in Fig.8.14, free Pd is the same after annealing. Different from Fig.8.14 is that due to the lower annealing temperature, the Bi_2Se_3 has not completely absorbed Pd and there are some pristine regions remaining.

again after annealing, as shown in Fig. 8.14(b). Like the Pd capped sample in 8.11(b), the surface morphology of the nanostructure has been greatly altered and is much rougher than before. Parts of the leads appear absorbed into the material, and gaps can be seen between some of the leads and the nanostructure. These changes occurred only where Pd was touching Bi_2Se_3. The free nanostructures, circled in red, remained unchanged throughout the annealing process, as did the Pd leads and thin Pd patch that were not in close proximity to a Bi_2Se_3 nanostructure. Optical images of another sample, before and after annealing at 220 °C using the same process, is shown in Fig.8.15(a) and (b). Before

annealing, the sample looks smooth and ordered with the leads sitting obviously on top of the nanostructure. After annealing, the leads are no longer well defined, and instead appear as gray patches on the nanostructure and seem to be absorbed into the nanostructure, as there are no well defined leads on top. It is obvious some of the doping has gone between some leads, as between the two leads on right, which have themselves been absorbed, and the region between them, is also grayed. Other regions between the leads seem unaffected by the annealing. This temperature and method has allowed for a very controlled absorption of the Pd into the Bi_2Se_3.

8.3.2.2 Transport Characteristics

The data in this subsection were taken in the PPMS using the four-probe method for every measurement. The device shown in Fig.8.15 is shown again in Fig.8.16, highlighting the regions of the sample that were measured. Not shown in these images is that after annealing, and before measurement, a second layer of Pd leads was added to patch up any leads that were disconnected due to absorption.

The sample always had current sourced from lead 1 to lead 6. The red box measures across the majority of the sample, between leads 2 and 5. The green box is referred to as *Region 1* and the voltage is measured from 2 to 3. The blue box is denoted *Region 2* and the voltage was measured across leads 3 and 4. Finally the purple box is referred to as *Region 3* and the voltage was measured across leads 4 and 5.

The R-T curve measuring *Region 1* is displayed in Fig.8.17. A transition in the region is

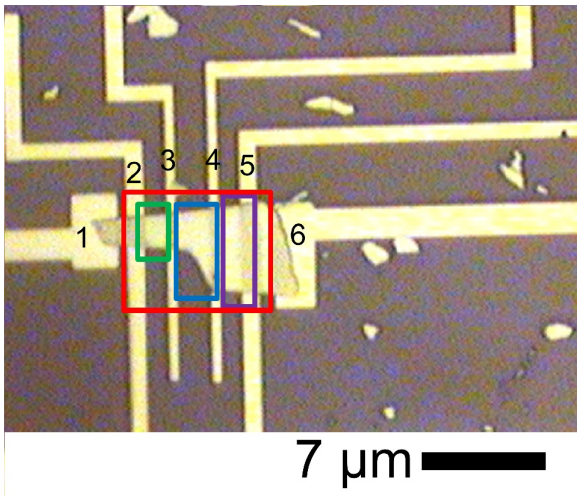

Figure 8.16: Optical image of nanodevice with boxes that delineate different regions that were measured using different combinations of leads. Green is *Region 1*, blue is *Region 2*, and purple is *Region 3*. The red box denotes the largest portion of the device that can be measured using a four-probe measurement.

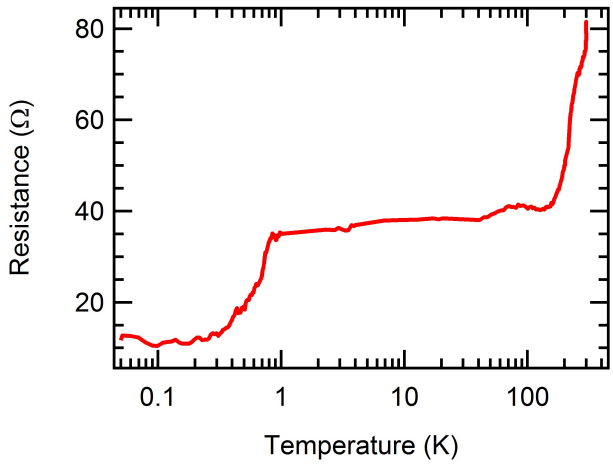

Figure 8.17: Resistance versus temperature of the green region, Region 1, as outlined in Fig.8.16. The R-T curve shows that this region of the device has a transition temperature of 800 mK. This region does not go fully superconducting, indicating that part of the material is still normal and the Pd has not been fully absorbed.

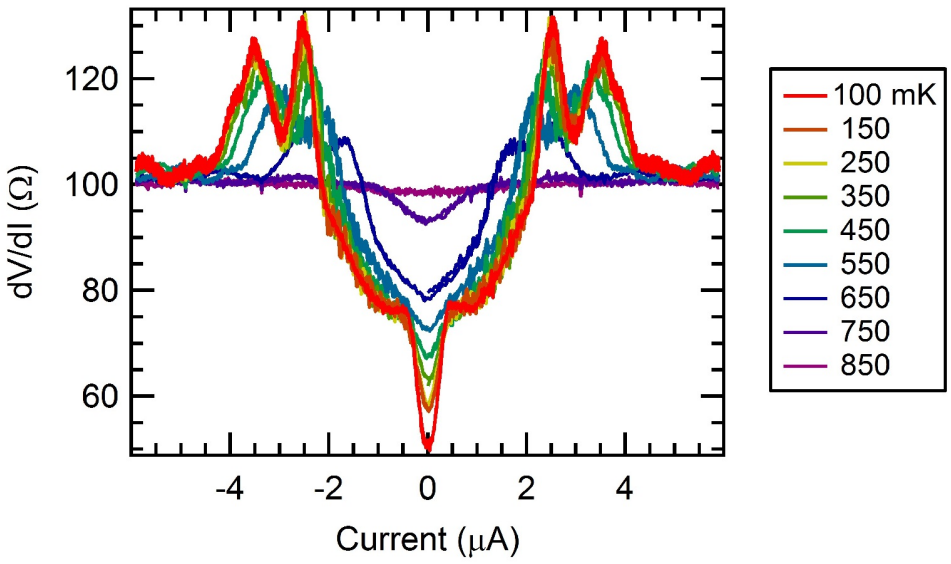

Figure 8.18: Differential resistance measurements of the whole device, red boxed region shown in 8.16, at different temperatures. Two primary peaks are observed outside the main gap at 2.5 μA and 3.5 μA. As the temperature is increased, the superconducting gap closes.

observed to occur at 800 mK. As with previous devices, this region does not go completely superconducting, and the resistance plateaus at approxiamtely 12Ω. As mentioned in the materials analysis, this region optically appeared with an undoped area between the leads. The superconductivity is most likely coming from the absorbed regions where the leads were, and from the proximity effect. In order to look more in depth at the superconductivity, the dV/dI measured over *All Regions*, red box in Fig. 8.16, at different temperatures is plotted in Fig.8.18. As observed in the VP sample, there are multiple superconducting peaks, as well as a small gap within the primary gap. The two main peaks outside the main gap are located at 2.5 μA and 3.5 μA, this is much closer to zero than in the VP sample. Also, unlike the VP sample there are no noticeable subgap peaks.

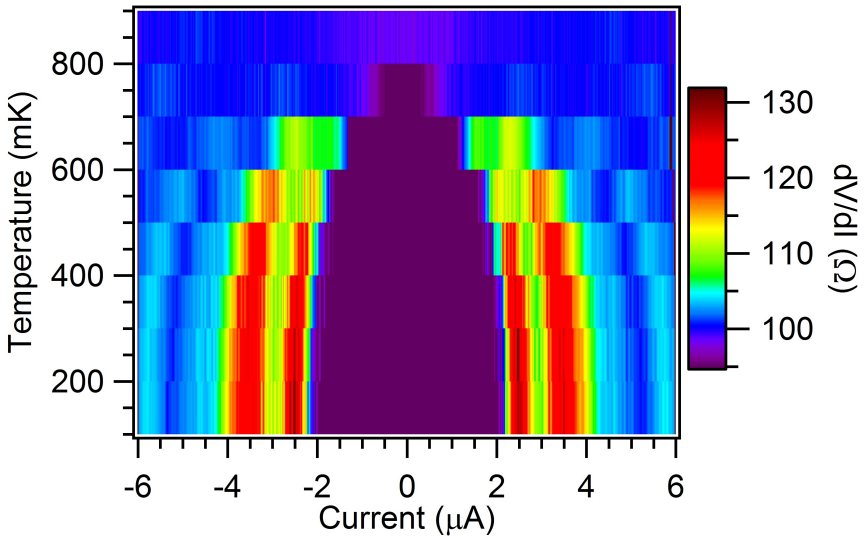

Figure 8.19: Differential resistance measurements of the whole device, red boxed region shown in 8.16, at different temperatures displayed as an image map. Two primary peaks are observed outside the main gap at 2.5 μA and 3.5 μA. As the temperature is increased a third peak moves towards the center in from the sides.

In order to better view the trend of the peaks as a function of temperature, a heat map was produced and is displayed in Fig. 8.19. In order to properly visualize the peaks outside the gap, the resistance is scaled to ignore all data below 95Ω. The two primary peaks outside the gap are observed to meld together into a single peak above 550 mK. There is also a faint third peak on the very edge of dV/dI curves that slowly moves towards zero as the temperature increases, before disappearing above 750 mK. The dV/dI at different magnetic fields is shown in Fig. 8.20. The center small gap closes below 400 Oe, while the main gap exists until above 2300 Oe. The same two primary peaks are observed to disappear as a function of magnetic field. The heights of the peaks decrease quickly with magnetic field, decreasing by more than 50-percent before the field reaches 200 Oe. A

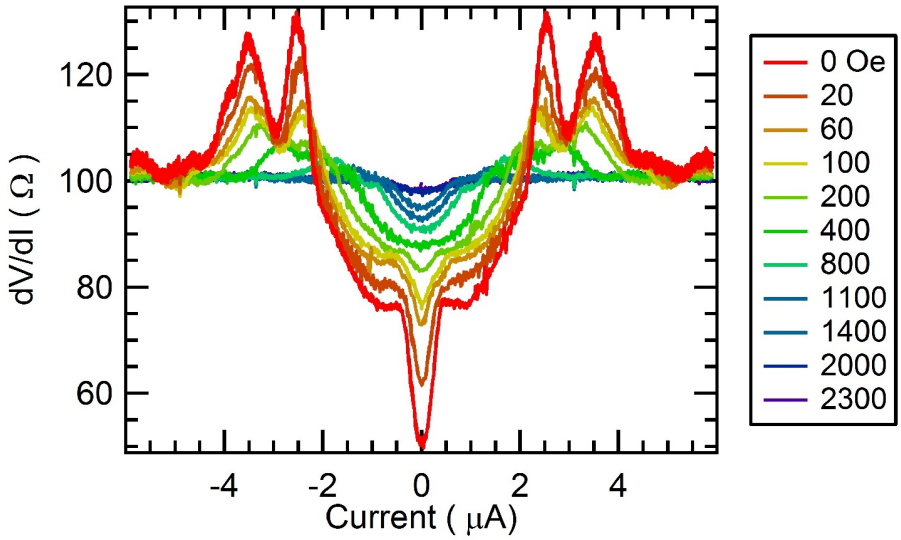

Figure 8.20: Differential resistance measurements of the whole device, red boxed region, shown in 8.16 at different magnetic fields. Two primary peaks are observed outside the main at 2.5 μA and 3.5 μA. As the magnetic field is increased, the superconducting gap slowly closes.

feature that also exists in Fig.8.18 is the shoulder on the peak located at 3.5 μA. This feature may in be another obscured peak as was observed in the VP sample in Fig.8.8.

Overall, although the peak locations and gap width are not the same as in the VP annealed sample, superconductivity with multi-peak structure and a central small gap is still observed. The basic measurements of the sample have shown that many characteristics of a VP annealed sample can be reproduced with the alternative thermal annealing method. However, with the thermal annealed sample the different regions may be acting differently, as described in the next subsection.

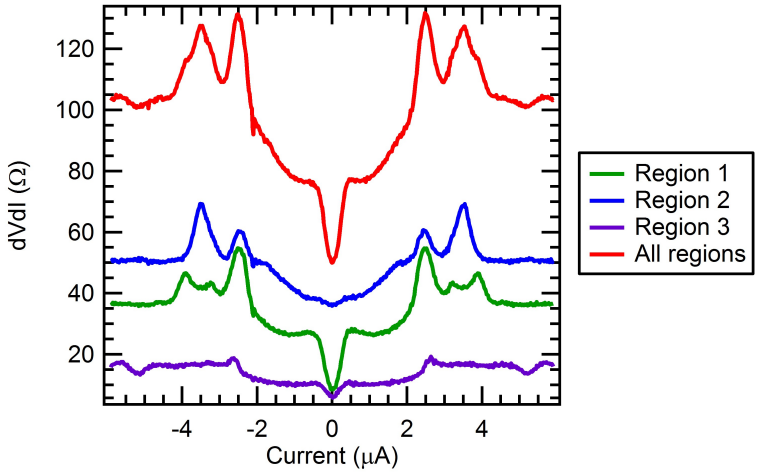

Figure 8.21: Differential resistance measurements of four regions depicted and color-coded similarly in 8.16. Each region shows different peaks and the strength of superconductivity is different. *Region 1* shows the largest sub-gap peak and has three peaks outside the superconducting gap.

8.3.2.3 dV/dI Characteristics By Region

The measurements in the previous subsection, except for the R-T curve, were all performed measuring the voltage across the whole device, potentially obscuring distinct phenomena in each doped region. In order to better understand the doping effects in the different regions, dV/dI curves for each region, and the whole device, are presented in Fig.8.21. The traces in Fig.8.21 are colored to match the established color coding of the regions from Fig.8.16. The data from the three regions are vastly different, but all correctly add together to re-form the trace taken for the whole device. *Region 1* shows the deepest small gap and shows three peaks outside the gap at 2.6 μA, 3.2 μA, and 3.7 μA. The *Region 1* data show that there are in fact peaks hidden in the 3.5 μA peak in the *All regions* data. *Region 2* shows the shallowest small gap and shows only two peaks outside the primary gap at 2.6

μA and 3.4 μA. The faint far peak, established by the image map in Fig. 8.19, is observed only in *Region 3*. The third region also has the 2.6 μA peak, but no other peaks exhibited by the other two regions.

The large variety in dV/dI structure, both in feature location and strength, shows that each region is very different. Each region is of a different size and shape, but there is no particular trend that the data follow in regards to this. Part of the differences between regions is most likely due to different amounts of doping.

8.3.2.4 Magnetoresistance Measurements

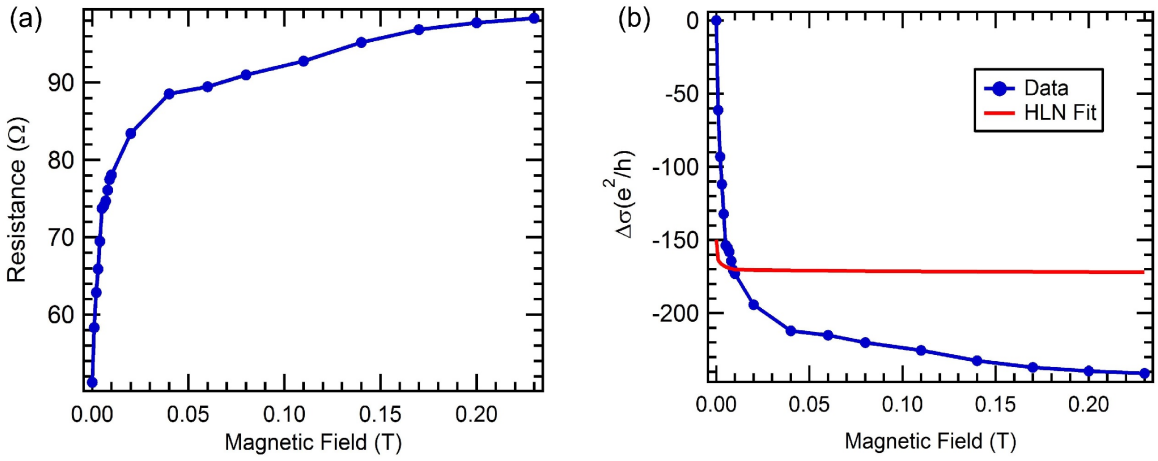

Figure 8.22: Magnetoresistance, magnetoconductance and WAL fit of data taken on the whole device boxed in red in 8.16. (a) Magnetoresistance shows a sharp increase in resitance with minimal applied field. (b) Converting the mangetoresistance to magnetoconductance(blue) and fitting with the HLN fit(red) shows that the sharp change with minimal applied magnetic field is not due to just WAL.

The dV/dI curves measured across the whole device displayed in Fig. 8.20 can be used to create a magnetoresistance curve by selecting the data at 60 nA from each curve, as shown in Fig. 8.22(a). The superconductivity disappears quickly with applied magnetic field. As observed in the dV/dI, 0.04 T is where the small gap has disappeared. The sharpness of the dip in the magnetoresistance initially seem like a WAL signal, but when converted to conductance the results cannot be fit with HLN theory, as shown in Fig. 8.22(b). One possibility for the sharpness of the magnetoresistance with a small amount of applied field is that the majority of the sample is a normal material that is induced into superconductivity by proximity effect. If the leads are close enough and proximity effect strong enough, then Region 1 of the device may be similar to the Josephson junction device devised by Ilan et. al. [25] and mentioned in the Majorana section. The device suggested would potentially

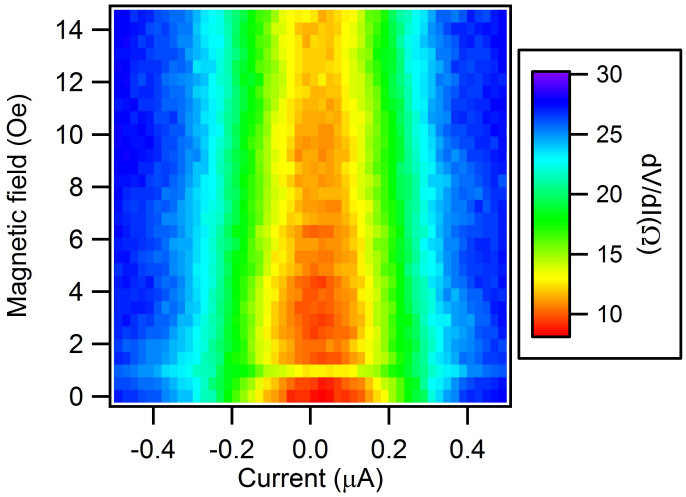

Figure 8.23: Differential resistance as a function of magnetic field and current measurement of Region 1, green boxed region displayed in 8.16. No obvious oscillations in the critical current are observed.

present perfect transmission, which would be observable in the fraunhoffer pattern if the device is in fact a Josephson junction. Fig. 8.23 shows a low field measurement of Region 1, based on the size of the region one flux quantum should be present in the area of the device at a field of 5Oe, which would then be the period of oscillation in the Fraunhoffer pattern. In the plot no obvious oscillations are observed meaning that the leads are not close enough together to form into a Josephson junction.

Overall, the measurements and methods in this chapter provide a new approach for inducing superconductivity in bismuth selenide. The thermal annealing method shows particular promise for creating customized devices in the nanostructures themselves, eliminating the need for an interface with another material. The next step is to better understand the nature of induced superconductivity and to make devices that are specifically focused on

the observation of Majorana fermions.

Chapter 9

Conclusions

This dissertation has focused on Bi_2Se_3 nanodevices from theoretical conception of their topological properties to measurement of the exotic properties of doped devices designed to work towards quantum computing. The devices were fabricated using standard optical and e-beam lithographies and measured using Helium-3 and dilution refrigerators in order to probe the material properties in the quantum regime. The three overarching projects described were to develop a novel growth method to obtain high quality nanostructures, to measure the electrical properties of these nanostructures, and finally to induce superconductivity in these devices towards the goal of observing Majorana fermions.

The growth of nanostructures was performed using a modified version of a Vapor-Liquid-Solid CVD method. The main modification was to add H_2 as a carrier gas during the growth. This allowed the growth to be performed without using a catalyst and to be performed on several different substrate types. The resultant nanostructures proved to be

of good size for fabricating nanodevices and included a variety of geometries including nanowires, ribbons, and flakes. Using a variety of materials analysis techniques, including EDX and electron diffraction, it was shown that high-quality nanostructures of the appropriate chemical make-up and crystal structure were produced.

With clean nanostructures that could be fabricated as-grown into nanodevices on silicon, the next step was to measure their electrical properties at low temperatures. At the temperature of liquid Helium and below, the nanostructures were shown to still have definite bulk conduction as evidenced by their low resistivity. The structures did however show a resistance peak as a function of a gate voltage, typically associated with the Dirac cone that characterizes the topological surface states. Due to the high measurement temperature at 4.2K, the devices did not exhibit the strong-spin-orbit coupling effect of WAL. More evidence of the topological states was observed by converting the Hall resistance to conductance. The conductance was fit to a two-carrier conduction model, showing that there were multiple conduction channels in the sample, with carrier concentrations similar to that in MBE-grown thin films which showed a surface state as well as an underlying 2DEG.

In order to probe more exotic phenomena, the nanostructures were doped to induce superconductivity. Beginning with a bulk Bi_2Se_3 pre-doped with copper, a known combination that is superconducting, annealing methods were developed in order to add palladium to Bi_2Se_3 to create superconductivity. The superconductivity in the initial $Cu_0.12Bi_2Se_3$ devices was repaired using thermal annealing after it had been destroyed by the copper leaching out of the sample. These results lead to attempts to add Pd to Bi_2Se_3 to make a

controllably dopable device. Using voltage-pulse annealing and thermal annealing of palladium into Bi_2Se_3 was achieved and superconductivity was observed. The best and most controllable process was the thermal annealing which allowed for making devices which had superconducting islands separated by normal Bi_2Se_3 regions. All Pd-doped devices showed unusual transport features. Specifically, there were multiple peaks in the dV/dI curves, suggesting that there were regions with different superconducting properties which could come from multiple gaps in a standard material or areas with different dopings. The real power of the controlled doping provided by thermal annealing is that custom devices can be doped into the nanostructure itself. One such device would be the Majorana devices that require a Josephson junction design.

The potential for creating custom Majorana devices leads into the future work that can sprout form this dissertation. In the thermally annealed samples, there are three main questions to be answered. The first question concerns the crystal structure of the superconducting regions. This can be understood both by further measurement of devices as well as more detailed materials analysis. Also, by calculating the amount of Pd that is absorbed into the Bi_2Se_3 it may be possible to separately produce bulk samples of candidate materials. The second question is whether the controlled doping can in fact be used to create Majorana devices. The devices shown in Chapter 8 were larger and wider than the nanowire systems designed by theorists and predicted to host Majoranas. Future devices should have a smaller profile with doped regions that are physically closer and thermal anneal doping should be attempted with nanowire samples. The third question that needs to be answered

is whether other elements can be doped into Bi_2Se_3 in the same manner as the Pd and Cu. It may be possible to perform the same operation with iron or nickel to get ferromagnetic regions or perhaps make other superconducting materials or more exotic phenomena.

Appendix A

Fabrication recipes

A.1 Optical fabrication recipe

-Start after nanostructures are on substrate. -Set sample in Acetone for 5 min the IPA for 5 min(do not sonicate in either) then e-beam hot plate for 2 min. -In spin coater add 3 drops of SU1813 to top of substrate. -Spin at 4000 RPM for 45 sec. -Bake at 115 ∘C for 60 sec. -Use Janice/Atikur ”50X thin w/ markers” and ”10X 20 lead” masks -Turn up microscope to about 9.5(i.e. 10 should be on but the light should be dimmer than the rest) -Do all 50X on a chip, exposing for 32 secs each -Develop sample for 10 sec in Microposit 351(1:7 351:Water, I use 2mL:14mL) -Wash off excess Microposit 351 in water for 60 sec. -Do 10X all at once on a chip, exposing for 4 min and 30 sec each. -Develop for 60 seconds in Microposit 351 and wash in water for 60 sec. -If pattern does not appear try developing for an extra 30 sec. If this does not work, start over.

A.2 E-beam fabrication recipe

-Same starting clean with Acetone and IPA cycle as Optical recipe -Add three drops of PMMA A4 950K. -Spin coat at 3000 rpm for 45 sec. -Bake for 90 sec on e-beam hot plate, 185 $\circ$. -Standard e-beam dose is 350 μC/cm^2 -Develop in MIBK:IPA ratio of 1:3 (keep in mind mother solution is already 1:1) for 45 sec. -Wash in IPA for 30 sec. -If pattern does not come out properly, or if there are contact issues with the device, consider using larger dose.

Bibliography

[1] Chao-Xing Liu, Xiao-Liang Qi, HaiJun Zhang, Xi Dai, Zhong Fang, and Shou-Cheng Zhang. Model hamiltonian for topological insulators. *Phys. Rev. B*, 82:045122, Jul 2010.

[2] Shinobu Hikami, Anatoly I. Larkin, and Yosuke Nagaoka. Spin-orbit interaction and magnetoresistance in the two dimensional random system. *Progress of Theoretical Physics*, 63(2):707–710, 1980.

[3] C. L. Kane and E. J. Mele. Quantum spin hall effect in graphene. *Phys. Rev. Lett.*, 95:226801, Nov 2005.

[4] C. L. Kane and E. J. Mele. Z_2 topological order and the quantum spin hall effect. *Phys. Rev. Lett.*, 95:146802, Sep 2005.

[5] Liang Fu, C. L. Kane, and E. J. Mele. Topological insulators in three dimensions. *Phys. Rev. Lett.*, 98:106803, Mar 2007.

[6] Rahul Roy. Topological phases and the quantum spin hall effect in three dimensions. *Phys. Rev. B*, 79:195322, May 2009.

[7] J. E. Moore and L. Balents. Topological invariants of time-reversal-invariant band structures. *Phys. Rev. B*, 75:121306, Mar 2007.

[8] D Hsieh, D. Qian, L. Wray, Y. Xia, Y. S. Hor, R. J. Cava, and M. Z. Hasan. A tunable topological insulator in a quantum spin hall phase. *Nature*, 452:970–974, Apr 2008.

[9] D Hsieh, Y. Xia, D. Qian, L. Wray, J. H. Dil, F. Meier, J. Osterwalder, L. Patthey, J. G. Checkelsky, N. P. Ong, A. V. Federov, H. Lin, A. Bansil, D. Grauer, Y. S. Hor, R. J. Cava, and M. Z. Hasan. A tunable topological insulator in the spin helical dirac transport regime. *Nature*, 460:1101–1105, Aug 2009.

[10] O. V. Yazyev, J. E. Moore, and S. G. Louie. Spin polarization and transport of surface states in the topological insulators $\mathrm{bi_2se_3}$ and $\mathrm{bi_2te_3}$ from first principles. *Phys. Rev. Lett.*, 105:266806, Dec 2010.

[11] Y. S. Hor, A. Richardella, P. Roushan, Y. Xia, J. G. Checkelsky, A. Yazdani, M. Z. Hasan, N. P. Ong, and R. J. Cava. p-type $\mathrm{bi_2se_3}$ for topological insulator and low-temperature thermoelectric applications. *Phys. Rev. B*, 79:195208, May 2009.

[12] S. R. Park, W. S. Jung, Chul Kim, D. J. Song, C. Kim, S. Kimura, K. D. Lee, and N. Hur. Quasiparticle scattering and the protected nature of the topological states in a parent topological insulator $\mathrm{bi_2se_3}$. *Phys. Rev. B*, 81:041405, Jan 2010.

[13] D. Hsieh, Y. Xia, D. Qian, L. Wray, F. Meier, J. H. Dil, J. Osterwalder, L. Patthey, A. V. Fedorov, H. Lin, A. Bansil, D. Grauer, Y. S. Hor, R. J. Cava, and M. Z. Hasan. Observation of time-reversal-protected single-dirac-cone topological-insulator states in $\mathrm{bi_2te_3}$ and $\mathrm{sb_2te_3}$. *Phys. Rev. Lett.*, 103:146401, Sep 2009.

[14] Y. Xia, D. Qian, D. Hsieh, L. Wray, A. Pal, H. Lin, A. Bansil, D. Grauer, Y. S. Hor, R. J. Cava, and M. Z. Hasan. Observation of a large-gap topological-insulator class with a single dirac cone on the surface. *Nature Physics*, 5:398–402, May 2009.

[15] Y. L. Chen, J. G. Analytis, J.-H. Chu, Z. K. Liu, S.-K. Mo, X. L. Qi, H. J. Zhang, D. H. Lu, X. Dai, Z. Fang, S. C. Zhang, I. R. Fisher, Z. Hussain, and Z.-X. Shen. Experimental realization of a three-dimensional topological insulator, bi2te3. *Science*, 325(5937):178–181, 2009.

[16] L. Fu and C. L. Kane. Superconducting proximity effect and majorana fermions at the surface of a topological insulator. *Phys. Rev. Lett.*, 100:096407, Mar 2008.

[17] A. R. Akhmerov, Johan Nilsson, and C. W. J. Beenakker. Electrically detected interferometry of majorana fermions in a topological insulator. *Phys. Rev. Lett.*, 102:216404, May 2009.

[18] X.-L. Qi and S.-C. Zhang. Topological insulators and superconductors. *Rev. Mod. Phys.*, 83:1057–1110, Oct 2011.

[19] S. Vishveshwara. Topological qubits: a bit of both. *Nature Physics*, 7:450–451, June 2011.

[20] T. H. Hsieh and L. Fu. Majorana fermions and exotic surface andreev bound states in topological superconductors: Application to $\mathrm{cu}_x\mathrm{bi}_2\mathrm{se}_3$. *Phys. Rev. Lett.*, 108:107005, Mar 2012.

[21] M Leijnse and K Flensberg. Introduction to topological superconductivity and majorana fermions. *Semiconductor Science and Technology*, 27(12):124003, 2012.

[22] C. W. J. Beenakker. Search for Majorana Fermions in Superconductors. In Langer, JS, editor, *ANNUAL REVIEW OF CONDENSED MATTER PHYSICS, VOL 4*, volume 4 of *Annual Review of Condensed Matter Physics*, pages 113–136. 2013.

[23] M. Z. Hasan and C. L. Kane. *Colloquium* : Topological insulators. *Rev. Mod. Phys.*, 82:3045–3067, Nov 2010.

[24] J. E. Moore. The birth of topological insulators. *Nature*, 8464:194–198, Mar 2010.

[25] Roni Ilan, Jens H Bardarson, H-S Sim, and Joel E Moore. Detecting perfect transmission in josephson junctions on the surface of three dimensional topological insulators. *New Journal of Physics*, 16(5):053007, 2014.

[26] L Jiang, C. L. Kane, and J. Preskill. Interface between topological and superconducting qubits. *Phys. Rev. Lett.*, 106:130504, Mar 2011.

[27] D. J. Griffiths. Introduction to quantum mechanics second edition. Pearson Prentice Hall, 2005.

[28] S. Matsuo, T. Koyama, K. Shimamura, T. Arakawa, Y. Nishihara, D. Chiba, K. Kobayashi, T. Ono, C.-Z. Chang, K. He, X.-C. Ma, and Q.-K. Xue. Weak antilocalization and conductance fluctuation in a submicrometer-sized wire of epitaxial bi_2se_3. *Phys. Rev. B*, 85:075440, Feb 2012.

[29] H Zhang, C.X. Liu, X.L. Qi, X Dai, Z Fang, and S.C. Zhang. Topological insulators in bi2se3, bi2te3 and sb2te3 with a single dirac cone on the surface. *Nature Physics*, 5:438–442, May 2009.

[30] J. Bardeen, L. N. Cooper, and J. R. Schrieffer. Theory of superconductivity. *Phys. Rev.*, 108:1175–1204, Dec 1957.

[31] J. Bardeen, L. N. Cooper, and J. R. Schrieffer. Microscopic theory of superconductivity. *Phys. Rev.*, 106:162–164, Apr 1957.

[32] Ettore Majorana. *Il Nuovo Cimento*, 14(4):171–184, 1937.

[33] A Yu Kitaev. Unpaired majorana fermions in quantum wires. *Physics-Uspekhi*, 44(10S):131, 2001.

[34] Y. S. Kim, M. Brahlek, N. Bansal, E. Edrey, G. A. Kapilevich, K. Iida, M. Tanimura, Y. Horibe, S.-W. Cheong, and S. Oh. Thickness-dependent bulk properties and weak

antilocalization effect in topological insulator bi_2se_3. *Phys. Rev. B*, 84:073109, Aug 2011.

[35] G. Zhang, H. Qin, J. Teng, J. Guo, Q. Guo, X. Dai, Z. Fang, and K. Wu. Quintuple-layer epitaxy of thin films of topological insulator bi2se3. *Applied Physics Letters*, 95(5), 2009.

[36] Y. Takagaki, U. Jahn, M. Ramsteiner, and K.-J. Friedland. Substitution of bismuth in hot wall epitaxy of bi 2 se 3 on transition metals. *Semiconductor Science and Technology*, 26(8):085031, 2011.

[37] D. Kong, J. J. Cha, K. Lai, H. Peng, J. G. Analytis, S. Meister, Y. Chen, H.-J. Zhang, I. R. Fisher, Z.-X. Shen, and Y. Cui. Rapid surface oxidation as a source of surface degradation factor for bi2se3. *ACS Nano*, 5(6):4698–4703, 2011.

[38] J. Zhang, Z. Peng, A. Soni, Y. Zhao, Y. Xiong, B. Peng, J. Wang, M. S. Dresselhaus, and Q. Xiong. Raman spectroscopy of few-quintuple layer topological insulator bi2se3 nanoplatelets. *Nano Letters*, 11(6):2407–2414, 2011.

[39] X. Qiu, C. Burda, R. Fu, L. Pu, H. Chen, and J. Zhu. Heterostructured bi2se3 nanowires with periodic phase boundaries. *Journal of the American Chemical Society*, 126(50):16276–16277, 2004.

[40] J. G. Checkelsky, Y. S. Hor, R. J. Cava, and N. P. Ong. Bulk band gap and surface

state conduction observed in voltage-tuned crystals of the topological insulator $\mathrm{bi_2se_3}$. *Phys. Rev. Lett.*, 106:196801, May 2011.

[41] S. S. Hong, W. Kundhikanjana, J. J. Cha, K. Lai, D. Kong, S. Meister, M. A. Kelly, Z.-X. Shen, and Y. Cui. Ultrathin topological insulator bi2se3 nanoribbons exfoliated by atomic force microscopy. *Nano Letters*, 10(8):3118–3122, 2010.

[42] D. Kong, J. C. Randel, H. Peng, J. J. Cha, S. Meister, K. Lai, Y. Chen, Z.-X. Shen, H. C. Manoharan, and Y. Cui. Topological insulator nanowires and nanoribbons. *Nano Letters*, 10(1):329–333, 2010.

[43] D. Kong, W. Dang, J. J. Cha, H. Li, S. Meister, H. Peng, Z. Liu, and Y. Cui. Few-layer nanoplates of bi2se3 and bi2te3 with highly tunable chemical potential. *Nano Letters*, 10(6):2245–2250, 2010.

[44] L. D. Alegria, M. D. Schroer, A. Chatterjee, G. R. Poirier, M. Pretko, S. K. Patel, and J. R. Petta. Structural and electrical characterization of bi2se3 nanostructures grown by metalorganic chemical vapor deposition. *Nano Letters*, 12(9):4711–4714, 2012.

[45] J. T. Mlack, A. Rahman, G. L. Johns, K. J. T. Livi, and N. Markovi. Substrate-independent catalyst-free synthesis of high-purity bi2se3 nanostructures. *Applied Physics Letters*, 102(19):–, 2013.

[46] H. Lind, S. Lidin, and U. Häussermann. Structure and bonding properties of

$(Bi_2Se_3)_m(Bi_2)_n$ stacks by first-principles density functional theory. *Phys. Rev. B*, 72:184101, Nov 2005.

[47] Dow s1800 positive photoresist. *Retrieved from http://micromaterialstech.com/products/ig-line-photoresists/dow-shipley-s1800-photoresist/*, page Dow Electronic Materials, May 2015.

[48] N Craig and T Lester. Hitchhikers guide to the dilution refrigerator. *Marcus Lab*, (2), 2004.

[49] H. Steinberg, J.-B. Laloë, V. Fatemi, J. S. Moodera, and P. Jarillo-Herrero. Electrically tunable surface-to-bulk coherent coupling in topological insulator thin films. *Phys. Rev. B*, 84:233101, Dec 2011.

[50] H. Steinberg, D. R. Gardner, Y. S. Lee, and P. Jarillo-Herrero. Surface state transport and ambipolar electric field effect in bi2se3 nanodevices. *Nano Letters*, 10(12):5032–5036, 2010.

[51] S. Cho, N. P. Butch, J. Paglione, and M. S. Fuhrer. Insulating behavior in ultrathin bismuth selenide field effect transistors. *Nano Letters*, 11(5):1925–1927, 2011.

[52] S. S. Hong, J. J. Cha, D. Kong, and Y. Cui. Ultra-low carrier concentration and surface-dominant transport in antimony-doped bi2se3 topological insulator nanoribbons. *Nature Communications*, 3, Mar 2012.

[53] X. He, T. Guan, X. Wang, B. Feng, P. Cheng, L. Chen, Y. Li, and K. Wu. Highly

tunable electron transport in epitaxial topological insulator (bi1-xsbx)2te3 thin films. *Applied Physics Letters*, 101(12), 2012.

[54] J. Chen, H. J. Qin, F. Yang, J. Liu, T. Guan, F. M. Qu, G. H. Zhang, J. R. Shi, X. C. Xie, C. L. Yang, K. H. Wu, Y. Q. Li, and L. Lu. Gate-voltage control of chemical potential and weak antilocalization in $\mathrm{bi_2se_3}$. *Phys. Rev. Lett.*, 105:176602, Oct 2010.

[55] Namrata Bansal, Yong Seung Kim, Matthew Brahlek, Eliav Edrey, and Seongshik Oh. Thickness-independent transport channels in topological insulator $\mathrm{bi_2se_3}$ thin films. *Phys. Rev. Lett.*, 109:116804, Sep 2012.

[56] H. Peng, W. Dang, J. Cao, Y. Chen, D. Wu, W. Zheng, H. Li, Z.-X. Shen, and Z. Liu. Topological insulator nanostructures for near-infrared transparent flexible electrodes. *Nature Chemistry*, 4:281–286, Jan 2012.

[57] G. Koren, T. Kirzhner, E. Lahoud, K. B. Chashka, and A. Kanigel. Proximity-induced superconductivity in topological $\mathrm{bi_2te_2se}$ and $\mathrm{bi_2se_3}$ films: Robust zero-energy bound state possibly due to majorana fermions. *Phys. Rev. B*, 84:224521, Dec 2011.

[58] G Koren, T Kirzhner, Y Kalcheim, and O Millo. Signature of proximity-induced p x + ip y triplet pairing in the doped topological insulator bi 2 se 3 by the s-wave superconductor nbn. *Europhysics Letters*, 103(6):67010, 2013.

[59] M. Veldhorst, M. Snelder, M. Hoek, C. G. Molenaar, D. P. Leusink, A. A. Golubov, H. Hilgenkamp, and A. Brinkman. Magnetotransport and induced superconductiv-

ity in bi based three-dimensional topological insulators. *physica status solidi (RRL) Rapid Research Letters*, 7(1-2):26–38, 2013.

[60] G. Koren and T. Kirzhner. Zero-energy bound states in tunneling conductance spectra at the interface of an s-wave superconductor and a topological insulator in nbn/bi_2se_3/au thin-film junctions. *Phys. Rev. B*, 86:144508, Oct 2012.

[61] J. R. Williams, A. J. Bestwick, P. Gallagher, Seung Sae Hong, Y. Cui, Andrew S. Bleich, J. G. Analytis, I. R. Fisher, and D. Goldhaber-Gordon. Unconventional josephson effect in hybrid superconductor-topological insulator devices. *Phys. Rev. Lett.*, 109:056803, Jul 2012.

[62] M. Veldhorst, C. G. Molenaar, X. L. Wang, H. Hilgenkamp, and A. Brinkman. Experimental realization of superconducting quantum interference devices with topological insulator junctions. *Applied Physics Letters*, 100(7):–, 2012.

[63] Y. S. Hor, A. J. Williams, J. G. Checkelsky, P. Roushan, J. Seo, Q. Xu, H. W. Zandbergen, A. Yazdani, N. P. Ong, and R. J. Cava. Superconductivity in $\mathrm{cu}_x\mathrm{bi}_2\mathrm{se}_3$ and its implications for pairing in the undoped topological insulator. *Phys. Rev. Lett.*, 104:057001, Feb 2010.

[64] Y.S. Hor, J.G. Checkelsky, D. Qu, N.P. Ong, and R.J. Cava. Superconductivity and non-metallicity induced by doping the topological insulators bi2se3 and bi2te3. *Journal of Physics and Chemistry of Solids*, 72(5):572 – 576, 2011.

[65] Takeshi Sakamoto, Makoto Wakeshima, Yukio Hinatsu, and Kazuyuki Matsuhira. Transport properties in normal-metal $bi_2pd_3s_2$ and superconducting $bi_2pd_3se_2$. *Phys. Rev. B*, 78:024509, Jul 2008.

[66] Toshiro Takabatake, Masayasu Ishikawa, and Alain Junod. Superconducting properties of the pd-se system. *Journal of the Physical Society of Japan*, 57(8):2763–2767, 1988.

[67] K. Chen, W Dai, C.D. Zhuang, Q. Li, S. Carabello, J. G. Lambert, J. T. Mlack, R. C. Ramos, and X. X. Xi. Momentum-dependent multiple gaps in magnesium diboride probed by electron tunnelling specstrocopy. *Nature Communications*, 3, Jan 2012.

Vita

Jerome Thomas Mlack was born February 20th, 1987 in Ashtabula, Ohio. He attended Edgewood Senior High School and graduated in 2005. After graduating high school he moved to Philadelphia, Pennsylvania and attend Drexel University. At Drexel University he had Co-op internships with the Army Research Laboratory in Adelphi, Maryland, the Penn State Navigation research and Development Center in Warminster, Pennsylvania, and the Magnetism and Spin Electronics Group at Trinity College in Dublin, Ireland. In 2010 he graduate from Drexel with a B.S. in Physics with a minor in Mathematics. Jerome next moved to Baltimore and began his graduate degree in condensed matter physics at Johns Hopkins University. After his third year at Johns Hopkins he spent a year visiting and researching at the Center for Quantum Devices in Copenhagen, Denmark. After his return he received his Ph.D. in June of 2015.